ISBN 978-82-471-1944-0 (printed ver.)
ISBN 978-82-471-1945-7 (electronic ver.)
ISSN 1503-8181

Zhengjie Zhu
Doctoral Thesis

Doctoral theses at NTNU, 2009:264

Zhengjie Zhu

The Least-Squares Spectral Element Method Solution of the Gas-Liquid Multi-fluid Model Coupled with the Population Balance Equation

NTNU
Norwegian University of
Science and Technology

Doctoral theses at NTNU, 2009:264
NTNU

NTNU
Norwegian University of
Science and Technology
Thesis for the degree of
philosophiae doctor
Faculty of Natural Sciences and Technology
Department of Chemical Engineering

NTNU
Norwegian University of
Science and Technology

Zhengjie Zhu

The Least-Squares Spectral Element Method Solution of the Gas-Liquid Multi-fluid Model Coupled with the Population Balance Equation

Thesis for the degree of philosophiae doctor

Trondheim, November 2009

Norwegian University of
Science and Technology
Faculty of Natural Sciences and Technology
Department of Chemical Engineering

NTNU
Norwegian University of
Science and Technology

NTNU
Norwegian University of Science and Technology

Thesis for the degree of philosophiae doctor

Faculty of Natural Sciences and Technology
Department of Chemical Engineering

ISBN 978-82-471-1944-0 (printed ver.)
ISBN 978-82-471-1945-7 (electronic ver.)
ISSN 1503-8181

Doctoral Theses at NTNU, 2009:264

Printed by Tapir Uttrykk

ISBN 978-82-471-1944-0 (printed version)

ISBN 978-82-471-1945-7 (electronic version)

ISSN 1503-8181

Thesis at NTNU:2009:264

Printed in Norway by NTNU-trykk, Trondheim

Abstract

This thesis work concentrates on the modelling of dispersed bubbly flow encountered widely in the chemical, oil & gas and nuclear industries. The computational fluid dynamics (CFD) that provides detailed information of gas-liquid flow has many advantages over the traditional modelling, which results in an enormously increased use of the CFD in the last decades.

It has been found out that in order to describe the complex inhomogeneous behavior of the gas-liquid flow caused by the size differences of bubbles, the necessary set of model equations to be solved must consist of the multi-fluid model for the flow, and a population balance equation (PBE) describing the bubble size distributions.

Such a complex model leads to a very expensive computational load and thus requires an advanced, accurate and efficient method to enable an appropriate numerical solution. The least-squares spectral element method (LSSEM) which possesses many extraordinary numerical properties may be a very attractive method to deal with such a model.

When solving the multi-fluid model the LSSEM has the potential of being much more accurate than the finite volume method (FVM) due to its higher order approximation. The pressure-velocity iterative algorithms like the semi-implicit pressure linked equation (SIMPLE) and the interphase slip algorithm (IPSA), are not required by the LSSEM. Furthermore, the properties of this method excludes the necessity of upwinded discretization of the convective terms.

Being a PBE solver, the Gauss-Legendre-Lobatto (GLL) quadrature points used in the LSSEM ensures a more efficient discretization of the internal coordinate than the method of classes (CM). Unlike the Method Of Moments (MOM), the LSSEM provides a direct estimation of the number density function. The moments of any order can be retrieved by post-calculation, and the number of desired moments does not affect the number of transport equations to be solved. The least-squares formulation leads to a better conditioned system than the Quadrature Method Of Moments (QMOM), and it does not pose any stability problem.

A new iterative algorithm is presented when using the LSSEM to couple the multi-fluid model and the PBE. It is based on the overall residue minimization so that the flow and the PBE are solved within same framework. The LSSEM also fully exploits the idea of single or multi-velocity group previously proposed in the homogeneous/inhomogeneous MUltiple-SIze-Group (MUSIG) models. The h/p-refinement divides the internal coordinate with high flexibility regarding to the size and velocity segregations.

For many commonly used breakup kernels in physical problems, the conservation of volume/mass is not always fulfilled, once they are employed in the CFD models. This unphysical feature is highly undesirable. In this work, the author propose a least-squares spectral element method which allows for incorporating the disperse phase mass-conservation (in the form of a continuity equation for the disperse phase) by means of the Lagrange

multipliers method. The PBE is solved under this additional constraint by finding the saddle point of the coupled system. The results obtained by the constrained LSM show that the mass is conserved everywhere in the domain with high accuracy. The constrained LSM has significantly improved the performance of the nonconservative breakup kernels.

A generic LSSEM toolbox lssem-suite has been designed and developed by the author. The lssem-suite toolbox is very flexible so that users can easily define the problem operator and other informations needed.

The first bubble column model consisting of both flow equations and the PBE has been successfully solved by the LSSEM with the use of the lssem-suite. Interphase forces and breakage/coalescence kernels have been taken from the literature. The algorithm, coupling scheme as well as implementation are illustrated in the thesis. The resulting solution has been validated against experimental data obtained for two-phase flow in a bubble column. The predicted bubble size distribution and other flow quantities are in good agreement with the experimental data.

Acknowledgements

This Ph.D thesis represents my devoted research work in the field of numerical modelling of multiphase flow. It contributes as part of the graduation requirement at the Department of Chemical Engineering at the Norwegian University of Science and Technology (NTNU).

This Ph.D work has given me a lot, but most of all it has given me the possibility to meet marvellous people. I would like to express my sincere gratitude to my supervisors Prof. Hugo A. Jakobsen and Associate Prof. Carlos A. Dorao for their patience, motivation, enthusiasm, and immense knowledge. They provided me with many helpful suggestions, important advice and constant encouragement during the course of this work. I am also grateful to Prof. Heinz A. Preizig, Associate Prof. Tore Haug-Warberg and Prof. Sigurd Skogestad for their trust and help in so many occasions.

The nicest achievement of my Ph.D work is never having had a problem with colleages. I wish to thank Olaf Trygve Berglihn and Dr. Bjørn Tore Løvfall for making me enjoy the Linux world. My thanks will go also to Dr. Dirk Lucas of Forschungszentrum, Germany for his valuable research co-operation and experimental data. Furthermore I have to thank Luciano Patruno, Andreas Linhart and Dr. Stathis Skouras, for sharing office with me. To all my colleagues, a sincere embrace and the conviction that the Department of Chemical Engineering will continue to grow to achieve more and more.

I am gratefully appreciated the financial supports of my Ph.D fellowship from the Gas Technology Center at NTNU and SINTEF, and the Research Council of Norway through a strategic University Program (CARPET).

Friends at university, SEFAS research institute, KFK football team, NTNUI swimming group and many others who I met, I want to thank all of you, who have shown me affection since my first day in Trondheim.

My special appreciation goes to my family, especially my parents - Xuebao Zhu and Xiaoling Huang, who taught me to value honesty, courage, and humility above all other virtues, and always supported me and encouraged me to concentrate on my study.

With affection,

Zhengjie Zhu

September 2009, Trondheim

Contents

List of Figures

Chapter 1

Introduction

1.1 Background

1.1.1 The bubble column reactors

Bubble columns are widely used for carrying out gas-liquid and gas-liquid-solid reactions in a variety of industrial applications in chemical, metallurgical, pharmaceutical and biochemical processes [17]. The primary advantages of bubble columns are simple con-

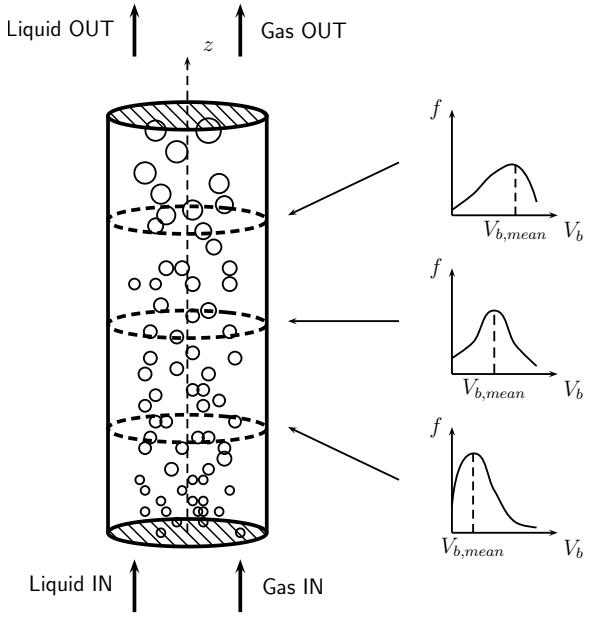

Figure 1.1: A bubble column: Bubbles flow upwards with different bubble size distribution at different axial positions. Mean bubble volumes are indicated by dashed lines.

struction due to no moving parts, high gas-liquid interfacial area, good mass/heat transfer

rates between the gas and liquid phases, and large liquid hold-up which is favorable for slow liquid phase reactions [83].

In bubble columns, four types of flow patterns have been observed, viz., homogeneous (bubbly), heterogeneous (churn-turbulent), slug, and annular flow. In these different flow regimes, the interaction of the dispersed gas phase with the continuous liquid phase varies considerably. Figure 1.2 shows the various flow regimes in bubble columns. The bubbly and churn-turbulent flow regimes are most frequently encountered. Depending upon the operating conditions, these two regimes can be separated by a transition regime.

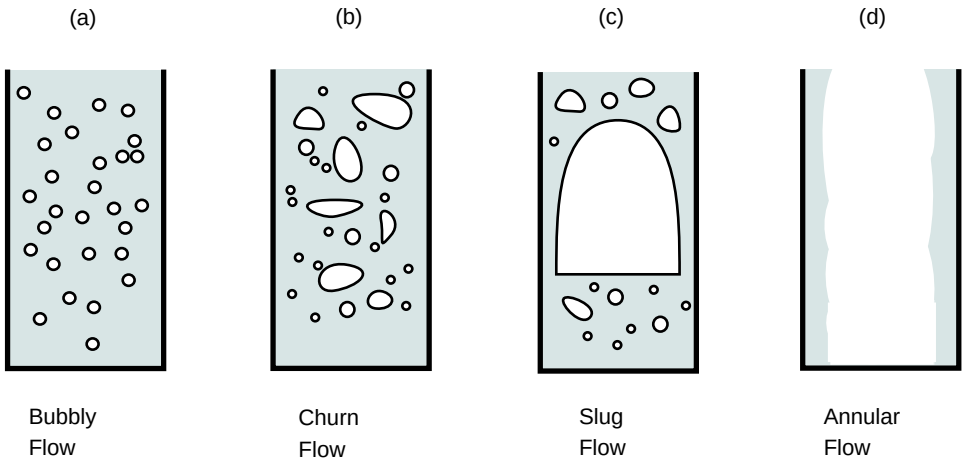

Figure 1.2: The flow regimes in bubble columns.

The homogeneous flow regime generally occurs at low to moderate superficial gas velocities. It is characterized by uniformly sized small bubbles traveling vertically with minor transverse and axial oscillations. There is practically no coalescence and break-up, hence there is a narrow bubble size distribution. The gas holdup distribution is radially uniform; therefore bulk liquid circulation is insignificant. The size of the bubbles depends mainly on the nature of the gas distributor and the physical properties of the liquid.

Heterogeneous flow occurs at high gas superficial velocities. Due to intense coalescence and break-up, small as well large bubbles appear in this regime, leading to wide bubble size distribution. The large bubbles churn through the liquid, and thus, it is called as churn-turbulent flow. The non-uniform gas holdup distribution across the radial direction causes bulk liquid circulation in this flow regime.

As one can see, homogeneous and heterogeneous flow regimes have entirely different hydrodynamic characteristics. Such different hydrodynamic characteristics result in different mixing as well as heat and mass transfer rates in these flow regimes. Therefore, the demarcation of flow regimes becomes an important task in the design and scale up of such reactors and has led to considerable research efforts which have resulted into various experimental methods and empirical, semi-empirical, and mechanistic models to identify flow regime transition.

Various methods have been implemented for the simulation of bubble columns. Flows encountered in bubble columns are inherently unsteady [85] and display a wide range of time and length scales and as a direct consequence thereof we adopt a multi-scale modeling approach consisting of served levels (see Figure 1.3) each developed to study the phenomena at a certain length and time scale.

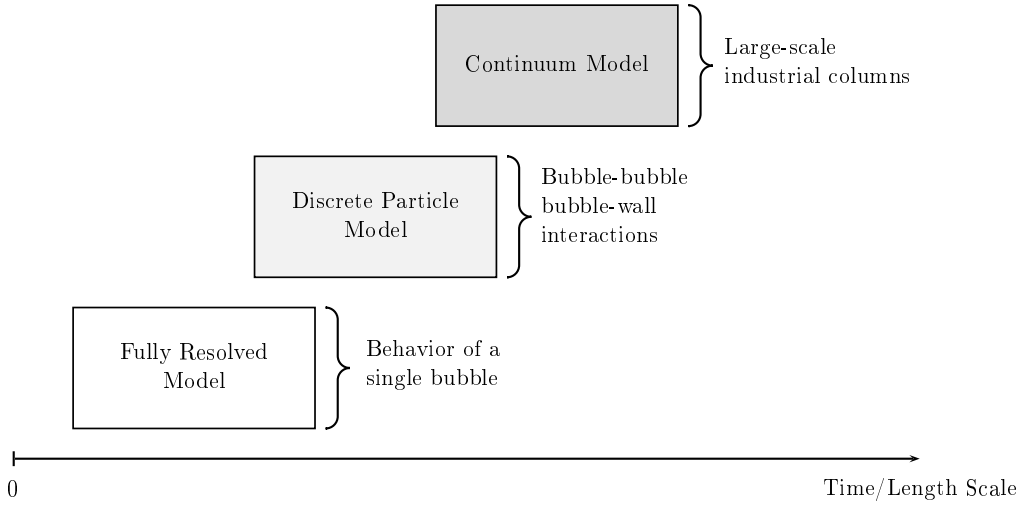

Figure 1.3: Multi-scale approach for modeling of dispersed gas-liquid two-phase flow. For each level of modeling the typical application is indicated.

At the lowest level (i.e. the smallest time and length scale) the front tracking (FT) method developed by Tryggvason and co-workers [90] can be used to study the behavior of a single bubble or a few (interacting) bubbles. The calculation generate insight in the behavior of a single bubble and provide closures for the bubble-liquid interaction. Due to the extensive computational requirements, FT can only be used for relatively small systems involving only a relatively small number of bubbles.

For systems, at larger time and length scales we use the Eulerian-Lagrangian (EL) or discrete bubble approach [9, 18, 19], which is particularly suited to study the effect of bubble-bubble and/or bubble-wall encounters. The Eulerian-Lagrangian formulation treats the liquid phase as continuum while tracks the motion of dispersed phase particles. Due to the large computational cost, the Eulerian-Lagrangian formulation is limited by the number of bubbles and size of the reactors [85]. Contrary to the FT approach, the flow field at the scale of an individual bubble is not resolved, closure laws for bubble-liquid interaction (drag, lift and added mass forces) have to be provided.

At the largest time and length scales the Eulerian-Eulerian (EE) or the continuum approach [26, 45, 72, 85] is used, which is particularly suited to model bubbly flows in industrial scale bubble columns. The Eulerian-Eulerian model describes the motion of the two-phase mixture in a macroscopic sense. It is also called the multi-fluid model. The multi-fluid model consists of a set of averaged transport equations for each phase. The gas holdup and interfacial transfer terms make these two phases coupled. In the Eulerian-

Eulerian approach, the computational cost is tractable and does not increase with the number of the bubbles. Similar to the EL approach closures for bubble-liquid and bubble-bubble interactions have to be provided.

1.1.2 The population balance model

In bubble columns, bubbles can break and coalescence due to bubble-bubble and bubble-fluid interactions. In particular, if breakage and coalescence events may produce very different bubble size distributions in the columns.

Additionally, bubbles can adopt different shapes such as spherical, distorted, cap or slug bubbles [14]. These differences in the bubble size and shape cause substantial differences in the disperse phase transport phenomena due to the differences in the drag force and interaction mechanisms. For example the vertical velocity of an air bubble rising in water is a function of bubble size (see Figure 1.4).

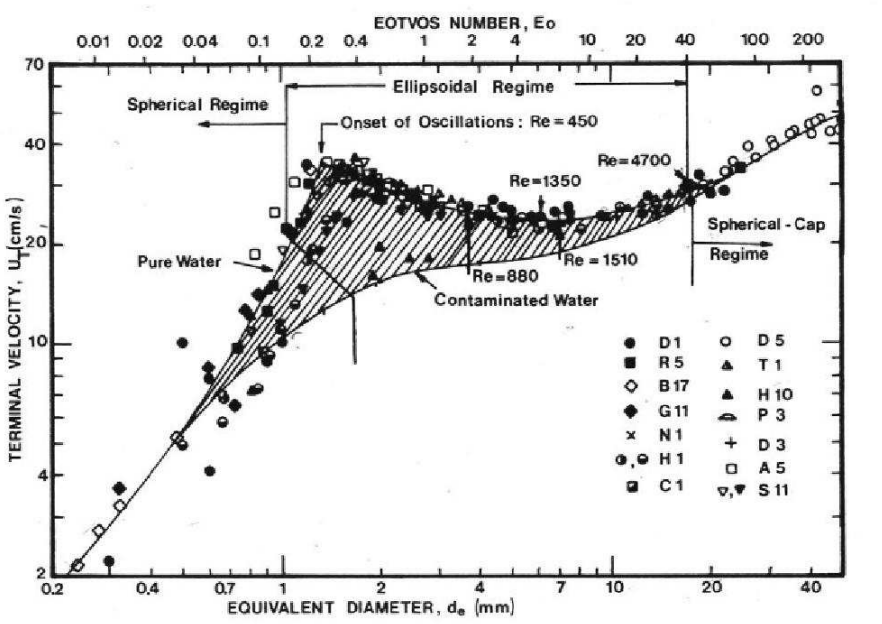

Figure 1.4: Terminal rise velocity of air bubbles in water as a function of bubble size and degree of contamination [14].

The flow field in bubble columns (Figure 1.5) shows that the lateral migration of bubbles driven by the lift force affects the larger bubbles moving towards the center of the column while smaller bubbles moving close to the column wall. The direction of the net bubble migration is determined by the different sizes and shapes of the bubbles and has a significant impact on the fluid dynamics.

Thus a balance equation is required to describe the changes in the particle population,

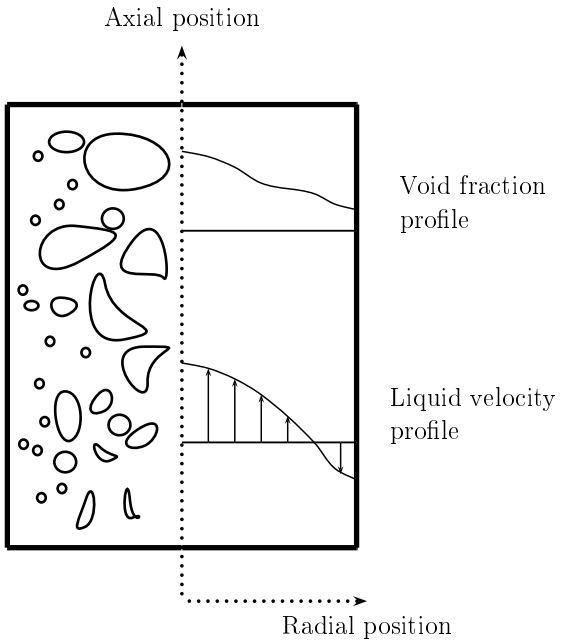

Figure 1.5: Flow field in the bubble column.

in addition to momentum, mass, and energy balances. This balance equation is generally referred to as the population balance equation (PBE) [79]. The PBE is a statistical Boltzmann-type equation. To make use of this modeling concept, a number density function is introduced to account for the particle population. With the aid of particle properties (e.g., particle size, porosity, composition, etc.), different particles in the population can be distinguished and their behavior can be described. Reliable closures are required for the unknown terms in the PBE. For a PBE describing breakage and coalescence of bubbles, the closures include the breakage kernel, daughter particle size distribution function and coalescence kernel, which are based on either empirical, or semi-empirical correlations.

It is noted that the population balance equation, as a stand alone model, has been successfully applied for different engineering problems [15, 38, 40, 78, 80]. For gas-liquid systems Reyes Jr. [81] and Lafi & Reyes [56] presented a detailed derivation of the mass, momentum and energy conservation equations for polydispersed system following an approach analogous to the Boltzmann's transport equation.

Kocamustafaogullari & Ishii [49] derived an interfacial area transport equation (IATE) which is a weighted integral over the bubble size of the particle transport equation. In this manner, an expression for the evolution of the average interfacial area concentration is obtained. Significant efforts were made by Millies et al. [57], Wu et al. [96], Morel et al. [71] and Hibiki & Ishii [36] to model bubble interactions and improve the IATE. The following approaches have extended the one-group IATE to two-group (Hibiki & Ishii [35], Ishii et al. [42], Kim et al. [48] and Sun et al.[87]) or even N-group (Carrica et al. [11]) by considering the size- and shape categories of bubbles. The multigroup model provides a more detailed description of the dispersed phase. In particular, due to the fact

that a velocity is computed for each group segregation by size can be modeled. However, this model is computationally expensive.

Several numerical methods are proposed to solve the PBE. The methods of classes (CM) [39, 53, 91] is based on discretization of the PBE into a finite number of size intervals. The quadrature method of moments (QMOM) [66, 67, 68] is an efficient alternative to the discrete population balance approach. In this approach, the population balance equation is transformed into a set of transport equations for moments of the distribution. The QMOM replaces the exact closure needed by the standard method of moments with an approximate closure. Marchisio et al.[65] have also proposed a variation of the QMOM, called the direct quadrature method of moments (DQMOM).

1.2 Modelling of the multi-fluid and the PBE

1.2.1 Numerical challenges

Inferred from the above discussions, a fixed bubble size model might not be suitable for predicting the correct fluid dynamics of a gas/liquid system. A model containing the bubble population balance must be used to handle breakage and coalescence phenomena in bubble columns. The final multi-fluid model complemented with a population balance model in which the hydrodynamics may be resolved with high resolution of the two phase flow in the external coordinates, while the PBE accounts for the bubble breakup and coalescence and predict the size distribution of the dispersed phase, is computational demanding. In particular, increasing the number of fields required for describing the gas velocity increases the computational cost considerably. The population balance equation is also computationally demanding since at least one extra dimension is introduced for characterizing the fluid particle. Besides, the internal coordinate of the population balance equation presents a global behavior, i.e. the changes in a point depend on the integral effects over the domain. Thus, for a three-dimensional physical domain such as a bubble column reactor, three dimensions are required in space, at least one internal dimension is required to represent the fluid particle and one dimension for the time. This gives a five-dimensional problem which has to be solved as efficiently as possible in order to enable the use of such a modeling approach for practical applications.

1.2.2 Current approaches

Several methods have been proposed for combining the PBE computations with commercial CFD codes. Lo [62] implemented the population balance equation in the commercial CFD code CFX via the multiple-size-group (MUSIG) model. A complete coupling is achieved by dividing the bubble size distribution into a finite number of discrete size classes. The basic assumption in this coupling is that bubbles of all sizes share a common

velocity field through coupling of the Sauter mean diameter to the drag term. Sanyal et al. [82] implemented both a CM and a method of moments (MOM) in the CFD code Fluent in conjunction with the Eulerian multiphase model. When adapting one of the above methods to solve the PBE together with a commercial CFD code, the particle size distribution is represented by an averaged particle size like the Sauter mean diameter for the fluid dynamics. One exception is the recently developed inhomogeneous MUSIG model [51, 52], which allows to consider size dependent momentum equations. According to the authors, 2-3 velocity groups should be sufficient. Bhole [3] also implemented size-specific bubble velocities by solving the momentum equations for each bubble classes in the CM. The drawbacks of these approaches are high cost of CPU time and additional equations for conservation of momentum have to be solved for each velocity group.

The QMOM [55] provides an attractive alternative solving the PBE associated with the multiphase flow model, especially when aggregation quantities, rather than an exact PSD, are desired. Its advantages are fewer variables (typically only six or eight moments) and a dynamic calculation of the size bins. The disadvantages are that the number of abscissas may not be adequate to describe the PSD and that solving the Product-Difference (PD) algorithm may be time consuming and the PD algorithm itself is ill-conditioned [23]. The applicability of QMOM is limited to no more than 12 moments[69], and the QMOM is also difficult to handle systems where there is a strong dependence of the dispersed-phase velocity on internal coordinates [65].

1.2.3 An advanced numerical method - the least-squares method

The least-squares method (LSM) is a member of the finite element method (FEM), and is formulated in a least-squares sense. If the high-order polynomials approximation instead of lower-order linear approximation is used, it called the least-squares spectral element method (LSSEM). The LSM is based on the minimization of a norm-equivalent functional. This method consists in finding the minimizer of the residual in a certain norm. Compared with other numerical methods, the LSM has the following advantages

- The LSM is highly *accurate*. It is a higher order spectral element method and therefore possesses all favorable properties of spectral element methods. The use of spectral methods leads to higher order convergence with h-refinement and even exponential convergence with p-enrichment if the underlying exact solution is sufficiently smooth. In general, for a given accuracy the high order spectral element method requires only a few collocation points whereas the low order finite volume method (FVM) requires a large number of grid cells.

- The weak formulation of the least-squares method is *universal* to all types of partial differential equations. Unlike other numerical methods which use central schemes to handle elliptic problems and upwinding schemes to handle hyperbolic equations, the least-squares method solves these both problems within one mathematical/computational framework.

- The least-squares formulation has a so-called *posterior* error indicator in form of the residue. This reliable indicator can be applied to check convergence or used for adaptive mesh refinement. No other numerical method can provide such information without additional calculation.
- In many practical problems we encounter the Poisson problem which both the potential and the gradient of the potential are of interest. The least-squares method is capable of converging optimally for these variables. This cannot be achieved with the Galerkin or finite difference/finite volume methods [46].
- In CFD, a common limitation with the FVM is the lack of possibilities to construct pressure correction and void schemes which enforce that all mass balances are fulfilled separately [43, 44]. The LSSEM may be restricted by similar limitations but does not require any pressure correction equation.
- When the LSM is applied to solve the PBE, it uses a much smaller number of discrete points than the CM. Since it solves the distribution function itself, it is not limited by the number of desired moments as in the QMOM. The discretized system is also much better conditioned.

The capacities of the LSM make this method particularly attractive to handle the multi-fluid model coupled with the PBE. Up till now, among the works on the LSM, the performance of the LSM to solve the hyperbolic equation [63], the Navier-Stokes equation and incompressible flow problems [46] have been investigated. Recently, Dorao and Jakobsen [21] discussed the applicability of the LSSEM to solve the PBE. Subsequent works [24, 25, 101] have been conducted to apply the LSM to solve the more complicated PBE with different terms.

Despite that efforts have been made to explore the capability and numerical properties of the LSM with the help of constructed analytical solution [24, 25, 31, 46, 63, 101], only a few contributions has been reported applying this method to real physical problems. In particular, the usage of the least-squares method in multiphase flow calculations combined with the PBE has not yet been investigated in spite of its proven capability. The complexity of this method is a main issue that hinders its broad applications. In addition, the LSM takes longer time to evaluate each iteration than the low-order methods. However, this drawback is made up by fewer discretization points and much higher accuracy, which might lead to less expensive overall computations eventually.

1.3 Objectives

The particular numerical issues mentioned in the previous section constitute a central motivation for this thesis work, that is, investigation of the applicability of using the least-squares method to solve the multi-fluid model coupled with the PBE. In particular, efficiency, accuracy and reliability are relevant aspects which are taken into consideration.

1.4 Scope of the work

1.4.1 Applying the LSM

In order to introduce the LSM to the field of multiphase flow modeling, a three-step approach is proposed.

1. First, the author will explore the capability of LSM to deal with multiphase flow problems. A LSM formulation for the solution of a one-dimensional, two-fluid model for the gas-liquid flow is developed. A least-squares operator which results in a stable numerical scheme is proposed.

2. Secondly, a LSM solver will be implemented aiming for the solution of the time-space-property PBE based on the previous work of Dorao et al. [25] and Zhu et al. [101]. The author also investigates an interesting alternative method - the least-squares direct minimization method (DM), which contributes to produce equally accurate results with a better conditioned formulation.

3. The last step consists in combining the work from the previous two steps. Rather than solving a stand-alone PBE or multifluid model, the formulation used consists of a two-fluid model that accounts for the characteristics of gas-liquid flow, and the population balance equation that predicts the bubble size distribution. The formulation of the least-squares operators for the two-fluid model and the PBE, as well as a new coupling algorithm are investigated.

1.4.2 Proposing a mass conservative formulation of the PBE

The author also addresses a fundamental problem in the modelling of multiphase flows (in particular two phase gas-liquid and liquid-liquid flows), namely the enforcement of mass-conservation when computing the evolution of disperse-phase properties within the PBE.

As a matter of fact, even the most advanced and in other respects physically-grounded models of shear-induced drop/bubble breakup (breakup kernels) do not ensure, once they are implemented in the PBE, that the volume fraction of the disperse phase will be preserved. The fact that the dispersed phase is not preserved during the breakage event results from the redistribution function which is not well behaved - the mass of the daughter particles is not equal to the mass of the parent particle (see Section 4.3.5). This unphysical feature is highly undesirable in applications where the composition of the system in terms of dispersed phase fraction is a key process variable. The author proposes to tackle this hitherto unsolved problem by introducing the constrained least-squares method and formulating a mass conservative PBE.

1.4.3 Developing a generic least-squares method solver - lssem-suite

In addition to the major contributions, a generic purpose least-squares spectral element method toolbox lssem-suite is designed and developed in this work. The intention is to separate complex codes of the numerical algorithm from that of physical equations, leading to less recoding effort and a better debugging efficiency. This toolbox allows the user to solve any partial differential equation (PDE) by just providing the problem operator, grid information and boundary conditions. Hence it is very suitable for solving large-scale physical problems, and is flexible for handling of multiple implementations involved in our step-wise research approach.

1.5 Papers

Paper I: Zhengjie Zhu, C.A.Dorao and H.A.Jakobsen. A least–squares method with direct minimization for the solution of the breakage-coalescence population balance equation. *Mathematics and Computers in Simulation, Volume 79, Issue 3, 1 December 2008, Pages 716-727*.

A least–squares method with a direct minimization algorithm is introduced to solve the nonlinear population balance equation that consists of both breakage and coalescence terms. The least–squares solver, the direct minimization solver together with a finite difference solver are implemented for comparisons. It is shown that the coalescence term introduces a strong non–linear behavior which can affect the robustness of the numerical solvers. In the comparison with the least–squares method, the direct minimization method is proved to be capable of producing equally accurate results, while its formulation is better conditioned. In the case of a nonlinear population balance equation system, the direct minimization method converges faster than the standard least–squares method.

Paper II: Zhengjie Zhu, C.A.Dorao and H.A.Jakobsen. Solution of bubble number density with breakage and coalescence in a bubble column by least-squares method. *Progress in Computational Fluid Dynamics (PCFD), Volume 9, Nos 6/7, Pages 436-446* .

A steady-state model has been built for an air-water bubble column. The bubble number density constitutive equation has been formulated through integrating the bubble transport equation. Proper kernels for the bubble breakage and coalescence rates have been taken from the literature. The momentum balance of the gas phase is included in the model which leads to a set of non-linear differential equations. The model has been successfully solved by using the least-squares method with high accuracy and fast convergence. The successive iteration has been applied to the linearized equation set. The model shows excellent agreements with experimental data.

Paper III: Zhengjie Zhu, C.A.Dorao and H.A.Jakobsen. On the fully coupled solution of a two-fluid model combined population balance equation using the least-squares spectral element method. *Industrial & Engineering Chemistry Research, Volume 48(17), July 2, 2009, Pages 7994-8006*.

In this work, a cross-sectional averaged two-fluid model combined with a population balance model is applied to simulate the flow field and the bubble size distributions in a two-phase bubble column. The Martinez-Bazan breakage kernel and a modified Prince and Blanch coalescence kernel have been chosen to describe bubble breakage and bubble coalescence, respectively.

In the present study, we discuss the use of a higher order spectral element method - the least-squares method, to compute the system of equations in a coupled manner. The least-squares method is highly accurate and has a number of advantages over the conventional numerical methods like the finite difference- and finite volume methods. In contrast to the finite volume method, when designing an overall solution algorithm this least squares method ensures that all the continuity equations are satisfied individually and it deals with both the convective and diffusive terms stably and accurately. The novel iterative algorithm solves the flow model and the population balance equation in a coupled manner.

The model has been validated against experimental data obtained for two-phase flow in a bubble column. The predicted bubble size distribution and other flow quantities are in good agreement with the experimental data.

Paper IV: Zhengjie Zhu, C.A.Dorao and H.A.Jakobsen. Mass conservative formulation of population balance equation using the least-squares spectral element method, Submitted to *Industrial & Engineering Chemistry Research* (Accepted).

In the standard least-squares formulation of the population balance equation significant loss of mass is observed for the dispersed phase. This mass loss is actually caused by the inexact conservation property reflected by many breakage kernels, hence incorrect physical interpretations of the model simulations may be drawn.

In this work a constrained least-squares spectral element method is developed enforcing mass conservation. This numerical property is accomplished by adding an extra restriction to the method in terms of the dispersed phase continuity equation through the Lagrange multipliers strategy. The discretized system resulting from applying the method to a two-phase population balance equation problem is symmetric and pseudopositive definite. Numerical experiments are carried out simulating the motion of a two-phase mixture passing through a 2D domain. The results obtained by the modified least-squares spectral element method show that the mass is conserved everywhere in the domain with high accuracy.

Paper V: Zhengjie Zhu, C.A.Dorao and H.A.Jakobsen. Modelling a bubble column with a bubble number density equation using the least-squares method. *6th International Conference on CFD in Oil and Gas, Metallurgical and Process Industries, SINTEF/NTNU, Trondheim, Norway, 10-12 June 2008* **(Selected as lead paper by reviewers)**.

A steady-state model has been built for an air-water bubble column. The bubble number density constitutive equation has been formulated through integrating the bubble transport equation. Proper kernels for bubble breakage and coalescence rate have been taken from the literature. The momentum balance of the gas phase is included in the model which leads to a set of non-linear differential equations. The model has been successfully solved by using the least-squares method with high accuracy and fast convergence. The successive iteration has been applied to the linearized equation set. The model shows excellent agreements with experimental data.

Paper VI: Zhengjie Zhu, L.E.Patruno, C.A.Dorao and H.A.Jakobsen. Simulation of the bubble coalescence in bubble column using the least-squares method. *11th International Conference on Multiphase Flow in Industrial Plant, Palermo, Italy, 7-10 September 2008 (MFIP'08)*.

The population balance equation (PBE) has been combined with a steady-state gas phase momentum equation to model the operation of an air-water bubble column. Instead of solving a bubble number density constitutive equation, a population balance equation with coalescence term has been solved. The system of equations has been linearized by successive iteration and solved by the least-squares method with high accuracy and fast convergence. The bubble size distribution along the column axis has been investigated and compared to the corresponding experimental data, showing good agreement.

1.6 Thesis Structure

The outline of this thesis is as following.

Chapter 2 introduces the basic idea and concepts of the least-squares spectral element method including the least-squares formulation, the spectral discretization and the assembly/scattering procedures in the spectral element approach. A constraint least-squares formulation is derived as a theoretical foundation of the formulation of the mass conservative PBE.

Chapter 3 illustrates the basis of the multiphase systems with particular emphasis on Eulerian-Eulerian models. Closure models and correlations on phase self-interaction, phase interactions and turbulence are presented as well. The computational techniques for solving the Eulerian-Eulerian multi-fluid model are discussed.

Chapter 4 presents the theory of the population balance equation, as well as mathematical interpretations and derivations of breakage and aggregation. Several numerical methods for solving the population balance equation are also included. In particular, a mass conservative PBE formulation based on the constraint LSM is proposed.

Chapter 5 is related to numerical strategies of solving the coupling between the multi-fluid models and the PBE. Among other methods, the LSSEM approach with its new iterative algorithm is explained in details.

Furthermore, conclusions and suggestions for future work are given in Chapter 6.

Chapter 2

The Least-Squares Method

The computational fluid dynamics (CFD) is a very valuable numerical simulation tool for investigation of complicated flow problems existing in various engineering fields. The most common numerical methods used in computational fluid dynamics (CFD) are: Finite Difference Methods (FDM), Finite Volume Methods (FVM) and Finite/Spectral Element Methods (FEM/SEM). The increased requirements of the CFDs on accuracy, error estimate, stability, geometry treatment, and so on, as well as increasing complexities of the problems constantly urge the development of new mathematical frameworks.

During the last decade, methods based on the least squares formulation ([6, 46]) emerged as an important alternative to the broad family of numerical methods. In particular, the least squares spectral element method (LSSEM) developed by [75, 76], which combine the least squares formulation as given by [6] and [46] with the spectral element approximation, is an attractive alternative for the solution of CFD problems. The LSSEM combines the generality of finite element methods, the accuracy of the spectral methods and the theoretical and computational advantages of the algorithmic design into a general mathematical framework.

In this chapter, a general presentation of the least squares formulation is provided followed by the spectral discretization. Practical issues related to the implementation of the least squares method are discussed, which serves as a theoretical foundation of the generic LSSEM toolbox - lssem-suite introduced in Appendix B.

2.1 The least-squares formulation

2.1.1 The general formulation

The least-squares method (LSM) is a well established numerical method for solving a wide range of mathematical problems (e.g. [6, 46, 75, 76]). The basic idea of the LSM is to minimize the integral of the square of the residual over the computational domain.

Consider the linear boundary-value problem:

$$\mathscr{L}\mathbf{f} = \mathbf{g}, \quad \text{in} \quad \Omega \in \mathbb{R}^{n_d} \tag{2.1}$$

$$\mathscr{B}\mathbf{f} = \mathbf{h}, \quad \text{on} \quad \Gamma \tag{2.2}$$

with $\mathscr{L}$ is a first-order partial differential operator:

$$\mathscr{L}\mathbf{f} = \sum_{i=1}^{n_d} \mathbf{L}_i \frac{\partial \mathbf{f}}{\partial x_i} + \mathbf{L}_0\mathbf{f} \tag{2.3}$$

in which $\Omega \in \mathbb{R}^{n_d}$ is a bounded domain with a piecewise smooth boundary Γ, n_d represents the number of space dimensions, $\mathbf{f}^{\mathrm{T}} = (f_1, f_2, \cdots, f_m)$ is a vector of m unknown functions of $\mathbf{x} = (x_1, \cdots, x_{n_d})$, $\mathbf{L}_i$ and $\mathbf{L}_0$ are $N_{eq} \times m$ matrices which continuously depend on $\mathbf{x}$, $\mathbf{g}$ is a given vector-valued function, $\mathscr{B}$ is a boundary algebraic operator, and $\mathbf{h}$ is a given vector-valued function on the boundary. Without loss of generality we assume that the vector $\mathbf{h}$ is null.

If the system is well-posed and the operator $\mathscr{L}$ is a continuous mapping from an underlying function space $\mathbf{X}(\Omega)$ onto the space $\mathbf{Y}(\Omega)$. The two norms $\| \bullet \|_{\mathbf{X}}$ and $\| \bullet \|_{\mathbf{Y}}$ are equivalent. Therefore,

$$C_1\|\mathbf{f}\|_{\mathbf{X}} \leq \|\mathscr{L}\mathbf{f}\|_{\mathbf{Y}} \leq C_2\|\mathbf{f}\|_{\mathbf{X}}, \quad \text{for } C_1, C_2 \geq 0 \tag{2.4}$$

holds. The first inequality states that the inverse of $\mathscr{L}$ is continuous and this inequality is called *coercivity*. The constant C_1 is called the *coercivity constant*. The second inequality states that the operator $\mathscr{L}$ is bounded and continuous in the function space $\mathbf{X}$. The constant C_2 is called the *continuity constant* [46].

The statement (2.4) implies that minimization of the error in the $\mathbf{X}$-norm is equivalent to minimization of the residual in the $\mathbf{Y}$-norm.

$$C_1\|\mathbf{f}^{ex} - \mathbf{f}\|_{\mathbf{X}} \leq \|\mathscr{L}(\mathbf{f}^{ex} - \mathbf{f})\|_{\mathbf{Y}} = \|\mathscr{L}\mathbf{f} - \mathbf{g}\|_{\mathbf{Y}} \leq C_2\|\mathbf{f}^{ex} - \mathbf{f}\|_{\mathbf{X}} \tag{2.5}$$

in which, $\mathbf{f}^{ex}$ is the exact solution, the quantity $\mathscr{L}\mathbf{f} - \mathbf{g} = \mathbf{R}$ is the residual of the equation. Eq.(2.5) ensures that when a sequence of residuals converges to zero in the $\mathbf{Y}$-norm, the sequence converges to the exact solution in the $\mathbf{X}$-norm. This connection between the residuals and the errors can be visualized in Figure 2.1.

The least-squares formulation is based on the minimization of a norm-equivalent functional. The norm-equivalent functional for Eq.(2.1) is given by

$$\mathscr{J}(\mathbf{f}) = \frac{1}{2}\|\mathscr{L}\mathbf{f} - \mathbf{g}\|^2_{\mathbf{Y}(\Omega)} \tag{2.6}$$

with the norm defined like

$$\| \bullet \|^2_{\mathbf{Y}(\Omega)} = < \bullet, \bullet >_{\mathbf{Y}(\Omega)} = \int_{\Omega} \bullet \bullet \, d\Omega \tag{2.7}$$

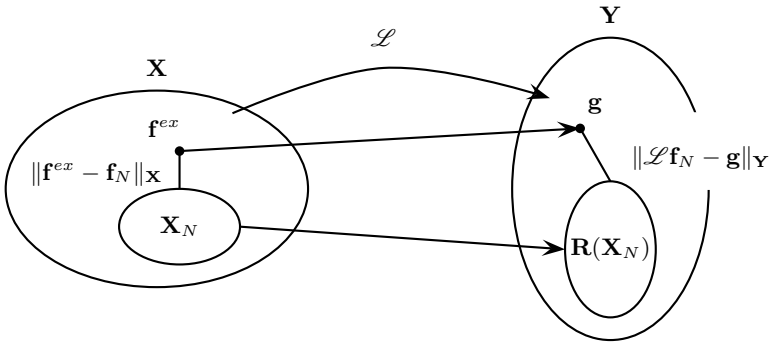

Figure 2.1: The norm-equivalence ensures that minimization of the error in the $\mathbf{X}$-norm is equivalent to the minimization of the residual in the $\mathbf{Y}$-norm.

The minimization statement is equivalent to: find $\mathbf{f} \in \mathbf{X}(\Omega)$ such that

$$\lim_{\epsilon \to 0} \frac{d\mathcal{J}\left(\mathbf{f} + \epsilon \mathbf{v}\right)}{d\epsilon} = 2 \int_{\Omega} (\mathscr{L}\mathbf{v})^{\mathrm{T}} (\mathscr{L}\mathbf{f} - \mathbf{g}) d\Omega = 0, \quad \forall \mathbf{v} \in \mathbf{X}(\Omega) \tag{2.8}$$

where $\mathbf{X}(\Omega)$ is the space of the admissible functions. $\mathbf{v}$ is an arbitrary trial function and ε is a small perturbation. Consequently, the necessary condition can be written as:

Find $\mathbf{f} \in \mathbf{X}(\Omega)$ such that

$$A(\mathbf{f}, \mathbf{v}) = F(\mathbf{v}) \quad \forall \mathbf{v} \in \mathbf{X}(\Omega) \tag{2.9}$$

with

$$A(\mathbf{f}, \mathbf{v}) = \langle \mathscr{L}\mathbf{f}, \mathscr{L}\mathbf{v} \rangle_{Y(\Omega)} \tag{2.10}$$

$$F(\mathbf{v}) = \langle \mathbf{g}, \mathscr{L}\mathbf{v} \rangle_{Y(\Omega)} \tag{2.11}$$

where $A : \mathbf{X} \times \mathbf{X} \to \mathbb{R}$ is a symmetric, continuous bilinear form, and $F : \mathbf{X} \to \mathbb{R}$ a continuous linear form.

2.1.2 The discretized form

If the inner products in (2.9) are discretized, we have the linear algebraic equations

$$\mathbf{A}\mathbf{U} = \mathbf{F} \tag{2.12}$$

where $\mathbf{U}$ is the global vector of unknown coefficients. The global matrix $\mathbf{A}$ is

$$\mathbf{A} = \int_{\Omega} \left(\mathscr{L}\Phi_0, \mathscr{L}\Phi_1, \ldots, \mathscr{L}\Phi_N\right)^{\mathrm{T}} \left(\mathscr{L}\Phi_0, \mathscr{L}\Phi_1, \ldots, \mathscr{L}\Phi_N\right) d\Omega \tag{2.13}$$

and the vector $\mathbf{F}$ is defined as:

$$\mathbf{F} = \int_{\Omega} \left(\mathscr{L}\Phi_0, \mathscr{L}\Phi_1, \ldots, \mathscr{L}\Phi_N\right)^{\mathrm{T}} d\Omega \tag{2.14}$$

in Eq. (2.13) and Eq. (2.14)

$$\mathscr{L}\Phi_j = \sum_{i=1}^{n_d} \frac{\partial \Phi_j}{\partial x_i}\mathbf{L}_i + \Phi_j \mathbf{L}_0 \tag{2.15}$$

in which $\Phi_j(\mathbf{x})$ is the basis function. The final system of equations is symmetric and positive definite, hence the solution can be obtained in an efficient way using standard matrix solvers.

2.2 Spectral discretization

In the LSM implemented in this work, the high-order spectral discretization based on the Lagrangian polynomials through the Gauss-Legendre-Lobatto points is used as orthogonal basis functions in order to approximate the problem operator in the partial differential equations [16, 75].

2.2.1 Nodal expansion

The discretization statement consists in searching the solution in a reduced subspace $X_N(\hat{\Omega})$, i.e.

$$f_N(\hat{x}) \in X_N(\hat{\Omega}) = \left[X \cap \mathbb{P}_N(\hat{\Omega})\right] \subset X(\hat{\Omega}) \tag{2.16}$$

in which $\hat{\Omega} \in [-1 \quad 1]$ is the one-dimensional local reference coordinate. $\mathbb{P}_N(\hat{\Omega})$ is the space of all functions which are polynomials of degree N or less over $\hat{\Omega}$, while X_N is a finite dimensional subspace of X of dimension N. The subspace $X_N(\hat{\Omega})$ is constructed as

$$X_N(\hat{\Omega}) = \text{span}\left\{\phi_1(\hat{x}), \phi_2(\hat{x}), \ldots, \phi_N(\hat{x})\right\} \tag{2.17}$$

Note that $\phi_j(\hat{x})$ are basis functions defined in local reference coordinate, $-1 \leq \hat{x} \leq 1$ with $\hat{x} = \mathcal{F}^{-1}(x)$ as the reference point mapped from function coordinate Ω (see Figure 2.2).

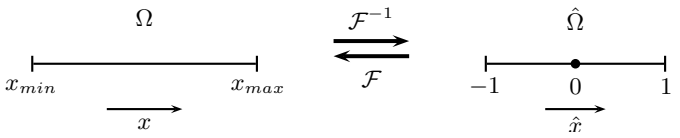

Figure 2.2: The affine mapping $\mathcal{F}$ is a one-to-one mapping between $\hat{\Omega}$ and Ω.

$\mathcal{F}$ is a affine mapping operator. We denote a point in the physical domain as x, while the corresponding point in the reference domain is denoted as $\hat{x}$. Hence,

$$x = \mathcal{F}(\hat{x}) \tag{2.18}$$

$$\hat{x} = \mathcal{F}^{-1}(x) \tag{2.19}$$

Given a set of $(N+1)$ nodal points, denoted by $\hat{x}_i (1 \leq i \leq N+1)$, the Lagrange polynomial $\phi_j(\hat{x}_i)$ is the unique polynomial of order N which has a unit value at $\hat{x}_i$ and is zero at $\hat{x}_j (i \neq j)$ (see Figure 2.3). This definition can be written as

$$\phi_j(\hat{x}_i) = \delta_{ij} \tag{2.20}$$

The $N+1$ basis functions consist of Lagrangian polynomials through the Gauss-Legendre-Lobatto (GLL) collocation points

$$\phi_j(\hat{x}) = \frac{(\hat{x}^2 - 1) dL_N(\hat{x})/d\hat{x}}{N(N+1)L_N(\hat{x})(\hat{x} - \hat{x}_j)} \tag{2.21}$$

The $N+1$ GLL-points, are the roots of the first derivative of the Legendre polynomial of degree N, extended with the boundary points.

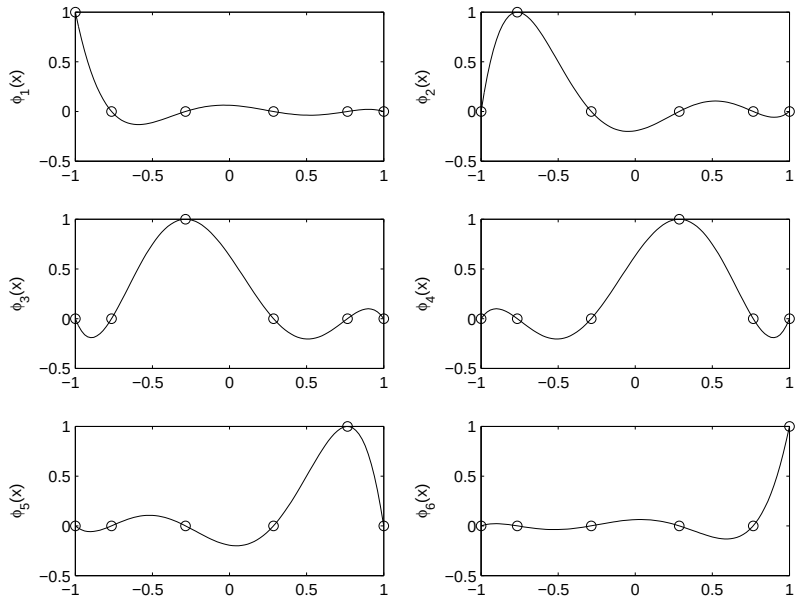

Figure 2.3: GLL-roots and nodal expansion modes for a polynomial order of $N = 5$.

Therefore, f_N can be expressed in terms of linear combinations of basis functions:

$$f_N(\hat{x}) = \sum_{j=1}^{N+1} f_j \phi_j(\hat{x}) \tag{2.22}$$

where f_j is the basis coefficient associated with the basis function $\phi_j(\hat{x})$ (Lagrangian polynomials), it follows that the basis coefficient f_j is equal to the value of the discrete solution $f_N(x)$ at the GLL points (or node) $\hat{x}_j$, i.e. $f_j = f_N(\hat{x}_j)$. Due to this property, we also say that we are using a *nodal* basis.

2.2.2 Numerical integration - Gaussian quadrature

It is possible to use the numerical integration to evaluate integrals of the form

$$\int_{-1}^{1} f(\hat{x})\, d\hat{x} \tag{2.23}$$

The fundamental concept is the approximation of the integral by the *Gaussian quadrature* based on the GLL roots

$$\int_{-1}^{1} f(\hat{x})\, d\hat{x} \approx \sum_{p=1}^{P+1} w_p f(\hat{x}_p) \tag{2.24}$$

where w_p are specified constants or weights and $\hat{x}_p$ represents $P+1$ distinct quadrature points in the interval $[-1 \quad 1]$.

In this technique the integrand $f(\hat{x})$ of Eq.(2.23) is approximated by a Lagrange polynomial of order N,

$$f(\hat{x}) \approx \sum_{j=1}^{N+1} f_j \phi(\hat{x}) \tag{2.25}$$

in which, $N = P$. If we substitute Eq.(2.25) into Eq.(2.24) we obtain a representation of the integral (2.23) as a finite summation:

$$\int_{-1}^{1} f(\hat{x})\, d\hat{x} \approx \sum_{p=1}^{P+1} w_p \sum_{j=1}^{N+1} f_j \underbrace{\phi_j(x_p)}_{\delta_{pj}} = \sum_{p=1}^{P+1} w_p f_p \tag{2.26}$$

with weighting factors w_p

$$w_p = \int_{-1}^{1} \phi_p(\hat{x})\, d\hat{x} \tag{2.27}$$

By substituting the Lagrange polynomial $\phi_p(\hat{x})$ of Eq.(2.27), which is the Lagrangian polynomial based on the GLL-roots, into the above expression for the weighting factors we obtain an expression for the $(P+1)$ Gauss-Legendre-Lobatto weights (GLL-weights) [46, 47]:

$$w_p = \frac{2}{P(P+1)[L_P(\hat{x}_p)]^2} \tag{2.28}$$

with $\hat{x}_p$ the p–th GLL–root, $1 \leq p \leq P+1$.

Notice that expression (2.26) is exact if the integrand $f(\hat{x})$ is a polynomial of degree $2P-3$ or less.

2.2.3 Numerical differentiation

If the number of the nodes is equal to the order of the basis functions, the derivative of the Lagrangian basis function Eq. (2.21) evaluated at the GLL-points are given by

$$\frac{d\phi_j}{d\hat{x}}\Big|_{\hat{x}_i} = \begin{cases} \frac{L_N(\hat{x}_i)}{L_N(\hat{x}_j)} \frac{1}{(\hat{x}_i - \hat{x}_j)} & \text{for } i \neq j, 1 \leq i,j \leq N+1, \\ 0 & \text{for } 1 < i = j < N+1, \\ -\frac{1}{4}N(N+1) & \text{for } i = j = 1, \\ \frac{1}{4}N(N+1) & \text{for } i = j = N+1. \end{cases} \tag{2.29}$$

2.2.4 Error estimation

The LSM is a h/p-version of the finite element method (h/p-FEM) which is a generalisation of the classical (h-version) FEM and the p-version FEM/spectral method in that convergence is achieved by simultaneously refining the mesh and increasing the approximation order.

Now, assume that the given function has a certain regularity. In particular, let

$$f \in H^{\sigma}(\Omega), \tag{2.30}$$

where H^{σ} represents a function space that consists of all functions that their σ-th derivatives are square integrable, i.e.

$$H^{\sigma}(\Omega) = \left\{ v \mid \int_{-1}^{1} \sum_{j=0}^{\sigma} \left(\frac{d^j v}{d\hat{x}^j} \right)^2 d\hat{x} < \infty \right\} \tag{2.31}$$

It can then be shown that [10]

$$\|f^{ex} - f^N\|_{L^2(\Omega)} \leq cN^{-\sigma} \|f^{ex}\|_{H^{\sigma}(\Omega)} \tag{2.32}$$

If $\sigma \to \infty$, f^N will converge towards f^{ex} faster than any algebraic power of $1/N$. In fact, it can be shown that the approximation error will go to zero exponentially fast as N increases. We can express this as

$$\|f^{ex} - f^N\|_{L^2(\Omega)} \sim e^{-\mu N} \tag{2.33}$$

for some $\mu \in \mathbb{R}^+$.

2.2.5 Spectral discretization in $\mathbb{R}^n$

We can define the two-dimensional high-order polynomial space $\mathbb{P}_N(\hat{\Omega})$ by using the one-dimensional nodal basis based on a tensor product Gauss-Legendre (Lobatto) grid, see Figure 2.4. Note that

$$\dim\left(\mathbb{P}_N(\hat{\Omega})\right) = (N_x+1)\times(N_y+1) \quad \text{in} \quad \mathbb{R}^2 \tag{2.34}$$

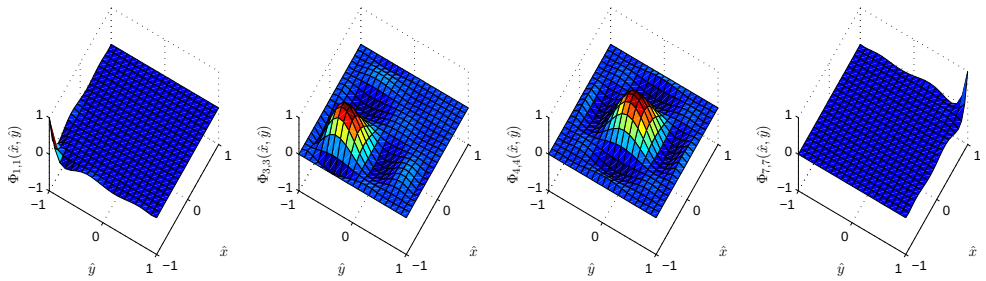

Figure 2.4: Four of the forty nine two-dimensional basis functions $\Phi_{r,s}(\hat{x},\hat{y})$ of order $N_x = N_y = 6$, (a) $\Phi_{1,1}(\hat{x},\hat{y})$, (b) $\Phi_{3,3}(\hat{x},\hat{y})$, (c) $\Phi_{5,5}(\hat{x},\hat{y})$, (d) $\Phi_{7,7}(\hat{x},\hat{y})$.

Therefore, $f_N(\hat{x},\hat{y})$ can be expressed in terms of linear combinations of the one-dimensional basis functions in each dimension:

$$f_N(\hat{x},\hat{y}) = \sum_{r=1}^{N_x+1}\sum_{s=1}^{N_y+1} f_{rs}\phi_r(\hat{x})\phi_s(\hat{y}) \tag{2.35}$$

where f_{rs} is the basis coefficient associated with the basis function $\phi_r(\hat{x})\phi_s(\hat{y})$, it follows that the basis coefficient f_{rs} is equal to the value of the discrete solution $f_N(\hat{x},\hat{y})$ at the GLL points $(\hat{x}_p,\hat{y}_q)$, i.e. $f(\hat{x}_p,\hat{y}_q) = f_N(\hat{x}_p,\hat{y}_q) = f_{pq}$.

The integration of the function is evaluated by the Gaussian quadrature rule:

$$\int_{-1}^{1}\int_{-1}^{1} f(\hat{x},\hat{y})d\hat{x}d\hat{y} \approx \sum_{k=1}^{K+1}\sum_{l=1}^{L+1} w_k w_l f_{kl} \tag{2.36}$$

where w_k, w_l and $\hat{x}_k$, $\hat{y}_l$ are the weights and points of quadrature.

The derivatives of the two-dimensional basis function with respect to each reference variables evaluated at the GLL-points are given by

$$\frac{\partial(\phi_r(\hat{x})\phi_s(\hat{y}))}{\partial\hat{x}}\Big|_{x_p,y_q} = \phi_r'(\hat{x}_p)\phi_s(\hat{y}_q) = [\mathbf{d}_{\hat{x}}]_{pr}[\mathbf{b}_{\hat{y}}]_{qs} \tag{2.37}$$

$$\frac{\partial(\phi_r(\hat{x})\phi_s(\hat{y}))}{\partial\hat{y}}\Big|_{x_p,y_q} = \phi_r(\hat{x}_p)\phi_s'(\hat{y}_q) = [\mathbf{b}_{\hat{x}}]_{pr}[\mathbf{d}_{\hat{y}}]_{qs} \tag{2.38}$$

in which $[\mathbf{b}_{\hat{x}}]$ and $[\mathbf{b}_{\hat{y}}]$ are the discrete one-dimensional zero-order operator in $\hat{x}$ and $\hat{y}$, respectively. The matrix $\mathbf{b}$ is also sometimes referred to as the *mass matrix* [16]. $[\mathbf{d}_{\hat{x}}]$ and $[\mathbf{d}_{\hat{y}}]$ are the one-dimensional derivatives matrices in $\hat{x}$ and $\hat{y}$.

The spectral discretization used in two-dimensional domain ($\mathbb{R}^2$) can be extended higher dimensional cases.

2.3 Spectral element approximation

The problem domain Ω can be divided into N_e subdomains $(\Omega_1, \Omega_2, \ldots, \Omega_{N_e})$ in order to achieve better numerical efficiency. Therefore, we have

$$\Omega = \bigcup_{e=1}^{N_e} \Omega_e. \tag{2.39}$$

It is possible to express the global modes $\phi_J(x)$ in terms of the local expansion modes $\phi_j^e(x)$. Therefore, we can express local expansion of unknowns f_N in terms of $\phi_j^e(x)$, that is,

$$f_N(x) = \sum_{J=1}^{N} f_J \phi_J(x) = \sum_{e=1}^{N_e} \sum_{j=1}^{N_m^e+1} f_j^e \phi_j(x), \tag{2.40}$$

This relation can also be visualized in Figure A.1.

In practical, a general procedure for global assembling is to construct a mapping array $\mathcal{GM}$ called the *local-global mapping* matrix. $\mathcal{GM}$ is a $N_e \times (N_x^e + 1)$ matrix where the e–th row contains in a fixed order the indices of the global expansion coefficients of the e–th subdomain. N_m^e is called the *elemental degree of freedom*.

The local-global mapping matrices $\mathcal{GM}$ can also be expressed by the sparse gathering matrix $\mathcal{G}_e$ which has nonzero entries. The global assembly of the N_e local systems can readily be obtained with:

$$\mathbf{A}\mathbf{f}_g = \mathbf{g} \Longleftrightarrow \left[\sum_{e=1}^{N_e} \mathcal{G}_e^{\mathrm{T}} \mathbf{A}_e \mathcal{G}_e\right] \mathbf{f}_g = \sum_{e=1}^{N_e} \mathcal{G}_e^{\mathrm{T}} \mathbf{g} \tag{2.41}$$

For detailed information on the assembling procedure please refer to Appendix. A.

2.4 The least-squares direct minimization formulation

Recently, an alternative formulation, which avoids variational analysis, has been implemented in the conventional LSM to minimize the residual directly [37]. The novel minimization function can be written as:

Find all $f_N \in X(\Omega)$ which minimize the function

$$\mathcal{J}(f_N) = \|\mathscr{L} f - g\|^2_{Y(\Omega)} \tag{2.42}$$

The solution space is restricted to a finite dimensional subspace $X_N(\Omega) \subset X(\Omega)$, so $f_N \subset X_N(\Omega)$. The integrals which constitute the L^2-norm can numerically be written as:

Find all $f_N \in X(\Omega)$ which minimize the function

$$\mathcal{J}(f_N) = \sum_{q=0}^{Q} \left(\mathscr{L} f - g\right)^2 \Big|_{x_q} w_q \tag{2.43}$$

In matrix notation, this can be written as:

Find all $f_N \in X(\Omega)$ which minimize the function:

$$\left(\mathbf{L}\boldsymbol{f} - \boldsymbol{g}\right)^T \mathbf{\Lambda} \left(\mathbf{L}\boldsymbol{f} - \boldsymbol{g}\right) = \|\sqrt{\mathbf{\Lambda}} \left(\mathbf{L}\boldsymbol{f} - \boldsymbol{g}\right)\|^2 \tag{2.44}$$

The solution which minimizes the residual norm of Eq.(2.44) is given by:

$$\sqrt{\mathbf{\Lambda}}\mathbf{L}\boldsymbol{f} = \sqrt{\mathbf{\Lambda}}\boldsymbol{g} \tag{2.45}$$

It can be proven that solving this equation is equivalent to solving Eq.(2.9)[54], but this system is much better conditioned and avoids matrix-matrix multiplication. However, the system matrix $\sqrt{\mathbf{\Lambda}}\mathbf{L}$ is not always symmetric, positive definite. The LSM still has the advantage of handling the first-order differential equation and an overdetermined algebraic system still has to be solved in the least-squares sense.

Using matrices $\mathcal{Q}$ and $\mathcal{R}$ from QR-decomposition of the matrix $\sqrt{\mathbf{\Lambda}}\mathbf{L}$, one can solve $\boldsymbol{f}$ by:

$$\boldsymbol{f} = \mathcal{R}^{-1}(\mathcal{Q}^T \sqrt{\mathbf{\Lambda}}\boldsymbol{g}) \tag{2.46}$$

In the paper entitled "A least-squares method with direct minimization for the solution of the breakage-coalescence population balance equation" (Appendix E.1), the authors presented the applicability of using the direct minimization to solve the PBE, and compared the method with the classic LSM.

2.5 The constrained least-squares formulation

The constrained least-squares solution [4, 5, 7, 12, 77] is based on the minimization of the least-squares functional (2.6) subjected to a linear constraint equation.

$$\mathscr{L}_c f = g_c \tag{2.47}$$

The constrained problem is essentially a minimization problem that can be expressed in the form:

$$\min_{\mathbf{f}\in\mathbf{Y}} \mathcal{J}(f) \quad \text{subject to} \quad (2.47). \tag{2.48}$$

where the constraint equation (2.47) holds in function space S.

This problem is solved using methods based on applying the Lagrange multiplier method. The constrained least-squares solution results from the equilibrium point of the following extended Lagrangian functional

$$\mathcal{I}(f,\lambda) = \mathcal{J}(f) + \mathscr{L}_c f \tag{2.49}$$

where $\mathcal{J}(f)$ represents the least-squares functional defined in Eq.(2.6).

A system of equations is obtained by substituting $f = f + \epsilon v$ and $\lambda = \lambda + \epsilon_c v_c$ and taking the partial derivatives of $\mathcal{I}$ with respect to ϵ and ϵ_c:

$$\lim_{\epsilon,\epsilon_c\to 0} \frac{\partial}{\partial\epsilon}\mathcal{I}(f+\epsilon v, \lambda+\epsilon_c v_c) = 0, \quad \forall v \in X(\Omega) \quad \forall v_c \in M(\Omega) \tag{2.50}$$

$$\lim_{\epsilon,\epsilon_c\to 0} \frac{\partial}{\partial\epsilon_c}\mathcal{I}(f+\epsilon v, \lambda+\epsilon_c v_c) = 0, \quad \forall v \in X(\Omega) \quad \forall v_c \in M(\Omega) \tag{2.51}$$

This result yields the following mixed formulations:

Find $(f,\lambda) \in X(\Omega) \times M(\Omega)$ such that:

$$\begin{cases} A(f,v) + B(v,\lambda) = F(v) & \forall v \in X(\Omega), \\ B(f,v_c) = 0 & \forall v_c \in M(\Omega) \end{cases} \tag{2.52}$$

where the space $X(\Omega)$ consists of the function f and the space $M(\Omega)$ consists of the function λ. Note that in general X and M can be different function spaces. The bilinear form A and its corresponding right-hand side linear form F have been defined in Eq.(2.10) and Eq.(2.11). The bilinear form $B(v,\lambda)$ is given by:

$$B(v,\lambda) = \langle \lambda, \mathscr{L}_c v - g_c \rangle \tag{2.53}$$

Let us assume that the system (2.49) has a unique solution $(f,\lambda) \in X \times M$. Moreover,

$$\|f\|_X + \|\lambda\|_M \leq C\left(\|f\|_Y + \|\lambda\|_S\right), \tag{2.54}$$

in which, C is a positive constant $f \in X$ is the unique solution of the constrained minimization problem (2.49).

Let us denote the total degree of freedom of f by N^t and total degree of freedom of λ by M^t. Using the spectral approximation introduced in Section 2.3, together with the

weak formulation (2.52), the following linear algebraic matrix system is obtained for the constrained least-squares formulation.

$$\begin{bmatrix} \mathbf{A} & \mathbf{B}^T \\ \mathbf{B} & \mathbf{0} \end{bmatrix} \begin{bmatrix} \mathbf{f} \\ \boldsymbol{\lambda} \end{bmatrix} = \begin{bmatrix} \mathbf{F} \\ \mathbf{G} \end{bmatrix} \tag{2.55}$$

or

$$\mathbf{A}_c \mathbf{f}_c = \mathbf{F}_c \tag{2.56}$$

where,

$$\mathbf{A}_c = \begin{bmatrix} \mathbf{A} & \mathbf{B}^T \\ \mathbf{B} & \mathbf{0} \end{bmatrix}, \quad \mathbf{f}_c = \begin{bmatrix} \mathbf{f} \\ \boldsymbol{\lambda} \end{bmatrix} \quad \text{and } \mathbf{F}_c = \begin{bmatrix} \mathbf{F} \\ \mathbf{G} \end{bmatrix}$$

in which $\mathbf{A}$, $\mathbf{F}$ are defined in (2.13) and (2.14), respectively. The matrix $\mathbf{B} \in \mathbb{R}^{(M^t \times N^t)}$,

$$[\mathbf{B}]_{ij} = B(\Phi_j, \Psi_i) = \langle \Psi_i, \mathscr{L}_c \Phi_j - g_{c,j} \rangle \tag{2.57}$$

for $1 \leq i \leq N^t$ and $1 \leq j \leq M^t$.

The vectors $\boldsymbol{\lambda}$, $\mathbf{G} \in \mathbb{R}^{(M^t \times 1)}$, the matrix $\mathbf{A}_c \in \mathbb{R}^{(N^t+M^t)\times(N^t+M^t)}$, and the vectors $\mathbf{f}_c$, $\mathbf{F}_c \in \mathbb{R}^{(N^t+M^t)\times 1}$.

The solution to Eq.(2.55) corresponds to a saddle point [7, 12, 77]. In this saddle point problem, the Ladyzhenskaja-Babuška-Brezzi (LBB) condition commonly referred to as the (discrete) *inf-sup* condition owing to the equivalent form yields

$$\inf_{\lambda_N \in M_N, \lambda_N \neq 0} \sup_{f_N \in X_N, f_N \neq 0} \frac{B(f_N, \lambda_N)}{\|f_N\|_X \|\lambda_N\|_M} \geq K_b \tag{2.58}$$

in which K_b is a positive constant, must be satisfied.

The discrete space for the Lagrange multiplier, λ, needs to be particularly chosen to render a stable discretization. In addition, in order to satisfy the discrete *inf-sup* condition, the equal-order interpolation of the variable f should not be used [77].

The constrained least-squares method is applied in chapter 4 to formulate a mass conservative population balance equation. The author proposes a least-squares spectral element method which allows for incorporating the disperse phase mass-conservation (in the form of a continuity equation for the disperse phase) by means of the Lagrange multipliers method. Then, the population balance equation is solved under this additional constraint by finding the saddle point of the coupled system.

Chapter 3

The Multi-Fluid Model

Bubble columns are contactors in which a dispersed gas phase in the form of bubbles moves relatively to the continuous liquid phase. The need to establish a rational basis for the interpretation of the interaction of fluid dynamic variables requires sophisticated multiphase flow models. Various approaches have been suggested for solving the same fundamental flow problem and modeling may be attempted at various levels such as the fully resolved bubble model [90]; the Eulerian-Lagrangian discrete bubble model [9, 18, 19] and the Eulerian-Eulerian continuum models [26, 45, 72, 85].

In the present chapter, we put our emphasis on the basis of the multiphase transport theorem and derivation of the Eulerian-Eulerian multi-fluid model, as well as its solution approaches by different numerical methods. In particular, a one-dimensional cross-sectional averaged two-fluid model solved by the LSSEM is presented.

3.1 Transport theorem with a dividing surface

Let's look at a material control volume (CV) Ω that contains two different phases separated by an interface Σ that is illustrated in Figure 3.1. We represent the phase interface as a dividing surface, a surface at which one or more quantities such as density and velocity are discontinuous. In general, a dividing surface is not material; it is common for mass to be transferred across it. We assume that this dividing surface may be in motion through the material with an arbitrary speed of displacement [84]. If $\mathbf{v}_I$ denotes the velocity of a point on the surface, $\mathbf{v}_I \cdot \mathbf{n}_I^+$ is the speed of displacement of the surface measured in the direction $\mathbf{n}_I^+$ as illustrated in Figure 3.1, and $\mathbf{v}_I \cdot \mathbf{n}_I^-$ is the speed of displacement of the surface measured in the direction $\mathbf{n}_I^-$.

The quantities Ψ and $\mathbf{v}$ are assumed to be continuously differentiable in the regions Ω^+ and Ω^-. Since in general the dividing surface Σ is not material, the regions Ω^+ and Ω^-

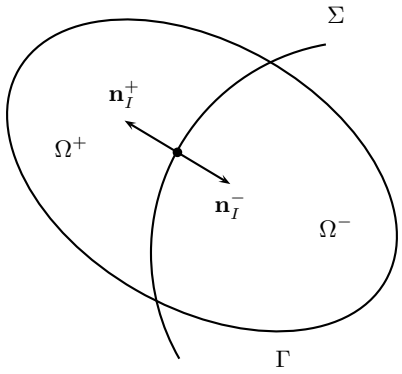

Figure 3.1: Region containing a dividing surface Σ.

are not material. We may write

$$\frac{d}{dt}\int_{\Omega_{(m)}} \Psi\, dV = \frac{d}{dt}\int_{\Omega^+} \Psi\, dV + \frac{d}{dt}\int_{\Omega^-} \Psi\, dV \tag{3.1}$$

By (m) we mean that the control volume and its boundary are material. To each term on the right of (3.1), we may apply the general transport theorem in the form of (3.2)

$$\frac{d}{dt}\int_{\Omega_{(m)}} \Psi\, dV = \int_{\Omega_{(m)}} \frac{\partial \Psi}{\partial t}\, dV + \int_{\Gamma_{(m)}} \Psi \mathbf{v}\cdot\mathbf{n}\, dA, \tag{3.2}$$

to obtain

$$\frac{d}{dt}\int_{\Omega^+} \Psi\, dV = \int_{\Omega^+} \frac{\partial \Psi}{\partial t}\, dV + \int_{\Gamma^+} \Psi \mathbf{v}\cdot\mathbf{n}\, dA - \int_{\Sigma} \Psi^+ \mathbf{v}_I\cdot\boldsymbol{\xi}^+\, dA \tag{3.3}$$

and

$$\frac{d}{dt}\int_{\Omega^-} \Psi\, dV = \int_{\Omega^-} \frac{\partial \Psi}{\partial t}\, dV + \int_{\Gamma^-} \Psi \mathbf{v}\cdot\mathbf{n}\, dA - \int_{\Sigma} \Psi^- \mathbf{v}_I\cdot\boldsymbol{\xi}^-\, dA \tag{3.4}$$

Ψ^+ and Ψ^- mean the limits of the function Ψ obtained as any point $\mathbf{z}$ approaches a point $\mathbf{z}_0$ on Σ while remaining within R^+ and R^-, respectively.

Substituting these expressions into (3.1), we conclude that

$$\begin{aligned}\frac{d}{dt}\int_{\Omega(m)} \Psi\, dV &= \int_{\Omega(m)} \frac{\partial \Psi}{\partial t}\, dV + \int_{\Gamma(m)} \Psi \mathbf{v}\cdot\mathbf{n}\, dA - \int_{\Sigma} \Psi^+ \mathbf{v}_I\cdot\mathbf{n}_I^+ + \Psi^- \mathbf{v}_I\cdot\mathbf{n}_I^-\, dA \\ &= \int_{\Omega(m)} \frac{\partial \Psi}{\partial t}\, dV + \int_{\Gamma(m)} \Psi \mathbf{v}\cdot\mathbf{n}\, dA - \int_{\Sigma} \left[\Psi \mathbf{v}_I\cdot\mathbf{n}_I\right]\, dA \end{aligned} \tag{3.5}$$

where the box brackets denote the jump of the quantity enclosed across the interface:

$$[A\mathbf{n}_I] \equiv A^+\mathbf{n}_I^+ + A^-\mathbf{n}_I^- \tag{3.6}$$

The Ψ^+ and Ψ^- represent the limits of the function Ψ obtained as any point $\mathbf{r}$ approaches a point $\mathbf{r}_0$ on Σ while remaining within Ω^+ and Ω^-, respectively.

We then use the Green's theorem to transfer the surface integral term on the r.h.s. of Eq.(3.5) [1] into a volume integral, which gives,

$$\int_{\Gamma_{(m)}} \Psi \mathbf{v} \cdot \mathbf{n} dA = \int_{\Omega_{(m)}} \nabla \cdot (\Psi \mathbf{v}) \; dV + \int_{\Sigma} [\Psi \mathbf{v} \cdot \mathbf{n}_I] dA. \tag{3.11}$$

Finally, we can use (3.11) to rewrite (3.5) as

$$\frac{d}{dt} \int_{\Omega_{(m)}} \Psi dV = \int_{\Omega_{(m)}} \left[\frac{\partial \Psi}{\partial t} + \nabla \cdot (\Psi \mathbf{v}) \right] dV + \int_{\Sigma} \left[\Psi (\mathbf{v} - \mathbf{v}_I) \cdot \mathbf{n}_I \right] dA \tag{3.12}$$

or

$$\frac{d}{dt} \int_{\Omega_{(m)}} \Psi dV = \int_{\Omega_{(m)}} \left[\frac{d_{(m)} \Psi}{dt} + \Psi \nabla \cdot \mathbf{v} \right] dV + \int_{\Sigma} \left[\Psi (\mathbf{v} - \mathbf{v}_I) \cdot \mathbf{n}_I \right] dA \tag{3.13}$$

An alternative form of the transform theorem for regions containing a dividing surface can be obtained by replacing Ψ with $\rho\psi$ in Eq.(3.13). Hence the generalized balance equation can be formulated like

$$\frac{d}{dt} \int_{\Omega_{(m)}} \rho \psi dV = \int_{\Omega_{(m)}} \rho \frac{d_{(m)} \psi}{dt} dV + \int_{\Sigma} \left[\rho \psi (\mathbf{v} - \mathbf{v}_I) \cdot \mathbf{n}_I \right] dA. \tag{3.14}$$

---

[1] The Green's theorem:

$$\int_{\Omega} \nabla \cdot \Psi \; dV = \int_{\Gamma} \Psi \mathbf{n} \, dA \tag{3.7}$$

Applying (3.7) for Ω^+ and Ω^-, respectively.

$$\int_{\Omega^+} \nabla \cdot (\Psi \mathbf{v}) \; dV = \int_{\Gamma^+} \Psi \mathbf{v} \cdot \mathbf{n} dA - \int_{\Sigma} \Psi^+ \mathbf{v} \cdot \boldsymbol{\xi}^+ \, dA \tag{3.8}$$

and

$$\int_{\Omega^-} \nabla \cdot (\Psi \mathbf{v}) \; dV = \int_{\Gamma^-} \Psi \mathbf{v} \cdot \mathbf{n} dA - \int_{\Sigma} \Psi^- \mathbf{v} \cdot \boldsymbol{\xi}^- \, dA. \tag{3.9}$$

The sum of these two expressions gives

$$\begin{aligned} \int_{\Omega_{(m)}} \nabla \cdot (\Psi \mathbf{v}) \; dV &= \int_{\Gamma_{(m)}} \Psi \mathbf{v} \cdot \mathbf{n} dA - \int_{\Sigma} \left(\Psi^+ \mathbf{v} \cdot \boldsymbol{\xi}^+ + \Psi^- \mathbf{v} \cdot \boldsymbol{\xi}^- \right) \, dA \\ &= \int_{\Gamma_{(m)}} \Psi \mathbf{v} \cdot \mathbf{n} dA - \int_{\Sigma} [\Psi \mathbf{v} \cdot \boldsymbol{\xi}] dA. \end{aligned} \tag{3.10}$$

3.2 Governing equations and jump conditions

The transport theorem (3.14) is important for deriving the mass and momentum balance equations of a CV with a dividing surface. The differential mass balance expresses the requirements that mass is conserved, and the momentum balance expresses that the time of change rate of the momentum is equal to the sum of the forces acting on the body at every point within a continuous material. The implication of the mass and momentum balances at the interface are known as the *jump conditions*, which must be obeyed at each point on each phase interface. The mathematical expressions of the jump conditions are derived from the second term of the r.h.s of Eq.(3.14).

It is possible to write a general form of the equations of motion for the exact motions of the materials involved in the CV

$$\frac{\partial \rho\psi}{\partial t} + \nabla \cdot (\rho\psi\mathbf{v}) - \nabla \cdot \mathbf{J} = \rho f \tag{3.15}$$

with jump conditions

$$[\rho\psi(\mathbf{v} - \mathbf{v}_I) - \mathbf{J}] \cdot \mathbf{n}_I = m \tag{3.16}$$

The usual values for ψ, $\mathbf{J}$, f and m are given in Table 3.1.

Conservation	ψ	$\mathbf{J}$	f	m
Mass	1	0	0	0
Momentum	$\mathbf{v}$	$\mathbf{T}$	$\mathbf{f}$	$\mathbf{m}^\sigma$

Table 3.1: Variables in the generic conservation equation and the jump condition.

in which, $\mathbf{T}$ is a second-order stress tensor, $\mathbf{f}$ is the body force and $\mathbf{m}^\sigma$ is the jump momentum balance that is related to the imbalance of long-range intermolecular forces at a deformed interface.

The detailed derivations of the transport theorem in the form of Eq.(3.15) are referred to [26, 27].

3.3 Ensemble averaged governing equations

3.3.1 Introduction of the ensemble averaging

In this section we examine the ensemble averaging method in the framework of the generic single averaging procedure proposed by [27].

As distinct from the time and volume averaging procedures, the application of the ensemble averaging operator is not restricted by any space- and time scales.

Generally, an ensemble averaging is defined in terms of an infinite number of realizations of the flow, consisting of variations of position, configuration, and velocities of the discrete units and the fluid between them. This means that we imagine that one can measure a local instantaneous quantity for each of an infinity of experiments which are alike except for presumably unimportant details of their behavior, and obtain the averaged values by averaging the quantity over the ensemble. In practical, the ensemble averaging is computed over a sufficiently large but finite number of realizations to ensure that the average measures become stable and do not fluctuate significantly.

The ensemble average of ψ is defined by

$$\overline{\psi}(\mathbf{r}, t) = \int_{\varepsilon} \psi(\mathbf{r}, t; \mu)\, dm(\mu) \tag{3.17}$$

where $p(\mu)d\mu = dm(\mu)$ is the probability density for observing a realization μ in the interval $d\mu$ on the set of all possible events ε. From the definition of a probability density function we note:

$$\int_{\varepsilon} p(\mu)\, d\mu = 1 \tag{3.18}$$

It is often desirable to isolate each phase theoretically, even in the micro scale description. To do this, we introduce the *phase indicator function*, or *characteristic function*, $X_k(\mathbf{r}, t; \mu)$, in any realization μ. The characteristic function is defined by

$$X_k(\mathbf{r}, t; \mu) = \begin{cases} 1 & \text{if } \mathbf{r} \in \text{ phase } k \text{ in realization } \mu \\ 0 & \text{otherwise.} \end{cases} \tag{3.19}$$

in which, k is the phase index.

The particular forms of the Leibniz's and Gauss' rules used for ensemble averaging are given by

$$\overline{X_k \nabla \psi} = \overline{\nabla X_k \psi} - \overline{\psi \nabla X_k} \tag{3.20}$$

$$\overline{X_k \frac{\partial \psi}{\partial t}} = \overline{\frac{\partial X_k \psi}{\partial t}} - \overline{\psi \frac{\partial X_k}{\partial t}} \tag{3.21}$$

This is the *topological equation*

$$\frac{\partial X_k}{\partial t} + \mathbf{v}_I \cdot \nabla X_k = 0 \tag{3.22}$$

Note that it is the material derivative of X_k following the interface. If we look at a point that is not on the interface, then either $X_k = 1$ or $X_k = 0$. In either case, the partial derivatives both vanish, and hence the left side of the topological equation equals zero.

3.3.2 The fundamental balance equations

Averages of balance equations are obtained by taking the product of the balance equation (3.15) with X_k, then performing the averaging process. After rearranging, the generic ensemble averaging balance equation is obtained

$$\frac{\partial\overline{X_k\rho\psi}}{\partial t} + \nabla\cdot\overline{X_k\rho\psi\mathbf{v}} - \nabla\cdot\overline{X_k\mathbf{J}} - \overline{X_k\rho f} = \overline{\rho\psi\left(\frac{\partial X_k}{\partial t} + \mathbf{v}\cdot\nabla X_k\right) - \mathbf{J}\cdot\nabla X_k} \tag{3.23}$$

Subtracting the average of $\rho\psi$ with the result in (3.22) reduces the right-hand side of (3.23) to

$$\overline{(\rho\psi(\mathbf{v}-\mathbf{v}_I)-\mathbf{J})\cdot\nabla X_k} \tag{3.24}$$

This is the interfacial source of ψ. It is due to phase change, $(\mathbf{v}-\mathbf{v}_I)\cdot\mathbf{n}_I \neq 0$, and to the flux $\mathbf{J}$.

3.3.3 Averaged balance equations

Averaged balance equations

All the variables are defined in terms of weighted averages. The main, or "component" variables are either component weighted variables, that is, weighted with the component function X_k or mass-weighted (or Favré) averaged, that is, weighted by $X_k\rho$.

$$\frac{\partial(\alpha_k\overline{\rho}_k^{x\rho})}{\partial t} + \nabla\cdot(\alpha_k\overline{\rho}_k^{x}\overline{\mathbf{v}}_k^{x\rho}) = \Gamma_k \tag{3.25}$$

$$\begin{aligned}\frac{\partial(\alpha_k\overline{\rho}_k^{x}\overline{\mathbf{v}}_k^{x\rho})}{\partial t} + \nabla\cdot(\alpha_k\overline{\rho}_k^{x}\overline{\mathbf{v}}_k^{x\rho}\overline{\mathbf{v}}_k^{x\rho}) =& \nabla\cdot\left(\alpha_k(\overline{\mathbf{T}}_k^{x} + \mathbf{T}_k^{Re})\right) + \alpha_k\overline{\rho}_k^{x}\overline{\mathbf{f}}_k^{x\rho} \\ &+ \mathbf{M}_k + \mathbf{v}_{kI}^{m}\Gamma_k\end{aligned} \tag{3.26}$$

where the average of X_k is the average fraction of the occurrences of component k at certain point at time t, which is customary to be called the volume fraction.

$$\alpha_k = \overline{X_k} \tag{3.27}$$

and,

$$\overline{\rho}_k^{x} = \frac{\overline{X_k\rho}}{\alpha_k}, \quad \overline{\mathbf{v}}_k^{x\rho} = \frac{\overline{X_k\rho\mathbf{v}}}{\alpha_k\overline{\rho}_k^{x}}, \quad \overline{\mathbf{T}}_k^{x} = \frac{\overline{X_k\mathbf{T}}}{\alpha_k}, \quad \overline{\mathbf{f}}_k^{x\rho} = \frac{\overline{X_k\rho\mathbf{f}}}{\alpha_k\overline{\rho}_k^{x}}, \tag{3.28}$$

Interfacial momentum source are defined by

$$\mathbf{M}_k = -\overline{\mathbf{T}\cdot\nabla X_k}, \tag{3.29}$$

Terms caused by fluctuating field:

$$\begin{aligned}\overline{X_k\rho\mathbf{v}\mathbf{v}} &= \overline{X_k\rho(\overline{\mathbf{v}}_k^{x\rho}+\mathbf{v}'_k)(\overline{\mathbf{v}}_k^{x\rho}+\mathbf{v}'_k)} = \overline{X_k\rho}\overline{\mathbf{v}}_k^{x\rho}\overline{\mathbf{v}}_k^{x\rho}+\overline{X_k\rho\mathbf{v}'_k\mathbf{v}'_k} \\ &= \alpha_k\overline{\rho}_k^x\overline{\mathbf{v}}_k^{x\rho}\overline{\mathbf{v}}_k^{x\rho}-\alpha_k\mathbf{T}_k^{Re} \end{aligned} \tag{3.30}$$

where $\mathbf{T}_k^{Re}$ is the Reynolds stress: $\mathbf{T}_k^{Re} = -\frac{\overline{X_k\rho\mathbf{v}'_k\mathbf{v}'_k}}{\alpha_k}$.

Several terms appear representing the actions of the convective and molecular fluxes at the interface. These terms are interfacial mass source, momentum source:

$$\begin{aligned}\Gamma_k &= \overline{\rho(\mathbf{v}-\mathbf{v}_I)\cdot\nabla X_k} \\ \mathbf{v}_{kI}^m\Gamma_k &= \overline{\rho\mathbf{v}(\mathbf{v}-\mathbf{v}_I)\cdot\nabla X_k}\end{aligned}$$

Manipulations

We now give a few miscellaneous relations for the interfacial transfer terms. Generally, we wish to write the stress as a pressure plus a shear stress,

$$\mathbf{T} = -P\mathbf{I}+\boldsymbol{\tau} \tag{3.31}$$

Then the average stress can be written as

$$\overline{\mathbf{T}}_k^x = -\overline{P}_k^x\mathbf{I}+\overline{\boldsymbol{\tau}}_k^x \tag{3.32}$$

The average interfacial pressure P_{kI} and shear stress $\boldsymbol{\tau}_{kI}$ are introduced to separate mean field effects from local effects in the interfacial forces.

$$P_k = P_{kI}+P'_{kI} \tag{3.33}$$

$$\boldsymbol{\tau}_k = \boldsymbol{\tau}_{kI}+\boldsymbol{\tau}'_{kI} \tag{3.34}$$

The interfacial force density can be written as

$$\mathbf{M}_k = -\overline{\mathbf{T}\cdot\nabla X_k} = P_{kI}\overline{\nabla X_k}-\boldsymbol{\tau}_{kI}\cdot\overline{\nabla X_k}+\mathbf{M}_{kI} \tag{3.35}$$

where we define the generalized interfacial momentum

$$\mathbf{M}_{kI} = \mathbf{M}_k - P_{kI}\nabla\alpha_k+\boldsymbol{\tau}_{kI}\cdot\nabla\alpha_k \tag{3.36}$$

and introduce

$$\mathbf{T}'_{kI} = -P'_{kI}\mathbf{I}+\boldsymbol{\tau}'_{kI} = -(P_k-P_{kI})\mathbf{I}+(\boldsymbol{\tau}_k-\boldsymbol{\tau}_{kI}) \tag{3.37}$$

The Reynolds stress tensor of the k phase, $\mathbf{T}_k^{Re}$, in Eq.(3.26) is modeled using a generalized Boussinesq approximation

$$\begin{aligned}\mathbf{T}_k^{Re} &= -\overline{\rho}_k^x \overline{\mathbf{v}_k' \mathbf{v}_k'} = -\frac{2}{3}\overline{\rho}_k^x k_k \mathbf{I} + \boldsymbol{\tau}_k^{Re} \\ &= -\frac{2}{3}\overline{\rho}_k^x k_k \mathbf{I} + \mu_{\text{tur},k}\left(\nabla \overline{\mathbf{v}}_k^{x\rho} + (\nabla \overline{\mathbf{v}}_k^{x\rho})^{\mathrm{T}} - \frac{2}{3}\mathbf{I}(\nabla \cdot \overline{\mathbf{v}}_k^{x\rho})\right)\end{aligned} \tag{3.38}$$

The dynamic turbulent viscosity of the phase k, $\mu_{\text{tur},k}$, is defined by $\mu_{\text{tur},k} = 2\overline{\rho}_k^x k_k \boldsymbol{\tau}_k^t/3$, and the time scale of the large eddies, $\boldsymbol{\tau}_k^t$, by $\boldsymbol{\tau}_k^t = \frac{2}{3}C_\mu k_k/\varepsilon_k$. The turbulent kinetic energy per unit mass of phase k, k_k, is defined by

$$k_k = \frac{1}{2}\overline{\mathbf{v}_k' \mathbf{v}_k'} \tag{3.39}$$

Note that the first term of the right-hand side of the generalized Boussinesq approximation Eq.(3.38) is normally neglected. Therefore by using (3.36) and (3.38), we rewrite the right-hand side of (3.26) as:

$$\begin{aligned}&\nabla \cdot \left(\alpha_k(\overline{\mathbf{T}}_k^x + \mathbf{T}_k^{Re})\right) + \alpha_k \overline{\rho}_k^x \overline{\mathbf{f}}_k^{x\rho} + \mathbf{M}_k + \mathbf{v}_{kI}^m \Gamma_k \\ =& -\alpha_k \nabla \overline{P}_k^x + \nabla \cdot \left(\alpha_k(\overline{\boldsymbol{\tau}}_k^x + \overline{\boldsymbol{\tau}}_k^{Re})\right) + \alpha_k \overline{\rho}_k^x \overline{\mathbf{f}}_k^{x\rho} + \mathbf{M}_{kI} + \mathbf{v}_{kI}^m \Gamma_k \\ &- (\overline{P}_k^x - P_{kI})\nabla \alpha_k - \boldsymbol{\tau}_{kI} \cdot \nabla \alpha_k\end{aligned} \tag{3.40}$$

where the last two terms are referred to as the interfacial pressure difference effect and the combined interfacial shear and void gradient effect, respectively. The interfacial pressure difference effect is believed to be insignificant for the two-fluid model and the combined interfacial shear and void gradient effect is generally ignored for dispersed flows, i.e. for type of flow considered here. The term $\mathbf{v}_{kI}^m \Gamma_k$ representing the abrupt interfacial momentum transport which is used in nuclear engineering, and not very often encountered in chemical engineering. It is set to zero in this work. Thus the right-hand side of (3.26) can be simpled as

$$-\alpha_k \nabla \overline{P}_k^x + \nabla \cdot \left(\alpha_k(\overline{\boldsymbol{\tau}}_k^x + \overline{\boldsymbol{\tau}}_k^{Re})\right) + \alpha_k \overline{\rho}_k^x \overline{\mathbf{f}}_k^{x\rho} + \mathbf{M}_{kI} \tag{3.41}$$

Therefore we rewrite the averaged momentum balance equation Eq.(3.26) as

$$\begin{aligned}\frac{\partial(\alpha_k \overline{\rho}_k^x \overline{\mathbf{v}}_k^{x\rho})}{\partial t} + \nabla \cdot (\alpha_k \overline{\rho}_k^x \overline{\mathbf{v}}_k^{x\rho} \overline{\mathbf{v}}_k^{x\rho}) =& -\alpha_k \nabla \overline{P}_k^x + \nabla \cdot \left(\alpha_k(\overline{\boldsymbol{\tau}}_k^x + \overline{\boldsymbol{\tau}}_k^{Re})\right) \\ &+ \alpha_k \overline{\rho}_k^x \overline{\mathbf{f}}_k^{x\rho} + \mathbf{M}_{kI}\end{aligned} \tag{3.42}$$

For convenience, in the following part of the thesis, we shall drop the averaging sign from each averaged variable.

3.4 Closures

The multifluid model represents a direct extension of the well-known two-fluid model and is described in detailed in [11, 60, 74, 88]. The governing set of equations consists of the continuity and momentum equations for $N + 1$ phases; one phase corresponds to the liquid phase and the remaining N phases are gas bubble phases.

The fundamental form of the multifluid continuity equation and momentum equations for phase k reads

$$\frac{\partial}{\partial t}(\alpha_k \rho_k) + \nabla \cdot (\alpha_k \rho_k \mathbf{v}_k) = \sum_{l=1}^{N} \Gamma_{k,l} \tag{3.43}$$

$$\begin{aligned}\frac{\partial}{\partial t}(\alpha_k \rho_k \mathbf{v}_k) + \nabla \cdot (\alpha_k \rho_k \mathbf{v}_k \mathbf{v}_k) = &- \alpha_k \nabla P_k + \nabla \cdot \left(\alpha_k (\boldsymbol{\tau}_k + \boldsymbol{\tau}_k^{Re})\right) \\ &+ \alpha_k \rho_k \mathbf{f}_k + \mathbf{M}_{k,l}\end{aligned} \tag{3.44}$$

The right-hand side of Eq.(3.43) describes the net mass-transfer flux to phase k from all other phases l, while the last term on the right-hand side of Eq.(3.44) accounts for all momentum-transfer fluxes between phase k and the other N phases.

The phases volume fractions also satisfy the compatibility condition

$$\sum_{k=1}^{N+1} \alpha_k = 1 \tag{3.45}$$

When sufficiently dilute dispersions are considered, only particle-fluid interactions are significant, and the two-fluid closures can be adopted. For the gas bubble phases ($k = d$), the interaction with the continuous liquid phase ($k = c$) and the wall ($k = w$) through the last term on the right-hand side of Eq.(3.44) is expressed as

$$\begin{aligned}\mathbf{M}_{d,l} &\approx \mathbf{M}_{d,c} + \mathbf{M}_{d,w} = \mathbf{F}_d \\ &= \mathbf{M}_d^D + \mathbf{M}_d^V + \mathbf{M}_d^L + \mathbf{M}_d^{TD} + \mathbf{M}_d^W\end{aligned} \tag{3.46}$$

i.e., the sum of steady-drag, added-mass, lift, turbulent diffusion, and wall forces, respectively.

The net interfacial momentum-transfer term for the liquid phase (i.e., excluding the wall forces) can be written as

$$\mathbf{M}_{c,d} = -\mathbf{M}_{d,c} \tag{3.47}$$

The drag force is given by

$$\mathbf{M}_d^D = -F_{D,d}(\mathbf{v}_d - \mathbf{v}_c) = \frac{3}{4\xi_{32,d}} \alpha_d \rho_c C_{D,d} |\mathbf{v}_d - \mathbf{v}_c| (\mathbf{v}_d - \mathbf{v}_c) \tag{3.48}$$

The drag coefficient can be estimated using the relation suggested by [88]

$$C_{D,d} = \max\left\{\min\left[\frac{A_D}{Re_{B,d}}\left(1+0.15Re_{B,d}^{0.687}\right), \frac{3A_D}{Re_{B,d}}\right], \frac{3Eo_d}{8(Eo_d+4)}\right\} \tag{3.49}$$

For pure systems, the parameter $A_D = 16$, whereas for contaminated systems $A_D = 24$. The *Eötvös number* number, Eo_d is given as

$$Eo_d = \frac{g_z|\rho_c - \rho_d|\xi_{32,d}^2}{\sigma_l} \tag{3.50}$$

and $Re_{B,d}$ is the particle *Reynolds number*

$$Re_{B,d} = \frac{\rho_c \xi_{32,d}|\mathbf{v}_d - \mathbf{v}_c|}{\mu_c} \tag{3.51}$$

The acceleration of the liquid in the wake of the bubble can be taken into account through the added-mass force given by Ishii and Mishima [41]

$$\mathbf{M}_d^V = -\alpha_d \rho_c C_{V,d}\left(\frac{d\mathbf{v}_d}{dt} - \frac{d\mathbf{v}_c}{dt}\right) \tag{3.52}$$

where $C_{V,d} = 0.5$ is derived for potential flow.

The lift force on the dispersions phase due to shear in the liquid phase is expressed as

$$\mathbf{M}_d^L = \alpha_d \rho_c C_{L,d}(\mathbf{v}_d - \mathbf{v}_c) \times (\nabla \times \mathbf{v}_c) \tag{3.53}$$

where $C_{L,d} = 0.5$ is derived for potential flow.

The dispersion of bubbles in turbulent liquid flow can be modeled as suggested by [11]

$$\mathbf{M}_d^{TD} = \frac{\nu_{c,t}}{\alpha_d Sc_{t,d}} F_{D,d} \nabla \alpha_d \tag{3.54}$$

where the *Schmidt number* is defined as $Sc_{t,d} = \nu_{c,t}/\nu_{d,t}$.

An additional lift force that pushes the dispersed phase away from the wall was suggested by [2] to be given by

$$\mathbf{M}_d^W = \max\left(0, C_{w1} + C_{w2}\frac{\xi_{32,d}}{y}\right)\alpha_d \rho_c \frac{|\mathbf{v}_d - \mathbf{v}_c|^2}{\xi_{32,d}}\mathbf{n}_w \tag{3.55}$$

where $C_{w1} = -0.1$ and $C_{w1} = 0.35$. This force, Eq.(3.55), represents an extension of the original model of Antal et al [1]. A defect in the original model, namely, that a bubble located far from the wall is attracted to the wall, has been removed.

3.5 A cross-sectional averaged two-fluid model

The cross-sectional averaged two-fluid model is developed by applying the cross-sectional area averaging operator on the two-phase transport equations([43], Chapter 3). Both liquid and gas flows are considered as steady-state, laminar flow. Therefore, the lift force M_d^L and the virtual mass force M_d^L in Eq.(3.46) vanish. The viscosity is assumed as constant. By neglecting the interfacial mass transfer, the mass balance equation for each phase can be expressed as:

$$\frac{\partial}{\partial z}(\alpha_d \rho_d) + \frac{\partial}{\partial z}(\alpha_d v_d) = 0 \tag{3.56}$$

$$\frac{\partial}{\partial z}(\alpha_c \rho_c) + \frac{\partial}{\partial z}(\alpha_c v_c) = 0 \tag{3.57}$$

The momentum equation for each phase are:

$$\begin{aligned}\frac{\partial(\alpha_d \rho_d v_d)}{\partial t} + \frac{\partial}{\partial z}(\alpha_d \rho_d v_d v_d) + \alpha_d \frac{\partial p_d}{\partial z} =& -\mu_d \frac{\partial}{\partial z}\left(\alpha_d \frac{\partial v_d}{\partial z}\right) + \alpha_d \rho_d g \\ &+ K_d(v_d - v_c) \end{aligned} \tag{3.58}$$

$$\begin{aligned}\frac{\partial(\alpha_c \rho_c v_c)}{\partial t} + \frac{\partial}{\partial z}(\alpha_c \rho_c v_c v_c) + \alpha_c \frac{\partial p_c}{\partial z} =& -\mu_c \frac{\partial}{\partial z}\left(\alpha_c \frac{\partial v_c}{\partial z}\right) + \alpha_c \rho_c g \\ &- K_d(v_d - v_c) \end{aligned} \tag{3.59}$$

where ρ is density, μ is viscosity, p is pressure and g is the gravity acceleration. K_d is the pre-multiplier in the drag force term

$$K_d = \frac{3}{4}\frac{C_D}{d_d}\alpha_d \rho_c |v_d - v_c| \tag{3.60}$$

The summation of the phase volumes must recover the whole domain, so that the fractions of the phases are coupled by the following relation:

$$\alpha_d + \alpha_c = 1 \tag{3.61}$$

It is assumed that the pressure in the gas phase is equal to that in the liquid phase:

$$p_d = p_c = p \tag{3.62}$$

The boundary conditions of the problem is as follows:

$$\alpha_d|_{z=0} = \alpha_{g,0} \tag{3.63}$$

$$v_d|_{z=0} = v_{g,0} \tag{3.64}$$

$$u_d|_{z=L} = 0 \tag{3.65}$$

$$v_c|_{z=0} = v_{l,0} \tag{3.66}$$

$$u_c|_{z=L} = 0 \tag{3.67}$$

$$p|_{z=0} = p_0 \tag{3.68}$$

3.6 Numerical methods for solving multi-fluid model

3.6.1 Finite volume method

By virtue of Eq.(3.15), the generalized balance equation in terms of extensive quantity $\Psi = \rho\psi$ can be written as

$$\frac{\partial \Psi(\mathbf{r},t)}{\partial t} = -\nabla \cdot (\Psi(\mathbf{r},t)\mathbf{v}(\mathbf{r},t)) - \nabla \cdot \mathbf{J} + S \tag{3.69}$$

where, $\mathbf{v}$ is a given velocity field, $\mathbf{J}$ is the diffusive flux, and $S = \rho f$ is the source term.

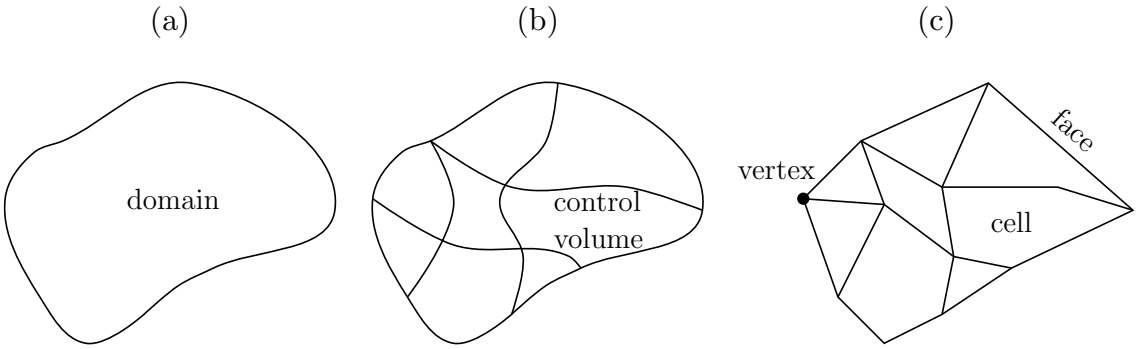

Figure 3.2: In the FVM, physical domain (a) can be divided into a set of arbitrary control volumes (b) and polyhedral control volumes (c).

The general balance equation (3.69) is to be solved in a given spatial domain that can be sub-divided into finite volumes or cells (Figure 3.2). For a particular cell, i, we take the volume integral of Eq.(3.69) over the total volume of the cell, V_P, and apply the Gauss's theorem, which gives,

$$\begin{aligned}\frac{\partial}{\partial t}\int_{V_P} \Psi(\mathbf{r},t)\, dV = &-\int_{A_P} \Psi(\mathbf{r},t)\mathbf{v}(\mathbf{r},t)\cdot\mathbf{n}\, dA - \int_{A_P} \mathbf{J}\cdot\mathbf{n}\, dA \\ &+ \int_{V_P} S(\Psi,\mathbf{r},t)\, dV\end{aligned} \tag{3.70}$$

where A_P represents the total surface area of the cell and $\mathbf{n}$ is a unit vector normal to the surface and pointing outward. Using the mean value integral and splitting the integral of the total fluxes through the neighbor shared surfaces, Eq.(3.70) can be written as

$$\frac{\partial \bar{\Psi}_P}{\partial t}\Delta V_P = -\sum_{nb_P} \bar{\Psi}_{nb_P}\mathbf{v}_{nb_P}\cdot\mathbf{n}\Delta A_{nb_P} - \sum_{nb_P} \overline{\mathbf{J}_P\cdot\mathbf{n}}\Delta A_{nb_P} + \bar{S}_P\Delta V_P \tag{3.71}$$

Here, the bar represents the mean value. For the fluxes, the mean value is to be intended as mean value at the surface whereas for the other terms, derived from the volume integral, as

mean value at the CV. The subscript nb_P denotes the neighbor CVs of the control volume P.

The discretized multi-fluid model equations can be written in implicit form as *Mass conservation*

$$A_{P,\alpha_k}\alpha_{P,k}^{n+1} = \sum_{nb_P} A_{nb_P,\alpha_k}\alpha_{nb_P,k}^{n+1} + S_{P,\alpha_k}^{n+1} \tag{3.72}$$

with

$$\sum_{k=1}^{N} \alpha_k^{n+1} = 1 \tag{3.73}$$

Phase momentum balance equations

$$\begin{aligned} A_{P,u_k}U_{P,k}^{n+1} =& \sum_{nb_P} A_{nb_P,u_k}U_{nb_P,k}^{n+1} + d_x(\delta_x p)^{n+1} + S_{P,u_k}^{n+1} \\ &+ \sum_{i=1}^{N} C_{ik}\left(U_{P,i}^{n+1} - U_{P,k}^{n+1}\right) \end{aligned} \tag{3.74}$$

$$\begin{aligned} A_{P,v_k}V_{P,k}^{n+1} =& \sum_{nb_P} A_{nb_P,v_k}V_{nb_P,k}^{n+1} + d_x(\delta_y p)^{n+1} + S_{P,v_k}^{n+1} \\ &+ \sum_{i=1}^{N} C_{ik}\left(V_{P,i}^{n+1} - V_{P,k}^{n+1}\right) \end{aligned} \tag{3.75}$$

$$\begin{aligned} A_{P,w_k}W_{P,k}^{n+1} =& \sum_{nb_P} A_{nb_P,w_k}W_{nb_P,k}^{n+1} + d_x(\delta_z p)^{n+1} + S_{P,w_k}^{n+1} \\ &+ \sum_{i=1}^{N} C_{ik}\left(W_{P,i}^{n+1} - W_{P,k}^{n+1}\right) \end{aligned} \tag{3.76}$$

Here, U, V and W are the component of the velocity along the x, y and z axis, δ_x, δ_y and δ_z represent finite difference in the x, y and z directions and C_{ik} is the drag coefficient between phase i and phase k. The other interfacial forces (lift, virtual mass, etc.) are accounted for in the source term S.

In fully implicit discretization, the coefficients A, d, C and the source term S are functions of the unknowns (p_k^{n+1}, α_k^{n+1}, $\mathbf{v}_k^{n+1}$).

When the FVM deals with the $p-\mathbf{v}-\alpha$ links, a segregated Picard like iteration is normally applied so that the α is set to a fixed preliminarily field when iterating on the $p-\mathbf{v}$ fields, and then in the following iteration on α another Picard iteration is used thus $p-\mathbf{v}$ are preliminarily set to fixed fields when interating on α. Some modern CFD codes like CFX abandoned this segregated procedure. CFX uses a coupled solution strategy solving most of the equations simultaneously, however some linearization is still required [43, 44].

Numerical issues

The finite volume method solution of the multiphase flow equations as well as for single phase are complicated by the lack of an independent equation for the pressure, whose gradient contributes to each of the momentum equations.

By analogy with single phase flows, where the pressure field is constructed in such a way to satisfy continuity [13, 29, 92], in multiphase flows the pressure is determined so that the total continuity or the continuity of one of the phases is conserved.

Two iterative methods based on the pressure correction approach are (i) the semi-implicit pressure linked equation (SIMPLE) method [73] and (ii) the inter-phase slip algorithm (IPSA), which is an extension of SIMPLE to multi-fluid model equations [86].

The SIMPLE is an iterative algorithm widely used in CFD commercial codes to solve pressure-velocity coupling problems. It defines corrections of pressure and each of the velocity components, which are the discrepancies between the correct values and guessed values. A linearized system of equations in the unknowns of pressure correction is derived by inserting the defined correction terms into the discrete mixture continuity.

The computation starts with a guessed pressure field, which is used to compute the velocity. The velocity obtained does not satisfy, in general, total mass conservation in each CV. The pressure is then corrected from the pressure correction equation in such a way that the derived velocity field restores total mass conservation. The under-relaxation is used in the pressure correction equations or even in the velocity components to grantee convergence.

The IPSA is an extension of SIMPLE in which a momentum equation for each phase needs to be solved and the pressure-velocity link depends on the interfacial forces too. The pressure correction is still derived from the conservation of the total mass, which is equivalent to the mixture continuity equations. However, the pressure correction is related to the velocity correction of each phase instead of the mixture velocity.

When solving the phase mass conservation equations in both mixture and multi-fluid models, it may happen that the constraint on the volume fraction given by Eq.(3.73) is not satisfied. It is due to the approximated values of the velocity and density (or guessed values) used to compute the coefficients and the source term of the equations. To avoid this problem, the volume fractions are usually normalized after the computation [97] in an either implicit or explicit manner.

The normalized volume fractions may satisfy the momentum balance and the total mass conservation even though mass conservation for each phase is not. It's usually not possible to ensure both total mass conservation and separate phase mass conservation. In the case of the implicit discretization, this problem can be treated solving the mass conservation equations iteratively until the computed and the normalized volume fractions are close enough under a given tolerance.

The strong phase coupling due to the large drag coefficients exists in the momentum

balance equations needs special attention. A method to improve the convergence rate of the momentum balance equation solution is the partial elimination algorithm (PEA) [64, 70, 86]. It aims to weaken the strong coupling between the phases by algebraic cross substitution of the velocities in the drag term or by partial elimination of the velocities. The resulting system shows a faster convergence than the original homologous coupled system.

It worthwhile to mention that the numerical discretization of the convective terms in both the volume fraction equations and the momentum equations introduces error propagation. The commonly used first-order upwinding scheme is responsible for the numerical diffusion. Additionally, in a spectral analysis of the signals, the upwinding scheme used in the momentum transport equations tends to remove the higher frequency of the signal [8].

3.6.2 The least-squares spectral element method

We now make a steady-state assumption on the cross-sectional bubble column presented in section 3.5 and use the LSSEM to solve it. In order to obtain a least-squares formulation, the cross-sectional averaged two-fluid model is first transformed into a system of first order partial differential equations by introducing two new variables defined equal to the derivatives of velocity of each phase

$$u_d = \frac{dv_d}{dz} \tag{3.77}$$

$$u_c = \frac{dv_c}{dz} \tag{3.78}$$

and by using the volume fraction constraint (3.61), the governing equations subsequently read

$$\begin{aligned} \alpha_d\frac{dp}{dz} + K_d v_d - K_d v_c =& -\rho_d\alpha_d v_d\frac{dv_d}{dz} + \mu_d\alpha_d\frac{du_d}{dz} \\ &+ \mu_d u_d\frac{d\alpha_d}{dz} - \alpha_d\rho_d g \end{aligned} \tag{3.79}$$

$$\begin{aligned} (1-\alpha_d)\frac{dp}{dz} + K_d v_c - K_d v_d =& -\rho_c(1-\alpha_d)v_c\frac{dv_c}{dz} + \mu_c(1-\alpha_d)\frac{du_c}{dz} \\ &- \mu_c u_c\frac{d\alpha_d}{dz} - (1-\alpha_d)\rho_c g \end{aligned} \tag{3.80}$$

$$\alpha_d\frac{dv_d}{dz} + v_d\frac{d\alpha_d}{dz} = 0 \tag{3.81}$$

$$(1-\alpha_d)\frac{dv_c}{dz} - v_c\frac{d\alpha_d}{dz} = 0 \tag{3.82}$$

$$\frac{dv_d}{dz} - u_d = 0 \tag{3.83}$$

$$\frac{dv_c}{dz} - u_c = 0 \tag{3.84}$$

where, in the particular case of the 1D problem, $\mathbf{f}^{\mathrm{T}} = (v_d, p, \alpha_d, v_c, u_d, u_c)$ represents the vector of unknowns. In order to alleviate the negative impacts of the strong interfacial force terms and acquire good convergence, Eqs.(3.79) and (3.80) have been scaled by K_d on both sides of the equations. The one dimensional system (3.79)-(3.84), consists of six equations and six unknowns. The linear cross-sectional averaged two-fluid model operator and its right-hand-side read:

$$\mathscr{L}\mathbf{f} = \mathbf{g}$$

$$\Longleftrightarrow \begin{bmatrix} 1 & \frac{\alpha_d^*}{K_d^*}\frac{d}{dz} & 0 & -1 & 0 & 0 \\ -1 & \frac{1-\alpha_d^*}{K_d^*}\frac{d}{dz} & 0 & 1 & 0 & 0 \\ \alpha_d^*\frac{d}{dz} & 0 & v_d^*\frac{d}{dz} & 0 & 0 & 0 \\ 0 & 0 & -v_c^*\frac{d}{dz} & (1-\alpha_d^*)\frac{d}{dz} & 0 & 0 \\ \frac{d}{dz} & 0 & 0 & 0 & -1 & 0 \\ 0 & 0 & 0 & \frac{d}{dz} & 0 & -1 \end{bmatrix} \begin{bmatrix} v_d \\ p \\ \alpha_d \\ v_c \\ u_d \\ u_c \end{bmatrix} = \begin{bmatrix} g_1^* \\ g_2^* \\ 0 \\ 0 \\ 0 \\ 0 \end{bmatrix} \text{ in } \Omega \tag{3.85}$$

in which,

$$g_1^* = \frac{1}{K_d^*}\left[-\alpha_d^*\rho_d g - \rho_d\alpha_d^* v_d^*\frac{dv_d^*}{dz} + \mu_d u_d^*\frac{d\alpha_d^*}{dz} + \mu_d\alpha_d^*\frac{du_d^*}{dz}\right] \tag{3.86}$$

$$g_2^* = \frac{1}{K_d^*}\left[-(1-\alpha_d^*)\rho_c g - \mu_c u_c^*\frac{d\alpha_d^*}{dz} + \rho_c(1-\alpha_d^*)v_c^*\frac{dv_c^*}{dz} + \mu_c(1-\alpha_d^*)\frac{du_c^*}{dz}\right] \tag{3.87}$$

where variables with a superscript asterisk denote values from previous iteration. The system of equations can be written in a standard form according to 2.3

$$\mathscr{L}\mathbf{f} = \mathbf{L}_z\frac{\partial\mathbf{f}}{\partial z} + \mathbf{L}_0 = \mathbf{g} \tag{3.88}$$

in which, $\mathbf{L}_z$, $\mathbf{L}_0$ and $\mathbf{g}$ are coefficient matrices.

$$\mathbf{L}_z = \begin{bmatrix} 0 & \frac{\alpha_d^*}{K_d^*} & 0 & 0 & 0 & 0 \\ 0 & \frac{1-\alpha_d^*}{K_d^*} & 0 & 0 & 0 & 0 \\ \alpha_d^* & 0 & v_d^* & 0 & 0 & 0 \\ 0 & 0 & -v_c^* & (1-\alpha_d^*) & 0 & 0 \\ 1 & 0 & 0 & 0 & 0 & 0 \\ 0 & 0 & 0 & 1 & 0 & 0 \end{bmatrix} \tag{3.89}$$

$$\mathbf{L}_0 = \begin{bmatrix} 1 & 0 & 0 & -1 & 0 & 0 \\ -1 & 0 & 0 & 1 & 0 & 0 \\ 0 & 0 & 0 & 0 & 0 & 0 \\ 0 & 0 & 0 & 0 & 0 & 0 \\ 0 & 0 & 0 & 0 & -1 & 0 \\ 0 & 0 & 0 & 0 & 0 & -1 \end{bmatrix} \tag{3.90}$$

$$\mathbf{g} = \begin{bmatrix} \frac{1}{K_d^*}\left[-\alpha_d^*\rho_d g - \rho_d\alpha_d^* v_d^*\frac{dv_d^*}{dz} + \mu_d u_d^*\frac{d\alpha_d^*}{dz} + \mu_d\alpha_d^*\frac{du_d^*}{dz}\right] \\ \frac{1}{K_d^*}\left[-(1-\alpha_d^*)\rho_c g - \mu_c u_c^*\frac{d\alpha_d^*}{dz} + \rho_c(1-\alpha_d^*)v_c^*\frac{dv_c^*}{dz} + \mu_c(1-\alpha_d^*)\frac{du_c^*}{dz}\right] \\ 0 \\ 0 \\ 0 \\ 0 \end{bmatrix} \tag{3.91}$$

The domain has been discretized with a mesh of non-overlapping spectral elements. Each spectral element Ω_e is mapped on the reference spectral element $[-1,\ 1]$ by using an iso-parametric mapping with local coordinate z. In the spectral element all variables located at the Gauss-Legendre-Lobatto collocation points, can be approximated by the same Lagrangian interpolant. For the 1D cross-sectional averaged two-fluid problem, the discrete spectral element approximation yields

$$\mathbf{f}_e = \sum_{r=1}^{N+1} \phi_r(z) \begin{bmatrix} v_d \\ p \\ \alpha_d \\ v_c \\ u_d \\ u_c \end{bmatrix}_r \tag{3.92}$$

where $\phi_r(z)$ with $1 \leq r \leq N+1$ represents the Lagrangian interpolants in the z-direction through the GLL points. The vector $[v_d, p, \alpha_d, v_c, u_d, u_c]^{\mathrm{T}}$ is the vector of unknown coefficients, evaluated at the GLL-collocation point. The local element matrices

$$\mathbf{A}_e = \int_{\Omega_e} [\mathscr{L}\phi_1, \cdots, \mathscr{L}\phi_{N+1}]^{\mathrm{T}} [\mathscr{L}\phi_1, \cdots, \mathscr{L}\phi_{N+1}]\, d\Omega_e \tag{3.93}$$

and the element right-hand-side

$$\mathbf{F}_e = \int_{\Omega_e} [\mathscr{L}\phi_1, \cdots, \mathscr{L}\phi_{N+1}]^{\mathrm{T}} \mathbf{g}\, d\Omega_e \tag{3.94}$$

yield the global assembled system of linear algebraic equations

$$\mathbf{AU} = \mathbf{F} \tag{3.95}$$

where $\mathbf{U}$ represents the global vector of unknowns nodal values. The two-fluid problem operator $\mathscr{L}$ and its right-hand-side $\mathbf{g}$ are given in (3.85)-(3.87). Note that, since the matrix $\mathbf{A}$ is symmetric positive definite, robust conjugate gradient iterative methods can be employed.

The LSSEM provides a powerful technique for numerical solution to the multi-fluid model. Compared to the finite volume method, the use of least-squares spectral element method leads to higher order convergence with h-refinement and even exponential convergence with p-enrichment if the underlying exact solution is sufficiently smooth.

Rather than using iterative schemes such as SIMPLE or IPSA to deal with the velocity-pressure coupling, Eq.(3.80) in the two-fluid model equations is directly being used for solving the pressure, and no extra equation for the pressure correction is needed.

In the FVM, the hyperbolic equations generally require a different treatment such as upwinding or artificial diffusion, the least-squares approach has a unified formulation for the numerical solution of all types of partial differential equations. Jiang [46, page 29] has compared analytically the error and stability estimates of the classic Galerkin method, the Streamline Upwinding Petrov-Galerkin method (SUPG) and the LSM for solving the advective (hyperbolic) equation. He concluded that both the classic Galerkin and the SUPG has different controls on variable and its derivative, leading to different convergences. However, the LSM has same order of controls on both the variable and its derivative, and their convergences are equally optimal.

In the LSM, special treatments, such as upwinding, artificial dissipation, staggered grid or non-equal-order elements, operator-splitting, etc. are unnecessary [46].

When the LSM is used to handle non-linear multiphase problem, the convergence criteria can be set in such way that difference of solution from last two iterative steps is smaller than a pre-specified value,

$$\left|\mathbf{f}^{**} - \mathbf{f}^{*}\right| \leq \varepsilon. \tag{3.96}$$

Alternatively, the LSM can use residue instead to formulate the convergence criteria,

$$\left\|\mathscr{L}\mathbf{f}^{*} - \mathbf{g}\right\|_{L^2} \leq \varepsilon. \tag{3.97}$$

According to the norm-equivalent theory, minimizing the residue in the mapped function space leads to the minimization of the error in the original defined space.

Chapter 4

The Population Balance Equation

In bubble columns the flow regime turns into heterogeneous as the gas superficial velocity increases, and bubble-bubble, bubble-liquid interactions invoke complex bubble breakage and coalescence phenomena. These breakage and aggregation processes can produce bubbles (particles) with wide size distributions which might influence the hydrodynamic properties in very different ways, leading to variations in the interfacial mass and heat transfer fluxes. The population balance is a powerful tool to model such processes taking place in bubble columns.

4.1 The framework of the population balance

4.1.1 The number density function

Considering that general systems consists of particles dispersed in an environmental phase, which we shall refer to as the continuous phase. The particles may interact between themselves as well as with the continuous phase [79].

The particle population may be regarded as being randomly distributed in the particle state space, which includes both the physical space of *external* coordinates and the space of *internal* coordinates. The external coordinates $\mathbf{r} = (r_1, r_2, r_3)$ are used to denote the position vector of the particle, and the internal coordinates $\mathbf{x} = (x_1, x_2, \cdots, x_d)$ represent d different properties associated with the particle. We let the symbol $\Omega_{\mathbf{x}}$ represent the domain of internal coordinates, and $\Omega_{\mathbf{r}}$ be the domain of external coordinates. These domains may be bounded or may have infinite boundaries. We can define the averaged number density function $f(\mathbf{x}, \mathbf{r}, t)$ such that $f(\mathbf{x}, \mathbf{r}, t)dV_{\mathbf{x}}dV_{\mathbf{r}}$ is the average number of particles in the infinitesimal volume $dV_{\mathbf{x}}dV_{\mathbf{r}}$ around the particle state $(\mathbf{x}, \mathbf{r})$.

The number density function $f(\mathbf{x}, \mathbf{r}, t)$ is assumed to have sufficiently high regularity to allow differentiation with respect to any of its arguments as many times as necessary.

4.1.2 The Reynolds transport theorem

The rate of change of particle state may be described by the variations of the particle state vector in time over the particle state space of both internal and external coordinates. While the change of external coordinates refers to the motion through physical space, that of internal coordinates refers to the motion through an abstract property space.

A particle space continuum can be defined such that it contains both internal and external coordinates and it is deforming with the time in both coordinates. For a particle, the final state $(\mathbf{x}, \mathbf{r})$ will be reached after the particle goes through a time dependent pass from its original state $(\mathbf{x}_0, \mathbf{r}_0)$.

A Reynolds transport theorem can be derived for the particle space continuum. We assume that the particles are embedded on this continuum at every point such that the distribution of particles is described by the continuous density function $f(\mathbf{x}, \mathbf{r}, t)$. Let $\Psi(\mathbf{x}, \mathbf{r})$ be an *extensive* property [1] associated with a single particle located at $(\mathbf{x}, \mathbf{r})$. The Reynolds transport theorem in a domain of $\Omega(t) = \Omega_{\mathbf{x}}(t) \times \Omega_{\mathbf{r}}(t)$ in general vector spaces is given by:

$$\begin{aligned} &\frac{d}{dt} \int_{\Omega_{\mathbf{x}(t)}} \int_{\Omega_{\mathbf{r}(t)}} \Psi f \, dV_{\mathbf{x}} \, dV_{\mathbf{r}} \\ &= \int_{\Omega_{\mathbf{x}(t)}} \int_{\Omega_{\mathbf{r}(t)}} \left[\frac{\partial}{\partial t} \Psi f + \nabla_{\mathbf{x}} \cdot (\mathbf{v}_d \Psi f) + \nabla_{\mathbf{r}} \cdot (\mathbf{w}_d \Psi f) \right] dV_{\mathbf{x}} \, dV_{\mathbf{r}} \end{aligned} \tag{4.1}$$

where $\mathbf{v}_d$ and $\mathbf{w}_d$ are defined as "velocities" for internal coordinates and for external coordinates, respectively. $\nabla_{\mathbf{r}} \cdot$ represents the regular spatial divergence (for fixed internal coordinates) in any convenient spatial coordinate system, and $\nabla_{\mathbf{x}} \cdot$ represents the divergence in the internal coordinate while holding the external coordinates fixed.

If we assume the only way in which the number of particles in $\Omega(t)$ can change is by birth and death process, the general population balance equation for a system can be written as:

$$\frac{\partial}{\partial t} f + \nabla_{\mathbf{x}} \cdot \mathbf{v}_d f + \nabla_{\mathbf{r}} \cdot \mathbf{w}_d f = h, \tag{4.2}$$

in which $h(\mathbf{x}, \mathbf{r}, t)$ is the net birth rate per unit volume of particle state space. It is dependent on the models of breakage and aggregation. The equation must be supplemented with initial and boundary conditions.

4.1.3 The breakage

The breakage process is assumed to be local and *instantaneous*, which implies a time scale small compared with that in which the particles state varies or with the time scale used for observing the population.

[1] Contrary to the *intensive* property, which does **not** depend on the amount of the substance in a system, the *extensive* property depends on amount of particles in the system. For instance, mass and energy are the *extensive* properties.

The breakup of particles is assumed to occur independently of each other. Let $b(\mathbf{x}, \mathbf{r}, \mathbf{Y}, t)$ be the specific "breakage rate" of particles of state $(\mathbf{x}, \mathbf{r})$ at time t in an environment described by $\mathbf{Y}$. $\mathbf{Y}$ can be hydrodynamic parameters, dissipation rate, temperature, etc. The breakage rate represents the fraction of particles of state $(\mathbf{x}, \mathbf{r})$ breaking *per unit time*. Then we have

$$\mathcal{B}^{-}(\mathbf{x}, \mathbf{r}, \mathbf{Y}, t) = b(\mathbf{x}, \mathbf{r}, \mathbf{Y}, t) f(\mathbf{x}, \mathbf{r}, t) \tag{4.3}$$

the average number of particles of state $(\mathbf{x}, \mathbf{r})$ "lost" by breakage per unit time.

The breakage functions include the breakage rate $b(\mathbf{x}, \mathbf{r}, \mathbf{Y}, t)$, the multiplicity factor $\nu(\mathbf{x}', \mathbf{r}', \mathbf{Y}, t)$ and the probability density function $P(\mathbf{x}, \mathbf{r}|\mathbf{x}', \mathbf{r}', \mathbf{Y}, t)$.

The function $b(\mathbf{x}, \mathbf{r}, \mathbf{Y}, t)$ has the dimensions of reciprocal time and is often called the breakage frequency.

The breakage rate can be modeled based on several interpretations, for instance

$$b(\mathbf{x}, \mathbf{r}, t) \propto \bar{\mathbf{v}} \Sigma_b \tag{4.4}$$

with $\bar{\mathbf{v}}$ the average velocity of the particles and Σ_b the macroscopic breakage cross section. This macroscopic cross section is the inverse of the mean free path related to the breakage. Thus, the macroscopic cross section is a measure of the distance traveled by the particle before it breaks. The macroscopic cross section can be expressed as $\Sigma = N\sigma$ with σ the microscopic cross section and N the number of breakage points in the system. The microscopic cross section can be defined as the cross sectional area of the particle. A breakage point can be considered as a singularity in the system for which the breakage originates, for instance turbulent fluctuations. This type of formulation was widely used for modeling the breakage rate.

A different alternative is to consider that

$$b(\mathbf{x}, \mathbf{r}, t) \propto \frac{1}{\tau} \tag{4.5}$$

where τ is the characteristic life time of a particle in the system before breaking.

The multiplicity factor $\nu(\mathbf{x}', \mathbf{r}', \mathbf{Y}, t)$ is the average number of particles formed from the breakup of a single particle of state $(\mathbf{x}', \mathbf{r}')$ in an environment of state $\mathbf{Y}$ at time t. It has a minimum value of 2 but, being an average number, is not restricted to being an integer.

The probability density function $P(\mathbf{x}, \mathbf{r}|\mathbf{x}', \mathbf{r}', \mathbf{Y}, t)$ represents the probability of appearance for particles from the breakup of a particle of state $(\mathbf{x}', \mathbf{r}')$ in an environment of state $\mathbf{Y}$ at time t that have state $(\mathbf{x}, \mathbf{r})$. This is a continuously distributed fraction over particle state space. It satisfies the normalization condition

$$\int_{\Omega_{\mathbf{x}}} P(\mathbf{x}, \mathbf{r}|\mathbf{x}', \mathbf{r}', \mathbf{Y}, t)\, dV_{\mathbf{x}} = 1 \tag{4.6}$$

If there's no loss of mass during the breakage, then

$$m(\mathbf{x}') = \nu(\mathbf{x}', \mathbf{r}', \mathbf{Y}, t) \int_{\Omega_\mathbf{x}} m(\mathbf{x}) P(\mathbf{x}, \mathbf{r} | \mathbf{x}', \mathbf{r}', \mathbf{Y}, t) f(\mathbf{x}', \mathbf{r}', t)\, dV_\mathbf{x} \tag{4.7}$$

in which $m(\mathbf{x})$ is the mass of the particle of state $\mathbf{x}$.

Assuming that the breakage is binary we have $\nu = 2$. The volume-based probability density function $\tilde{P}(V, \mathbf{r} | V', \mathbf{r}', \mathbf{Y}, t)$ with V' the volume of the particle that breaks, and V the volume of one particle that was produced, can be related to the so-called breakage redistribution function $\tilde{h}(V, \mathbf{r} | V', \mathbf{r}', \mathbf{Y}, t)$ that gives the relation between the number of the particles of a state $(V, \mathbf{r})$ that appear due to the breakup of a particle of state $(V', \mathbf{r}')$ in an environment of state $\mathbf{Y}$ at time t. The redistribution function can be written as

$$\tilde{h}(V, \mathbf{r} | V', \mathbf{r}', \mathbf{Y}, t) = \nu \tilde{P}(V, \mathbf{r} | V', \mathbf{r}', \mathbf{Y}, t) \tag{4.8}$$

The $\tilde{P}(V, \mathbf{r} | V', \mathbf{r}', \mathbf{Y}, t)$ must satisfy the symmetry condition

$$\tilde{P}(V' - V, \mathbf{r} | V', \mathbf{r}', \mathbf{Y}, t) = \tilde{P}(V, \mathbf{r} | V', \mathbf{r}', \mathbf{Y}, t) \tag{4.9}$$

because a fragment of volume V formed from a parent of volume V' (undergoing binary breakage) automatically implies that the other has volume $V' - V$ so that their probabilities must be the same.

Then, the birth rate of the particles due to the breakage is

$$\mathcal{B}^+(\mathbf{x}, \mathbf{r}, \mathbf{Y}, t) = \int_{\Omega_\mathbf{r}} \int_{\Omega_\mathbf{x}} \nu(\mathbf{x}', \mathbf{r}', \mathbf{Y}, t) b(\mathbf{x}', \mathbf{r}', \mathbf{Y}, t) P(\mathbf{x}, \mathbf{r} | \mathbf{x}', \mathbf{r}', \mathbf{Y}, t) f(\mathbf{x}', \mathbf{r}', t)\, dV_\mathbf{x}\, dV_\mathbf{r} \tag{4.10}$$

which reflects the production of particles of state $(\mathbf{x}, \mathbf{r})$ by breakage of particles of all particle states, internal and external.

The net birth rate of particles of state is given by $\mathcal{B}(\mathbf{x}, \mathbf{r}, \mathbf{Y}, t) \equiv \mathcal{B}^+(\mathbf{x}, \mathbf{r}, \mathbf{Y}, t) - \mathcal{B}^-(\mathbf{x}, \mathbf{r}, \mathbf{Y}, t)$. The right-hand side of which is given by Eqs.(4.3) and (4.10).

4.1.4 The aggregation

Aggregation occurs between at least two particles. The binary aggregation is a special significance although in crowded systems, it is conceivable that several adjacent particles could simultaneously aggregate. Aggregation can be referred as *coalescence*, in which two particles completely merge along with their interiors, or to *coagulation*, which features a "flow" of particles loosely held by surface forces without involving physical contact. The aggregation frequency is defined as the probability that a particle of state $(\mathbf{x}, \mathbf{r})$

and another particle of state $(\mathbf{x}', \mathbf{r}')$, both present at time t in a continuous phase with state locally at $\mathbf{Y}$, will aggregate in the time interval t to $t + dt$, as given by:

$$a(\mathbf{x}, \mathbf{r}; \mathbf{x}', \mathbf{r}', \mathbf{Y}, t)dt \tag{4.11}$$

It represents the fraction of particle pairs of specified states aggregating per unit time. The aggregating frequency satisfies the *symmetry* property

$$a(\mathbf{x}, \mathbf{r}; \mathbf{x}', \mathbf{r}', \mathbf{Y}, t)dt = a(\mathbf{x}', \mathbf{r}'; \mathbf{x}, \mathbf{r}, \mathbf{Y}, t)dt \tag{4.12}$$

The explicit time dependence in the aggregation frequency is generally not a desirable feature in models and is eliminated in the remaining treatment.

We define $f_2(\mathbf{x}, \mathbf{r}, \mathbf{x}', \mathbf{r}', t)$ to represent the average number of distinct pairs of particles at time t per unit volumes in state space located about $(\mathbf{x}, \mathbf{r})$ and $(\mathbf{x}', \mathbf{r}')$, respectively.

In gas-liquid bubbly flows, the aggregation is often referred as coalescence. The coalescence rate determines the fraction of particles that coalesce per unit time. A simple modeling approach consists in considering the coalescence process as a two stage process. This consists in determining the collision rate, C_{rate}, between the particles of states $(\mathbf{x}, \mathbf{r})$ and $(\mathbf{x}', \mathbf{r}')$, and the coalescence efficiency, C_{eff}, which reflects the ratio of the number of particles that coalesce and the number of particle collisions.

$$a(\mathbf{x}, \mathbf{r}, \mathbf{x}', \mathbf{r}', \mathbf{Y}) = C_{rate}(\mathbf{x}, \mathbf{r}, \mathbf{x}', \mathbf{r}', \mathbf{Y})C_{eff}(\mathbf{x}, \mathbf{r}, \mathbf{x}', \mathbf{r}', \mathbf{Y}) \tag{4.13}$$

The coalescence efficiency gives a measure of the efficiency of the coalescence process. Normally, the coalescence efficiency is related to the drainage time of the liquid between particles and the time of the collision. Nevertheless, this approach ends up in rather empirical expressions due to the complexity of the process.

A common approximation of the pair density function f_2 is made by

$$f_2(\mathbf{x}', \mathbf{r}'; \mathbf{x}, \mathbf{r}, t) = f(\mathbf{x}', \mathbf{r}', t)f(\mathbf{x}, \mathbf{r}, t) \tag{4.14}$$

this implies that there is no statistical correction between particles of state $(\mathbf{x}', \mathbf{r}')$ and $(\mathbf{x}, \mathbf{r})$ at any instant t.

Eq.(4.14) is a good approximation under the hypothesis of dilute systems and particle chaos. Typical multiphase flow regimes violate the required hypotheses and so expression (4.14) should be considered incorrect. The hypothesis of dilute systems requires that the fraction of volume occupied by the particles is small. This requirement for example is justified considering aerosol dispersions. However, industrial applications can demand void fractions up to 50%, which is far from satisfying the condition of a dilute system.

The second hypothesis of particle chaos requires that the particles at different positions are uncorrelated. This hypothesis can be violated in multiphase flows due to the effects caused by the motion of a particle into the neighboring ones. A possible way of considering the deviation from the hypothesis of dilution is to assume

$$f_2(\mathbf{x}', \mathbf{r}'; \mathbf{x}, \mathbf{r}, t) = Yf(\mathbf{x}', \mathbf{r}', t)f(\mathbf{x}, \mathbf{r}, t) \tag{4.15}$$

with Y the pair correlation function which considers, for example, the fact that particles actually occupy a finite volume and particle screening which reduce the possible particle interaction. A simple model for the pair correlation function consists in assuming that the effective volume where the particle can move is given by α, with α the void fraction, then the pair correlation function can be defined as

$$Y = \frac{1}{1-\alpha}. \tag{4.16}$$

implying that the interactions are increased due to the reduction of the available volume. This correction factor was used by [30] for simulating bubbly flows adopting the Enskog dense gas model.

The source term for the rate of production of particles in volume $(\mathbf{x}, \mathbf{r})$ of state $(\mathbf{x}, \mathbf{r})$ may be written as

$$\mathcal{A}^{+}(\mathbf{x}, \mathbf{r}, \mathbf{Y}, t) = \int_{\Omega_{\mathbf{x}}} \int_{\Omega_{\mathbf{r}}} \frac{1}{\delta} a(\tilde{\mathbf{x}}, \tilde{\mathbf{r}}; \mathbf{x}', \mathbf{r}', \mathbf{Y}) f_2(\tilde{\mathbf{x}}, \tilde{\mathbf{r}}; \mathbf{x}', \mathbf{r}', t) \frac{\partial(\tilde{\mathbf{x}}, \tilde{\mathbf{r}})}{\partial(\mathbf{x}, \mathbf{r})} \, dV_{\mathbf{x}'} \, dV_{\mathbf{r}'} \tag{4.17}$$

in which the density with respect to coordinates $(\mathbf{x}', \mathbf{r}')$ has been transformed into one in terms of $(\mathbf{x}, \mathbf{r})$ by using the appropriate Jacobian. $(\mathbf{x}', \mathbf{r}')$ is held constant in the definition of the Jacobian. δ represents the number of times identical pairs have been considered in the interval of integration in the right-hand side of (4.17) so that $1/\delta$ corrects for the redundancy. The sink term $\mathcal{A}^{-}(\mathbf{x}, \mathbf{r}, \mathbf{Y}, t)$ is found to be

$$\mathcal{A}^{-}(\mathbf{x}, \mathbf{r}, \mathbf{Y}, t) = \int_{\Omega_{\mathbf{x}}} \int_{\Omega_{\mathbf{r}}} a(\mathbf{x}', \mathbf{r}'; \mathbf{x}, \mathbf{r}, \mathbf{Y}) f_2(\mathbf{x}', \mathbf{r}'; \mathbf{x}, \mathbf{r}, t) \, dV_{\mathbf{x}'} \, dV_{\mathbf{r}'} \tag{4.18}$$

The net birth rate of particles of state is given by $\mathcal{A}(\mathbf{x}, \mathbf{r}, \mathbf{Y}, t) \equiv \mathcal{A}^{+}(\mathbf{x}, \mathbf{r}, \mathbf{Y}, t) - \mathcal{A}^{-}(\mathbf{x}, \mathbf{r}, \mathbf{Y}, t)$. The right-hand side of which is given by Eqs.(4.18) and (4.17).

4.2 The population balance equation (PBE)

Since the birth and death functions are now identified the complete population balance equation, a breakage/aggregation population is given by substituting the right-hand side of (4.2) with expressions of breakage and aggregation terms as calculated from (4.3), (4.10), (4.17) and (4.18). Since particles distributed according to their volume are frequently encountered in applications, assuming that particle coalesce or breakup does not have impact on the coalescence or breakage of particles somewhere else, which implies that the breakage frequency, the probability density function and the aggregation frequency are independent of the external coordinates $\mathbf{r}$. In addition, the integrals over the external coordinates in the breakage birth term (4.10), the aggregation birth term (4.17) and the aggregation death term (4.18) disappear. We can consider the breakage and aggregation processes for a population of particle distributed according to their volume denoted by V.

A volume-based PBE that includes breakup, aggregation and source terms can be written as follows:

$$\frac{\partial \tilde{f}(V,\mathbf{r},t)}{\partial t} + \nabla_{\mathbf{r}} \cdot (\mathbf{v}_d \tilde{f}(V,\mathbf{r},t)) = \tilde{\mathcal{B}}^{+}(V,\mathbf{r},t) - \tilde{\mathcal{B}}^{-}(V,\mathbf{r},t) + \tilde{\mathcal{A}}^{+}(V,\mathbf{r},t) - \tilde{\mathcal{A}}^{-}(V,\mathbf{r},t) \tag{4.19}$$

in which,

$$\tilde{\mathcal{B}}^{+}(V,\mathbf{r},t) = \int_{V}^{V_{max}} \nu \tilde{P}(V,V') \tilde{b}(V') \tilde{f}(V',\mathbf{r},t) dV' \tag{4.20}$$

$$\tilde{\mathcal{B}}^{-}(V,\mathbf{r},t) = \tilde{b}(V) \tilde{f}(V,\mathbf{r},t) \tag{4.21}$$

$$\tilde{\mathcal{A}}^{+}(V,\mathbf{r},t) = \frac{1}{2} \int_{V_{min}}^{V} \tilde{a}(V-V',V') \tilde{f}(V',\mathbf{r},t) \tilde{f}(V-V',\mathbf{r},t) dV' \tag{4.22}$$

$$\tilde{\mathcal{A}}^{-}(V,\mathbf{r},t) = \tilde{f}(V,\mathbf{r},t) \int_{V_{min}}^{V_{max}-V} \tilde{a}(V,V') \tilde{f}(V',\mathbf{r},t) dV' \tag{4.23}$$

$\tilde{\mathcal{B}}^{-}$, $\tilde{\mathcal{B}}^{+}$, $\tilde{\mathcal{A}}^{-}$ and $\tilde{\mathcal{A}}^{+}$ have the following meaning:

1. rate of death of particles of mass V due to breakup,
2. rate of birth of particles of mass V due to breakup of larger particles,
3. rate of death of particles of mass V due to aggregation with other particles,
4. rate of birth of particles of mass V due to aggregation of smaller particles.

in which, $\tilde{b}(V)$ is the breakup frequency, $\tilde{P}(V,V')$ is the breakup kernel that represents the probability that a particle of mass V' splits up creating two particles of mass V and $V'-V$. The aggregation kernel $\tilde{a}(V,V')$ represents the probability of aggregation per unit time that two particles with mass $V-V'$ and V' to aggregate resulting in a particle with the mass V. V_{min} and V_{max} are the lower and upper limits of the particle size, respectively. In addition, the upper limit of the integral in the aggregation birth term (4.22) is $(V_{max}-V)$ (see [42, page 1324]).

The Eq.(4.19) can also be expressed in terms of the number density function using particle length as internal coordinate by assuming $V \propto \xi^3$ and observing the relation $\tilde{f}(V,\mathbf{r},t)\,dV = f(\xi,\mathbf{r},t)\,d\xi$, in which ξ is the equivalent particle length.

$$\frac{\partial f(\xi,\mathbf{r},t)}{\partial t} + \nabla_{\mathbf{r}} \cdot (\mathbf{v}_d f(\xi,\mathbf{r},t)) = \mathcal{B}^{+}(\xi,\mathbf{r},t) - \mathcal{B}^{-}(\xi,\mathbf{r},t) + \mathcal{A}^{+}(\xi,\mathbf{r},t) - \mathcal{A}^{-}(\xi,\mathbf{r},t) \tag{4.24}$$

in which,

$$\mathcal{B}^{+}(\xi,\mathbf{r},t)=\int_{\xi}^{\xi_{max}}\nu P(\xi,\zeta)b(\zeta)f(\zeta,\mathbf{r},t)d\zeta \tag{4.25}$$

$$\mathcal{B}^{-}(\xi,\mathbf{r},t)=b(\xi)f(\xi,\mathbf{r},t) \tag{4.26}$$

$$\mathcal{A}^{+}(\xi,\mathbf{r},t)=\frac{\xi^2}{2}\int_{\xi_{min}}^{\xi}\frac{a((\xi^3-\zeta^3)^{1/3},\zeta)}{(\xi^3-\zeta^3)^{2/3}}f(\zeta,\mathbf{r},t)f((\xi^3-\zeta^3)^{1/3},\mathbf{r},t)d\zeta \tag{4.27}$$

$$\mathcal{A}^{-}(\xi,\mathbf{r},t)=f(\xi,\mathbf{r},t)\int_{\xi_{min}}^{(\xi_{max}^3-\xi^3)^{1/3}}a(\xi,\zeta)f(\zeta,\mathbf{r},t)d\zeta \tag{4.28}$$

where ξ and ζ represent the particle diameter. The detail transformation from the mass-based PBE to the length-based PBE is explained in App. C.

The moments of the distribution function of different orders can be defined as:

$$m^{(k)}(\mathbf{r},t)=\int\xi^k f(\xi,\mathbf{r},t)d\xi \tag{4.29}$$

In this work, the moments which have physical significance are:

(i) the number density (number of particles per unit mass)

$$N(\mathbf{r},t)=\int f(\xi,\mathbf{r},t)d\xi \tag{4.30}$$

(ii) the gas void fraction (mass of particles per unit mass)

$$\alpha(\mathbf{r},t)=\int(\frac{\pi}{6}\xi^3)f(\xi,\mathbf{r},t)d\xi \tag{4.31}$$

and (iii) the Sauter diameter

$$\xi_{32}(\mathbf{r},t)=\frac{\int\xi^3 f(\xi,\mathbf{r},t)d\xi}{\int\xi^2 f(\xi,\mathbf{r},t)d\xi} \tag{4.32}$$

The mean particle volume can be computed by

$$\hat{V}_{b,mean}(\mathbf{r},t)=\frac{\alpha(\mathbf{r},t)}{N(\mathbf{r},t)}=\frac{\int(\frac{\pi}{6}\xi^3)f(\xi,\mathbf{r},t)d\xi}{\int f(\xi,\mathbf{r},t)d\xi} \tag{4.33}$$

The integrals in Eqs.(4.30), (4.31) and (4.32) should be evaluated over all possible particle lengths.

4.3 Numerical methods for solving the PBE

4.3.1 Method of classes (CM)

When methods of classes [39, 53, 91] based on M fixed size intervals in a partition $P_M \equiv \{0 = V_1, V_2, \cdots, V_M, V_{M+1} = \infty\}$ are used, the discretized form of Eq.(4.19) yields

$$\frac{\partial N_i}{\partial t} + \nabla \cdot \left(\mathbf{v}_d(\hat{V}_i) N_i\right) = \frac{1}{2} \sum_{j=1}^{i-1} N_j \sum_{(\hat{V}_j + \hat{V}_k) \in I_i} N_k \tilde{a}(\hat{V}_j, \hat{V}_k)$$
$$- N_i \sum_{j=1}^{M} N_j \tilde{a}(\hat{V}_i, \hat{V}_j) + \sum_{j=1}^{M} \nu(\hat{V}_j) N_j \tilde{b}(\hat{V}_j) \int_{V_i}^{V_{i+1}} \tilde{P}(V/\hat{V}_j)\, dV - \tilde{b}(\hat{V}_i) N_i$$
$$i = 1, \cdots, M. \tag{4.34}$$

in which, $\hat{V}_i \in [V_i, V_j)$ represents a pivot size. Here, the dependency of the variable on the spatial position and time has been omitted for simplicity of notation. By this method, the transport of the population balance equation corresponds to the transport of M scalars, i.e. the number density of the classes, N_i.

In the CM, good accuracy can be achieved if a large number of size groups are used, but at the expense of high CPU cost due to increased number of scalars to be solved. The number of classes is a potential problem in CFD applications, especially when a multi-fluid flow model needs to be used; hence the CM method is not a feasible approach in practice.

4.3.2 Quadrature method of moments (QMOM)

In the method of moments (MOM), the particle size distribution (PSD) is not tracked directly but through its moments integrated over the internal coordinates. This approach has many advantages such as low CPU time and relatively high accuracy. The standard method of moment (SMM) needs to be closed, which limits its practical application.

In the QMOM [66, 67, 68], the Gaussian quadrature approximation for PSD is introduced to close the SMM. By the QMOM, the solution of Eq.(4.19) reduces to transport the lower order moments of the particle size distribution function, m^k, as follows

$$\frac{\partial m^{(k)}}{\partial t} + \nabla \cdot \left(\mathbf{v}_d^{(k)} m^{(k)}\right) = H^{(k)}(\hat{V}_i, N_i)$$
$$k = 0, \cdots, 2M-1; \quad i = 1, \cdots, M. \tag{4.35}$$

Here, M is the number of classes used for the quadrature approximation. The terms of the

quadrature, $\hat{V}_i$, and N_i, are derived by the inversion of the following non-linear system

$$m^{(k)} = \sum_{i=1}^{M} N_i \hat{V}_i^k \qquad k = 0, \cdots, 2M-1. \tag{4.36}$$

The k^{th} moment velocity, $\mathbf{v}_d^{(k)}$, is defined as

$$\mathbf{v}_d^{(k)} = \frac{\sum_{i=1}^{M} \mathbf{v}_d(\hat{V}_i) N_i \hat{V}_i^k}{\sum_{i=1}^{M} N_i \hat{V}_i^k} \qquad k = 0, \cdots, 2M-1 \tag{4.37}$$

QMOM has been widely used for PBE in recent years [28, 55, 66, 67, 82, 93, 94, 100], and has been extended to bivariate PBE applications [95, 98, 99]

The QMOM uses the product-difference (PD) introduced by Gordon [34] to evaluating the Gaussian quadrature. However, the PD algorithm is a numerical ill-conditioned method for computing the Gauss quadrature rule (e.g. [58]). In general the computation of the quadrature rule based on the power moments of the density function is quite sensitive to small errors as the number of moments used becomes large (e.g. [32, 33]). The applicability of QMOM is limited to no more than 12 moments, although in certain applications it is stated that few moments are enough for obtaining reliable results [69].

It has also been reported that with the QMOM it is difficult to handle systems where there is a strong dependence of the dispersed-phase velocity on internal coordinates (e.g. fluidized bed and bubble column), and can become quite complex in the case of bivariate PBE [65].

4.3.3 Direct quadrature method of moments (DQMOM)

By the DQMOM [28, 65], after mathematical manipulation, Eq.(4.19) yields

$$\frac{\partial N_i}{\partial t} + \nabla \cdot \left(\mathbf{v}_d(\hat{V}_i) N_i \right) = a_i \qquad i = 1, \cdots, M \tag{4.38}$$

and

$$\frac{\partial \zeta_i}{\partial t} + \nabla \cdot \left(\mathbf{v}_d(\hat{V}_i) \zeta_i \right) = b_i \qquad i = 1, \cdots, M. \tag{4.39}$$

Here, the source terms are derived by the solution of the following linear system in the unknown a_i and b_i

$$\sum_{i=1}^{M} \left[\left(\hat{V}_i^k - k\hat{V}_i^k \right) a_i + k\hat{V}_i^{k-1} b_i \right] = H^{(k)} \qquad k = 0, \cdots, 2M-1. \tag{4.40}$$

The DQMOM defines a set of transport equations for the evolution of the quadrature rule. The DQMOM remains ill conditioned so it is necessary to keep the number of moments

small [23]. In particular, the DQMOM requires some ad hoc techniques for restarting the problem when singularities occurs. Basically, in the DQMOM the condition number of the system is monitored. When the condition number is too high, i.e. the problem become singular, small perturbations are added to the quadrature rule which can reduce the condition number and thus remove the singularity.

Previous studies have shown that the accuracy and time consumption of QMOM and DQMOM depend largely on the relative magnitude of the moments. The matrix becomes extremely difficult to solve if the moments vary over a large range. In such cases, the solution of the differential equations and the PD algorithms in QMOM, or the matrix inversion in DQMOM, would require excessive computational resources.

4.3.4 The least-squares method

In this section we are describing how to use the LSSEM to solve a space-time-property PBE with particle breakage and aggregation. The linear population balance operator and its right-hand-side read:

$$\begin{aligned}\mathscr{L}f = & \underbrace{\frac{\partial f(\xi,r,t)}{\partial t}}_{\text{transient term}} + \underbrace{\frac{\partial}{\partial r}(\mathbf{v}_d f(\xi,r,t))}_{\text{convection}} \\ & + \underbrace{b(\xi)f(\xi,r,t)}_{\text{breakage death}} - \underbrace{\int_{\xi}^{\xi_{max}} \nu P(\xi,\zeta)b(\zeta)f(\zeta,r,t)d\zeta}_{\text{breakage birth}} \\ & + \underbrace{f(\xi,r,t)\int_{\xi_{min}}^{(\xi^3_{max}-\xi^3)^{1/3}} a(\xi,\zeta)f^*(\zeta,r,t)d\zeta}_{\text{aggregation death}} \\ & - \underbrace{\frac{\xi^2}{2}\int_{\xi_{min}}^{\xi} \frac{a((\xi^3-\zeta^3)^{1/3},\zeta)}{(\xi^3-\zeta^3)^{2/3}} f^*(\zeta,r,t)f((\xi^3-\zeta^3)^{1/3},r,t)d\zeta}_{\text{aggregation birth}} \end{aligned} \tag{4.41}$$

and

$$g = 0 \tag{4.42}$$

where, in the particular case of the 1D problem, $f(\xi,r,t)$ represents the unknown number density functions. A superscript asterisk denote values from previous iteration.

The domain has been discretized with a mesh of non-overlapping spectral elements. Each spectral element Ω_e is mapped on the reference spectral element $[-1,\ 1]$ by using an iso-parametric mapping with local coordinate z. In the spectral element all variables located at the GL-GLL-GLL collocation points, can be approximated by the Lagrangian

interpolant. By GL-GLL-GLL we mean that we use the Gauss-Legendre points for the internal coordinate ξ, and use the Gauss-Legendre-Lobatto points for both external coordinate z and time t. For the transient 1D population balance equation, the discrete spectral element approximation yields

$$f_e = \sum_{j_\xi=1}^{N_\xi+1} \sum_{j_r=1}^{N_r+1} \sum_{j_t=1}^{N_t+1} f_{j_\xi,j_r,j_t}\ \phi_{j_\xi}(\xi)\phi_{j_r}(r)\phi_{j_t}(t) = \sum_{j=1}^{N^t} f_j\, \Phi_j(\mathbf{x}) \tag{4.43}$$

where $\phi_{j_\xi}(\xi)$ with $1 \leq j_\xi \leq N_\xi + 1$, $\phi_{j_r}(r)$ with $1 \leq j_r \leq N_r + 1$ and $\phi_{j_t}(t)$ with $1 \leq j_t \leq N_t + 1$ represent the Lagrangian interpolants in the ξ, r and t-direction through the GLL points, respectively. The global basis function

$$\Phi_j(\mathbf{x}) = \phi_{j_\xi}(\xi)\phi_{j_r}(r)\phi_{j_t}(t) \tag{4.44}$$

is the function of vector of independent variables $\mathbf{x} = [\xi, r, t]$ and the total degrees of freedom is defined as $N^t = (N_\xi + 1)(N_r + 1)(N_t + 1)$. The local element matrices

$$\begin{aligned}\mathbf{A}_e &= \int_{\Omega_e} [\mathscr{L}\Phi_1, \cdots, \mathscr{L}\Phi_{N^t}]^{\mathrm{T}} [\mathscr{L}\Phi_1, \cdots, \mathscr{L}\Phi_{N^t}]\, d\Omega_e \\ &= \begin{bmatrix} \langle \mathscr{L}\Phi_1, \mathscr{L}\Phi_1 \rangle_{\Omega_e} & \langle \mathscr{L}\Phi_1, \mathscr{L}\Phi_2 \rangle_{\Omega_e} & \cdots & \langle \mathscr{L}\Phi_1, \mathscr{L}\Phi_{N^t} \rangle_{\Omega_e} \\ \langle \mathscr{L}\Phi_2, \mathscr{L}\Phi_1 \rangle_{\Omega_e} & \langle \mathscr{L}\Phi_2, \mathscr{L}\Phi_2 \rangle_{\Omega_e} & \cdots & \langle \mathscr{L}\Phi_2, \mathscr{L}\Phi_{N^t} \rangle_{\Omega_e} \\ \vdots & \vdots & \ddots & \vdots \\ \langle \mathscr{L}\Phi_{N^t}, \mathscr{L}\Phi_1 \rangle_{\Omega_e} & \langle \mathscr{L}\Phi_{N^t}, \mathscr{L}\Phi_2 \rangle_{\Omega_e} & \cdots & \langle \mathscr{L}\Phi_{N^t}, \mathscr{L}\Phi_{N^t} \rangle_{\Omega_e} \end{bmatrix} \end{aligned} \tag{4.45}$$

and the element right-hand-side

$$\mathbf{F}_e = \int_{\Omega_e} [\mathscr{L}\Phi_1, \cdots, \mathscr{L}\Phi_{N^t}]^{\mathrm{T}} \mathbf{g}\, d\Omega_e = \begin{bmatrix} \langle \mathscr{L}\Phi_1, g \rangle_{\Omega_e} \\ \langle \mathscr{L}\Phi_2, g \rangle_{\Omega_e} \\ \vdots \\ \langle \mathscr{L}\Phi_{N^t}, g \rangle_{\Omega_e} \end{bmatrix} \tag{4.46}$$

The evaluations of the inner products in (4.45) and (4.46) can be numerical integrated by using the Gauss quadrature of order N^t or higher than N^t as being discussed in Chapter

2. At each Gauss quadrature point $\mathbf{x}_i = (\xi_{i_\xi}, r_{i_r}, t_{i_t}), \quad 1 \leq i \leq N^t$, we have

$$\mathscr{L}\Phi_j(\mathbf{x_i}) = \underbrace{\sum_{j_\xi=1}^{N_\xi+1}\sum_{j_r=1}^{N_r+1}\sum_{j_t=1}^{N_t+1}\phi_{j_\xi}(\xi_{i_\xi})\phi_{j_r}(r_{i_r})\phi'_{j_t}(t_{i_t})}_{\text{transient term}}$$

$$\underbrace{+v^*\big|_{\mathbf{x}_i}\phi_{j_\xi}(\xi_{i_\xi})\phi'_{j_r}(r_{i_r})\phi_{j_t}(t_{i_t}) + \frac{dv^*}{dr}\Big|_{\mathbf{x}_i}\phi_{j_\xi}(\xi_{i_\xi})\phi_{j_r}(r_{i_r})\phi_{j_t}(t_{i_t})}_{\text{convection}}$$

$$\underbrace{+b(\xi_{i_\xi})\phi_{j_\xi}(\xi_{i_\xi})\phi_{j_r}(r_{i_r})\phi_{j_t}(t_{i_t})}_{\text{breakage death}}$$

$$\underbrace{-\sum_{k=1}^{K+1} w_k(i_\xi)h(\xi_{i_\xi},\zeta_k(i_\xi))b(\zeta_k(i_\xi))\phi_{j_\xi}(\zeta_k(i_\xi))\phi_{j_r}(r_{i_r})\phi_{j_t}(t_{i_t})}_{\text{breakage birth}}$$

$$\underbrace{+\phi_{j_\xi}(\xi_{i_\xi})\phi_{j_r}(r_{i_r})\phi_{j_t}(t_{i_t})\sum_{k=1}^{K+1}\left[\begin{array}{l} w_k(i_\xi)a(\xi_{i_\xi},\zeta_k(i_\xi)) \\ \left(\begin{array}{l}\sum_{\tilde{j}_\xi=1}^{N_\xi+1}\sum_{\tilde{j}_r=1}^{N_r+1}\sum_{\tilde{j}_t=1}^{N_t+1} \\ \phi_{\tilde{j}_\xi}(\zeta_k(i_\xi))\phi_{\tilde{j}_r}(r_{i_r})\phi_{\tilde{j}_t}(t_{i_t})f^*_{\tilde{j}_\xi,\tilde{j}_r,\tilde{j}_t}\end{array}\right)\end{array}\right]}_{\text{aggregation death}}$$

$$\underbrace{-\frac{\xi_{i_\xi}^2}{2}\sum_{k=1}^{K+1}\left[\begin{array}{l} w_k(i_\xi)a((\xi_{i_\xi}^3-\zeta_k^3(i_\xi))^{1/3},\zeta_k(i_\xi))/(\xi_{i_\xi}^3-\zeta_k^3(i_\xi))^{2/3} \\ \left(\begin{array}{l}\sum_{\tilde{j}_\xi=1}^{N_\xi+1}\sum_{\tilde{j}_r=1}^{N_r+1}\sum_{\tilde{j}_t=1}^{N_t+1} \\ \phi_{\tilde{j}_\xi}(\zeta_k(i_\xi))\phi_{\tilde{j}_r}(r_{i_r})\phi_{\tilde{j}_t}(t_{i_t})f^*_{\tilde{j}_\xi,\tilde{j}_r,\tilde{j}_t}\end{array}\right) \\ \phi_{j_\xi}(\xi_{i_\xi}-\zeta_k(i\xi))\phi_{j_r}(r_{i_r})\phi_{j_t}(t_{i_t})\end{array}\right]}_{\text{aggregation birth}} \tag{4.47}$$

The local linear systems are obtained by substituting Eq.(4.47) into (4.45) and (4.46) at each subelement, and the global assembled system of linear algebraic equations yields

$$\mathbf{AU} = \mathbf{F} \tag{4.48}$$

where $\mathbf{U}$ represents the global vector of unknowns nodal values. The population balance equation problem operator $\mathscr{L}$ and its right-hand-side $\mathbf{g}$ are given in (4.41) and (4.42). Note that, since the matrix $\mathbf{A}$ is symmetric positive definite, robust conjugate gradient iterative methods can be employed.

Dorao et al. [22] compared error convergence rate and computation time of QMOM and LSQ for solving the PBE. LSM shows to be computational efficient and accurate for the tested problem. There is no limitation of the number of the required moments in the LSM. Besides, the LSM provides also information about the reliability of the solution in the residual, which can be used for controlling the time stepping in an efficient way.

4.3.5 The mass conservative least-squares method

Mass nonconservative breakage kernels

For the breakup processes, numerous source term closures have been formulated. Commonly used breakup closures in physical problems include the models proposed by Coulaloglou and Tavlarides [15], Diemer and Olson [20], Martinez-Bazan [59], Konno [50] etc. A shortcoming of the breakup kernels employed in many CFD models is that the conservation of volume/mass is not always fulfilled.

Models that do not conserve volume/mass generally lead to an evolution of the predicted volume fraction which is unstable and not meaningful from a physical point of view [100]. Inexact conservation of mass/volume has also been observed using the model presented in this work. The numerical verifications performed show that the system tends to lose mass when breakup takes place. We shall explain the mass conservation problem in the following.

If the dispersed phase density is assumed to be a constant, and there is no loss of mass during the breakage, then

$$\text{vol}(\zeta) = \nu \int_{\xi_{min}}^{\zeta} \text{vol}(\xi) P(\xi, \zeta)\, d\xi \tag{4.49}$$

in which, $\text{vol}(\xi) = (\pi/6)\xi^3$ is the volume of a spherical particle. For a binary breakage the multiplicity factor $\nu = 2$. Eq.(4.49) implies that the volumes of all the particles with the size interval $[\xi_{min}, \zeta)$ that are generated from breakage event of a parent particle of size ζ, should equal to the volume of this parent particle.

Figure 4.1 shows the performance of the Martinez-Bazan breakage kernel. A loss of volume/mass is observed and there's a significant reduction in the volume compared with that of the original parent particle as the dissipation rate increases. We can see that the loss of mass during the breakage event is due to the fact that the breakage kernel (daughter particle distribution function) does not fulfill the mass conservation constraint.

Using the theory of the constraint least-squares formulation introduced in section 2.5, we propose a mass conservative solution to the PBE. The mass conservative least-squares solution is based on the minimization of the least-squares functional

$$\mathcal{J}(f) = \frac{1}{2} \| \mathscr{L} f - g \|^2_{Y(\Omega)} \tag{4.50}$$

in which the operator $\mathscr{L}$ and source g are defined in Eq.(4.41) and (4.42), subjected to the constraint that mass is conserved

$$\nabla \cdot (\alpha \mathbf{v}_d) = 0 \tag{4.51}$$

in which, $\mathbf{v}_d$ is the dispersed phase velocity. Eq.(4.51) is obtained by integrating Eq.(4.50) over the entire internal coordinate domain, and using the definition of the void fraction (α) Eq.(4.31). Eq.(4.51) is also known as the continuity equation of the dispersed phase.

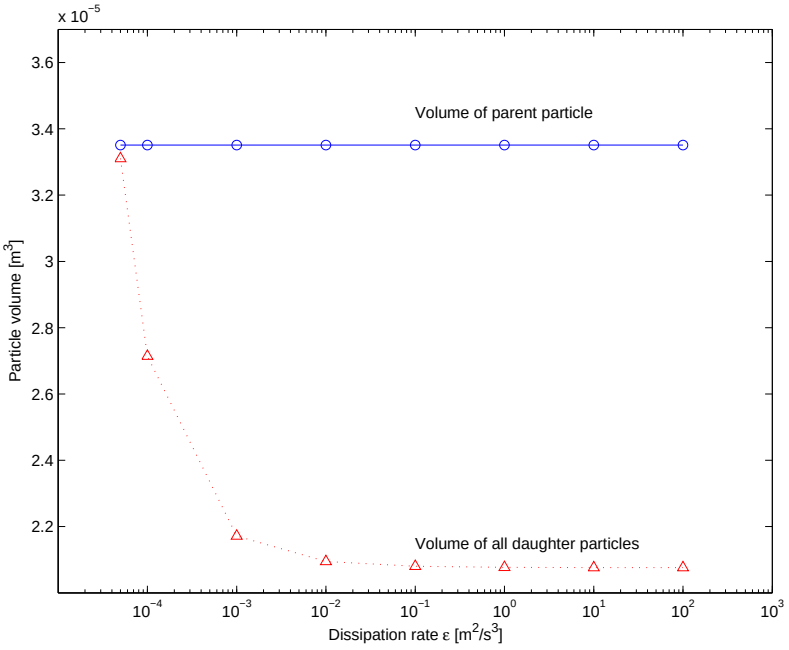

Figure 4.1: The loss of mass of a parent particle of size $\zeta = 0.02$ m during the breakage event when the Martinez-Bazan [59] breakage kernel is used (tested for the air-water flow with the dissipation rate ε varies from 5×10^{-5} to 100 $\mathrm{m}^2 \cdot \mathrm{s}^{-3}$).

The mass conservative formulation

Therefore the constrained minimization problem can be expressed in the form:

$$\min_{f \in Y} \mathcal{J}(f) \quad \text{subject to} \quad (4.51). \tag{4.52}$$

where the constraint equation (4.51) holds in function space S.

To enforce mass conservation, the Lagrange multiplier method is used. The constrained least-squares solution results from the equilibrium point of the following extended Lagrangian functional

$$\mathcal{I}(f, \lambda) = \mathcal{J}(f) + \int_{\Omega} \lambda \left[\nabla \cdot \left(\int_{\xi_{min}}^{\xi_{max}} f(\xi, \mathbf{z}) \mathrm{vol}(\xi)\, d\xi\, \mathbf{v}_d \right) \right] d\Omega \tag{4.53}$$

where $\mathcal{J}(f)$ represents the least-squares functional defined in Eq.(4.50).

A system of equations is obtained by substituting $f = f + \epsilon\Phi$ and $\lambda = \lambda + \epsilon_c\Psi$ and taking the partial derivatives of $\mathcal{I}$ with respect to ϵ and ϵ_c:

$$\lim_{\epsilon, \epsilon_c \to 0} \frac{\partial}{\partial \epsilon} \mathcal{I}(f + \epsilon\Phi, \lambda + \epsilon_c\Psi) = 0, \quad \forall \Phi \in X(\Omega) \quad \forall \Psi \in M(\Omega) \tag{4.54}$$

$$\lim_{\epsilon, \epsilon_c \to 0} \frac{\partial}{\partial \epsilon_c} \mathcal{I}(f + \epsilon\Phi, \lambda + \epsilon_c\Psi) = 0, \quad \forall \Phi \in X(\Omega) \quad \forall \Psi \in M(\Omega) \tag{4.55}$$

This result yields the following mixed formulations:

Find $(f, \lambda) \in X(\Omega) \times M(\Omega)$ such that:

$$\begin{cases} A(f, \Phi) + B(\Phi, \lambda) = F(\Phi) & \forall \Phi \in X(\Omega), \\ B(f, \Psi) = 0 & \forall \Psi \in M(\Omega) \end{cases} \tag{4.56}$$

where the space $X(\Omega)$ consists of the function f and the space $M(\Omega)$ consists of the function λ. Note that in general X and M can be different function spaces. The bilinear form A and its corresponding right-hand side linear form F are defined as

$$A(f, \Phi) = \langle \mathscr{L} f, \mathscr{L} \Phi \rangle_{Y(\Omega)} \tag{4.57}$$

$$F(\Phi) = \langle g, \mathscr{L} \Phi \rangle_{Y(\Omega)} \tag{4.58}$$

where $A : X \times X \to \mathbb{R}$ is a symmetric, continuous bilinear form, and $F : X \to \mathbb{R}$ a continuous linear form.

The bilinear form $B(\Phi, \lambda)$ is given by:

$$B(\Phi, \lambda) = \langle \lambda, \nabla \cdot \left[\left(\int_{\Omega_r} \Phi \, \mathrm{vol}(\xi) \, d\xi \right) \mathbf{v}_d \right] \rangle_{S(\Omega)} \tag{4.59}$$

Then, the constrained minimization problem (4.52) is equivalent to the unconstrained optimization problem of finding saddle points $(f, \lambda) \in Y \times S$ of the Lagrangian functional Eq.(4.59).

The equation system of the mass conservative PBE problem is formulated by introducing a similar polynomial expansion for the variable λ.

$$\lambda(\xi, r, t) = \sum_{k=1}^{M_\xi+1} \sum_{l=1}^{M_r+1} \sum_{m=1}^{M_t+1} \lambda_{klm} \psi_k(\xi) \psi_l(r) \psi_m(t) \tag{4.60}$$

on $\mathbb{P}_M(\Omega)$ and

$$\dim\left(\mathbb{P}_M(\Omega)\right) = (M_\xi + 1) \times (M_r + 1) \times (M_t + 1) = M^t \quad \text{in} \quad \mathbb{R}^3$$

in which M^t is the total number of degree of freedom.

Using the approximation (4.60), together with (4.43) in the weak formulation (4.56), the following linear algebraic matrix system is obtained for the mass conservative PBE problem.

$$\begin{bmatrix} \mathbf{A}_e & \mathbf{B}^T \\ \mathbf{B} & \mathbf{0} \end{bmatrix} \begin{bmatrix} \mathbf{f}_e \\ \boldsymbol{\lambda} \end{bmatrix} = \begin{bmatrix} \mathbf{F}_e \\ \mathbf{G} \end{bmatrix} \tag{4.61}$$

or

$$\mathbf{A}_c \mathbf{f}_c = \mathbf{F}_c \tag{4.62}$$

where,

$$\mathbf{A}_c = \begin{bmatrix} \mathbf{A}_e & \mathbf{B}^T \\ \mathbf{B} & \mathbf{0} \end{bmatrix}, \quad \mathbf{f}_c = \begin{bmatrix} \mathbf{f}_e \\ \boldsymbol{\lambda} \end{bmatrix} \quad \text{and } \mathbf{F}_c = \begin{bmatrix} \mathbf{F}_e \\ \mathbf{G} \end{bmatrix}$$

in which $\mathbf{A}_e$, $\mathbf{F}_e$ are defined in (4.45) and (4.46), respectively. The matrix $\mathbf{B} \in \mathbb{R}^{(M^t \times N^t)}$,

$$[\mathbf{B}]_{ij} = B(\Phi_j, \Psi_i) = \langle \Psi_i, \left[\left(\int_{\Omega_r} \Phi_j \text{vol}(\xi)\, d\xi \right) \mathbf{v}_d \right] \rangle_{Y(\Omega_e)} \tag{4.63}$$

for $1 \leq i \leq N^t$ and $1 \leq j \leq M^t$.

The vectors $\boldsymbol{\lambda}$, $\mathbf{G} \in \mathbb{R}^{(M^t \times 1)}$, the matrix $\mathbf{A}_c \in \mathbb{R}^{(N^t+M^t)\times(N^t+M^t)}$, and the vectors $\mathbf{f}_c$, $\mathbf{F}_c \in \mathbb{R}^{(N^t+M^t)\times 1}$.

The obtained system (4.61) corresponds to a saddle-point problem (see proof in Appendix. D), and proper function spaces need to be chosen to satisfy the Ladyzhenskaja-Babuška-Brezzi (LBB) condition.

Due to the similarity with the mixed formulation of the Stokes problem [77], the discrete space for the Lagrange multiplier, λ, needs to be particularly chosen to render a stable discretization. If variable f is approximated by polynomials of degree N^t, then the discrete *inf-sup* condition can be satisfied by approximating the variable λ by a polynomials of order $M^t = N^t - 2$.

Numerical test and results

In the paper entitled "Mass conservative solution of the population balance equation using the least-squares spectral element method" (Appendix E.4), the author studies the evolution of the bubble size distribution of an air-water two-phase mixture moving through a 2D rectangular channel to assess the overall mass conservative properties of the standard and constrained least-squares formulations of a breakage-only PBE in which the Martinez-Bazan [59] breakage kernel is applied. Using the Gauss' theorem and the definition of

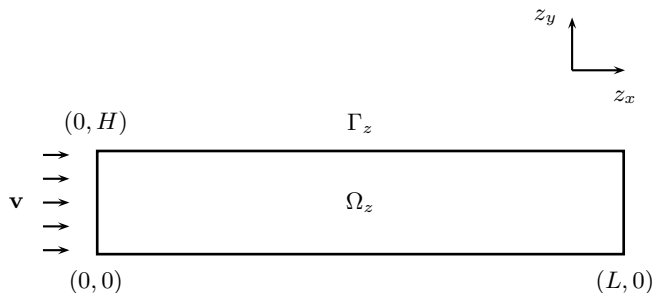

Figure 4.2: The external domain of the test case problem. The gas-liquid mixture is fed from the inlet at constant velocity. Bubble breakup is taking place within the domain.

the void fraction Eq.(4.31), a space boundary integral of the dispersed phase continuity equation (4.51) can be cast into

$$\int_{\Omega_r} \nabla \cdot (\alpha \mathbf{v}_d)\ d\Omega_r = \int_{\Gamma_r} (\alpha \mathbf{v}_d) \cdot \mathbf{n}\, d\Gamma_r \tag{4.64}$$

where Γ_r represents the boundary of the channel and where $\mathbf{n}$ represents the outward unit vector. $\mathbf{v}_d$ denotes the velocity field.

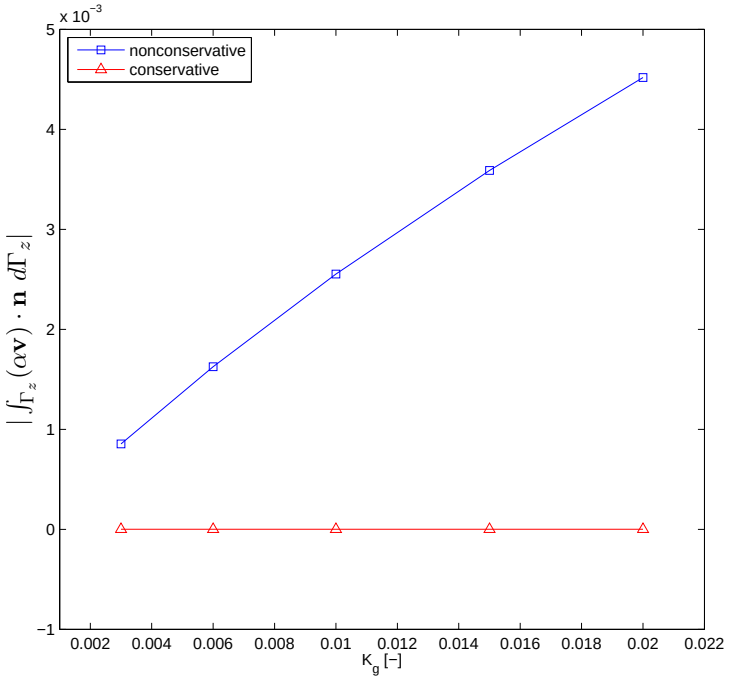

Figure 4.3: The boundary integral values predicted by the standard (i.e., mass nonconservative) LSM and the constrained (i.e., mass conservative) LSM.

For comparison the absolute value of the boundary integrals of the standard LSM and the constrained LSM has been plotted as a function of the breakage kernel parameter (K_g) in Figure 4.3. The breakage parameter (K_g) has been varied from 3.0×10^{-3} to 2.0×10^{-2}. The higher the K_g value, the stronger the breakage rate. From the figure it can be seen that the value of boundary integral of the mass nonconservative LSM grows with the breakage rate, hence the conservation properties are increasingly affected as the breakage rate grows. In contrast, the result from the constrained LSM shows the divergence of the velocity times the void fraction is close to zero at any breakage rate, indicating the mass conservation has been strictly satisfied to machine accuracy.

Figure 4.4 shows plots of the different evolutions of the density function f along z_x at the centerline of the channel as predicted by the standard LSM and constrained LSM are given. Outtakes reveals that notable deviations of the number densities exist for larger bubbles as the profile of f of the larger bubble part has been zoomed in.

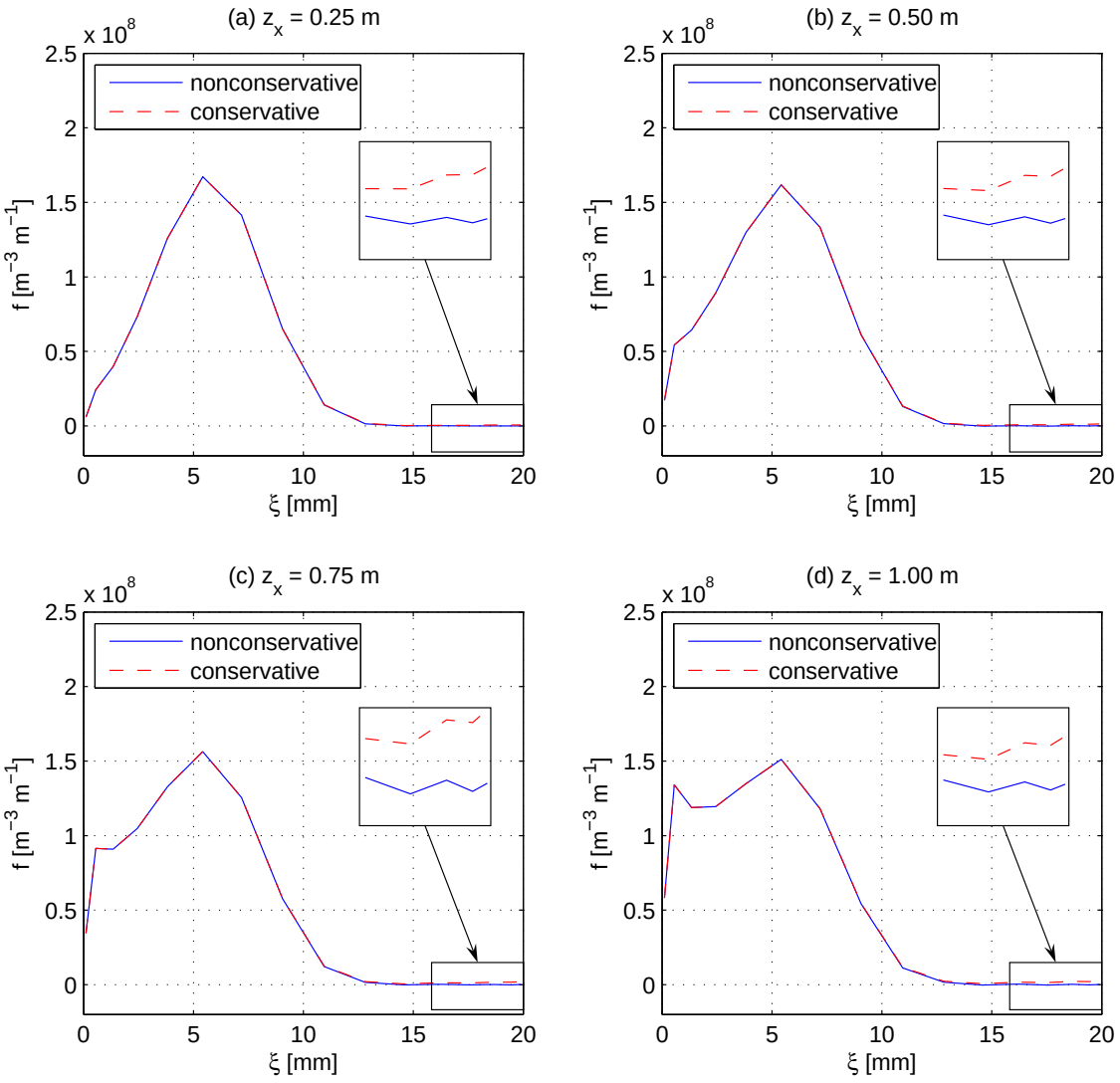

Figure 4.4: Comparisons of axial evolution of the bubble size distribution at (a) $z_x = 0.00$ m, (b) $z_x = 0.25$ m, (c) $z_x = 0.50$ m and (d) $z_x = 1.00$ m at centerline ($z_y = 0.1$m) with $K_g = 6.0 \times 10^{-3}$.

The number of large bubbles predicted by the mass conservative method is higher than that of the nonconservative method, whereas the number of the smaller bubbles remains almost unchanged. A comparison of these number density profiles indicates that the improved mass conservation of the LSM is obtained at the expense of emergence of large bubbles. This behavior can be understood if one realize that the LSM tries to find a solution of f by minimizing the residuals of both the PBE (Eqs.(4.41) and (4.42)) and the dispersed phase continuity equation (Eq.(4.51)) which are discretized on the domain of interest, simultaneously. Considering that in many engineering problems the moments of the density function usually get more attention than the density function itself, the constrained LSM can be an attractive fix to these mass nonconservative breakage kernels.

However, the use of the Lagrange multipliers undermines one of the main advantages of the LSM. One sacrifices one of the appealing properties of the least-squares formulation - the positive definiteness, which may led to indefinite problems similar to those arising in the standard Galerkin formulations of the Stokes equations [77]. Secondly, in addition to the variables needed to obtain the first order least-squares formulations, one needs an additional Lagrange multiplier, λ. And finally, an additional compatibility requirement (e.g., the LBB condition), not present in the standard least-squares implementations, enters the formulation to guarantee a unique solution.

For more detailed discussions on the issue of the mass conservative formulation of the PBE, we refer to the paper in Appendix E.4.

Chapter 5

Numerical Solution of the Bubble Column Model

5.1 Introduction

In the present chapter, we will formulate the system of equations denoting the bubble column model, and discuss the coupling between the multi-fluid and the PBE model. In particular, an example of using the least-squares spectral element method for solving the entire one-dimensional bubble column model with a novel iteration algorithm is presented.

5.2 The combined multi-fluid and PBE model

The multiphase system, consisting of bubbles and fluid, might be described by a two-fluid model, in which the fluid surrounding the bubbles is modeled as the primary phase and the entire gas phase is modeled as an unique secondary phase (see Figure 5.1). The dynamics of the bubbles and the surrounding fluid dynamics can also be described by the multi-fluid model, in which the fluid surrounding the particles is modeled as the primary phase and the population of particles is modeled by N secondary phases, each one has its own size group and velocity field (see Figure 5.2).

The system of equations of the multi-fluid model is

Mass conservation of the primary phase

$$\frac{\partial}{\partial t}(\alpha_c \rho_c) + \nabla \cdot (\alpha_c \rho_c \mathbf{v}_c) = \Gamma_c \tag{5.1}$$

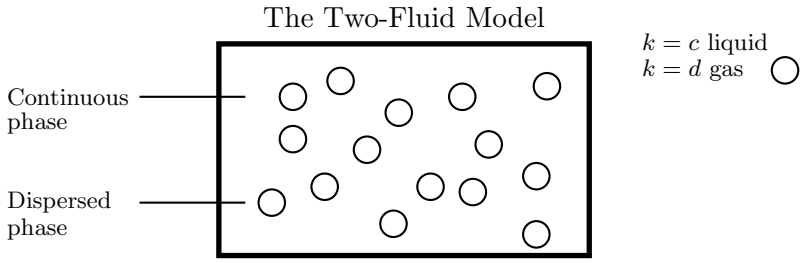

Figure 5.1: The two-fluid model.

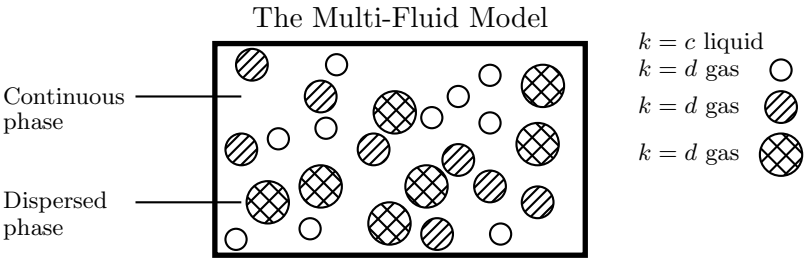

Figure 5.2: The multi-fluid model.

Mass conservation of the secondary phases

$$\frac{\partial}{\partial t}(\alpha_d \rho_d) + \nabla \cdot (\alpha_d \rho_d \hat{\mathbf{v}}_d) = \Gamma_d \quad d = 1, \cdots, N. \tag{5.2}$$

Volume fraction constraint

$$\alpha_c + \sum_{d=1}^{N} \alpha_d = 1 \tag{5.3}$$

Momentum balance of the primary phase

$$\begin{aligned} \frac{\partial}{\partial t}(\alpha_c \rho_c \mathbf{v}_c) + \nabla \cdot (\alpha_c \rho_c \mathbf{v}_c \mathbf{v}_c) = & -\alpha_c \nabla P_c + \nabla \cdot \left(\alpha_c \left(\mathbf{T}_c + \mathbf{T}_c^{Re}\right)\right) \\ & + \alpha_c \rho_c \mathbf{g} + \mathbf{M}_c^{\tau}. \end{aligned} \tag{5.4}$$

Momentum balance of the secondary phase

$$\begin{aligned} \frac{\partial}{\partial t}(\alpha_d \rho_d \hat{\mathbf{v}}_d) + \nabla \cdot (\alpha_d \rho_d \hat{\mathbf{v}}_d \hat{\mathbf{v}}_d) = & -\alpha_d \nabla P_d + \nabla \cdot \left(\alpha_d \left(\hat{\mathbf{T}}_d + \hat{\mathbf{T}}_d^{Re}\right)\right) \\ & + \alpha_d \rho_d \mathbf{g} + \mathbf{M}_d^{\tau}. \qquad d = 1, \cdots, N. \end{aligned} \tag{5.5}$$

Here, $\hat{\mathbf{v}}_d$ is the velocity of the d^{th} phase or the representative velocity of the d^{th} velocity class $[\xi_d, \xi_{d+1})$. The average particle size of the d^{th} velocity class is

$$\hat{\xi}_d = \frac{\alpha_d}{N_d} = \frac{\int_{\xi_d}^{\xi_{d+1}} \text{vol}(\xi) f(\xi, \mathbf{r}, t)\, d\xi}{\int_{\xi_d}^{\xi_{d+1}} f(\xi, \mathbf{r}, t)\, d\xi} \tag{5.6}$$

in which, $\text{vol}(\xi) = \frac{\pi}{6}\xi^3$ is the volume of a spherical particle of diameter ξ.

The dispersed phase size distribution is described by the population balance equation

$$\frac{\partial f(\xi, \mathbf{r}, t)}{\partial t} + \nabla \cdot (f(\xi, \mathbf{r}, t)\mathbf{v}(\xi, \mathbf{r}, t)) = h(f, \xi, \mathbf{r}, t, \mathbf{Y}) \tag{5.7}$$

in which, the velocity $\mathbf{v}(\xi, \mathbf{r}, t)$ is a function of both internal and external coordinates, which can be expressed by the velocities of each velocity class

$$\mathbf{v}(\xi, \mathbf{r}, t) = \begin{cases} \hat{\mathbf{v}}_1(\mathbf{r}, t), & \xi \in [\xi_1, \xi_2) \\ \hat{\mathbf{v}}_2(\mathbf{r}, t), & \xi \in [\xi_2, \xi_3) \\ \cdots & \cdots \\ \hat{\mathbf{v}}_d(\mathbf{r}, t), & \xi \in [\xi_d, \xi_{d+1}) \\ \cdots & \cdots \\ \hat{\mathbf{v}}_N(\mathbf{r}, t), & \xi \in [\xi_N, \xi_{N+1}) \end{cases} \tag{5.8}$$

The volume fractions of the secondary phases particles within the size interval $[\xi_d, \xi_{d+1})$ can be recovered directly from the density function, f, as follows

$$\alpha_d(\mathbf{r}, t) = \int_{\xi_d}^{\xi_{d+1}} \text{vol}(\xi) f(\xi, \mathbf{r}, t)\, d\xi. \tag{5.9}$$

The mass conservation equations (5.2) can be excluded from the system. The new determined system will include the mass conservation equation for the primary phase, Eq.(5.1), the momentum equations for all phases, Eqs.(5.4) and (5.5), and the population balance equation, Eq.(5.7).

5.3 Coupled solver

Normally the coupling of the multi-fluid model and the PBE model requires that each part being solved by an independent numerical method. Therefore, methods like the FVM (see Chapter 3) are applied for the stand-alone multi-fluid model, whereas methods like the CM, QMOM and DQMOM (see Chapter 4) are used to solve the PBE. Some coupling of these models are required. In this Chapter, the applicability of using the LSM as both the multi-fluid solver and the PBE solver is discussed.

For all the methods mentioned, information must be passed between the flow solver and the PBE solver (see Figure 5.3). Values of the dispersed phase velocity field and hydrodynamics parameters which are evaluated by the multi-fluid solver and required by the breakage and aggregation kernels are delivered to the PBE solver. On the other hand, the moments of the density functions, in particular the information on particle size distribution can be computed by the PBE solver and passed back to the multi-fluid solver.

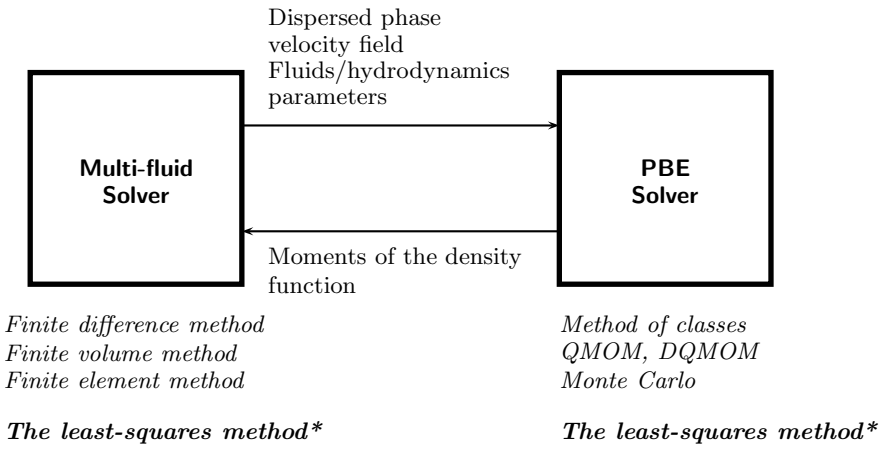

Figure 5.3: The information exchange between a multi-fluid solver and a population balance equation solver.

The conventional approach to solve the two-fluid model coupled with the PBE uses only one common momentum equation for all bubble sizes (e.g., the homogeneous MUSIG model, see [61]). The dispersed phase is divided into M size fractions. The population balance equation is applied to describe the size fractions taking into account the inter-fraction mass transfer resulting due to bubble coalescence and breakup (Figure 5.4). With a sufficient number of size fractions being used, the volume fraction of the dispersed phase α_g and the Sauter diameter ξ_{32} can be obtained by Eq.(4.32), which are required by the two-fluid model.

Mathematically, these approaches are based on the population balance equation and the two-fluid model. The assumption that all bubbles move at the same velocity restricts its applicability to homogeneous dispersed flows, where the slip velocities of the particles are almost independent of particle size and the particle relaxation time is sufficiently small with respect to inertial time scales. The model is also unable to predict the radial migration of small and large bubbles in vertical pipes where the lift forces plays an essential role on the bubble motion.

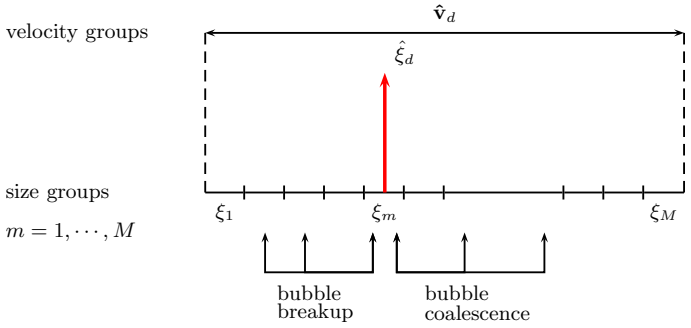

Figure 5.4: The population balance equation solved by the method of classes with one velocity group.

A more sophisticated approach (e.g., like that inhomogeneous MUSIG, [51]) that takes into account the different dispersed phases, must rigorously solve the complete set of balance equations for each phase. In practice, the gaseous disperse phase is divided into a number N of so-called velocity groups (or phases), where each of the velocity groups is characterized by its own velocity field. Furthermore, the overall bubble size distribution is represented by dividing the bubble diameter range within each of the velocity groups d into a number of sub-size fractions $M_d, \quad d = 1, \cdots, N$. The population balance model considering bubble coalescence and bubble breakup is applied to the sub-size groups (see Figure 5.5). Unlike the one velocity group approach, the mass exchange due to the coalescence and breakage can exceed the size ranges assigned to the velocity groups.

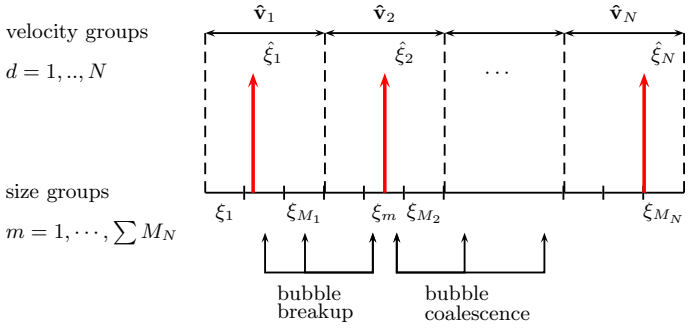

Figure 5.5: The population balance equation solved by the method of classes with multiple velocity groups (inhomogeneous MUSIG [51]).

With the QMOM approach, the PBE Eq.(5.7) is integrated over its internal coordinate and the low-order moments can be directly computed from Eq.(4.35). The QMOM [55] provides an attractive alternative solving the PBE associated with the multiphase flow model, especially when aggregation quantities, rather than an exact PSD, are desired. Its advantages are fewer variables (typically only six or eight moments) and a dynamic calculation of the size bins. The disadvantages are that the number of abscissas may not be adequate to describe the PSD, the Product-Difference (PD) algorithm may be time consuming, and the PD algorithm itself is ill-conditioned [23]. The applicability of QMOM is limited to no more than 12 moments[69], and the QMOM also has problem handling systems where there is a strong dependence of the dispersed-phase velocity on the internal coordinates [65].

When the least-squares method is applied to the system that consists of both flow and PBE models, the bubble number density function $f(\xi, \mathbf{r}, t)$ is approximated by the Lagrangian polynomials. The h/p-refinement can be easily used to solve both the single dispersed phase approach (one velocity group) and the multiple dispersed phase approach (multi-velocity group).

In the case of a single velocity group, the least-squares problem domain is defined such that it includes both the internal and external coordinates. In the internal coordinates, a Lagrangian polynomials of order Q can be chosen to approximate the solution results in

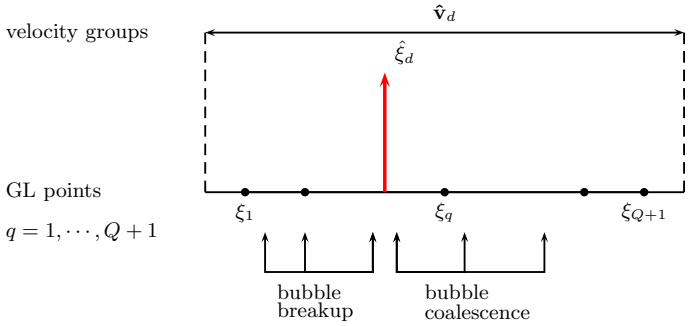

Figure 5.6: The population balance equation solved by the least-squares method with one velocity group.

$Q+1$ nodal points (see Figure 5.6). Unlike the MUSIG size group, these nodal points are now located at the GL quadrature points rather than being equally distributed.

The moments of any order can be calculated by

$$m^{(k)}(\mathbf{r},t) = \int_{\xi_{min}}^{\xi_{max}} f(\xi,\mathbf{r},t)\xi^k \, d\xi \approx \sum_{q=1}^{Q+1} w_q \xi_q^k f(\xi_q,\mathbf{r},t) \tag{5.10}$$

in which, $\xi_q \in (\xi_{min}, \xi_{max})$ and w_q are the quadrature points and weights in internal coordinate.

In the multiple velocity approach, the h-refinement can divide the internal coordinate into N subelements and the Lagrangian polynomials of order Q_d that corresponds to $Q_d + 1$ nodal quadrature points, are assigned within each subelement (see Figure 5.7).

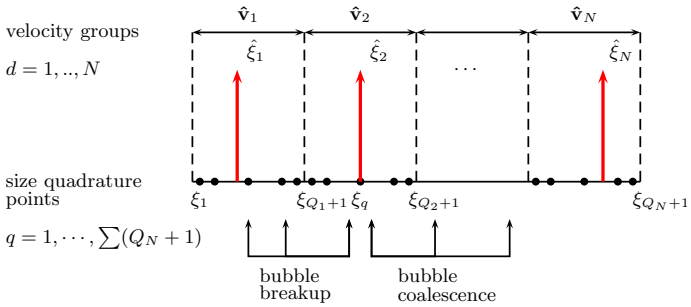

Figure 5.7: The population balance equation solved by the least-squares method with multiple velocity groups.

A number of N velocity groups can be assigned over the subelements. One velocity group can range over one or more subelements and the moments of each velocity group is the

summation of all contributions of each subelement.

$$m^{(k)}(\mathbf{r},t) = \sum_{d=1}^{N} m_d^{(k)} = \sum_{d=1}^{N} \int_{\xi_{d,min}}^{\xi_{d,max}} f(\xi,\mathbf{r},t)\xi^k \, d\xi$$
$$\approx \sum_{d=1}^{N} \sum_{q=1}^{Q+1} w_q \xi_q^k f(\xi_q,\mathbf{r},t) \quad d = 1,\cdots,N. \tag{5.11}$$

The lower and upper boundaries of bubble size intervals ($\xi_{d,min}$ and $\xi_{d,max}$) for the velocity groups can be controlled by either an equal bubble size distribution, an equal bubble mass distribution or can be based on a user defined bubble size range for each distinct bubble size.

The division of the velocity groups should be based on the physics of bubble motion for bubbles of different sizes (e.g., different behavior of differently sized bubbles with respect to lift force or turbulent dispersion). Therefore, it can be suggested that in most cases $N = 2$ or 3 velocity groups are sufficient in order to capture the main phenomena in bubbly or slug flows.

5.4 A cross-section averaged bubble column model solved by the LSM

5.4.1 A column-section averaged bubble column model

As discussed in Chapter 3, the length-based steady-state PBE considering the breakage and coalescence can be written as

$$\frac{\partial\left(vf(\xi,z)\right)}{\partial z} = \mathcal{B}^+(\xi,z) - \mathcal{B}^-(\xi,z) + \mathcal{A}^+(\xi,z) - \mathcal{A}^-(\xi,z) \tag{5.12}$$

in which,

$$\mathcal{B}^+(\xi,z) = \int_{\xi}^{\xi_{max}} \nu P(\xi,\zeta) b(\zeta) f(\zeta,z) d\zeta \tag{5.13}$$
$$\mathcal{B}^-(\xi,z) = b(\xi) f(\xi,z) \tag{5.14}$$
$$\mathcal{A}^+(\xi,z) = \frac{\xi^2}{2} \int_{\xi_{min}}^{\xi} \frac{a((\xi^3-\zeta^3)^{1/3},\zeta)}{(\xi^3-\zeta^3)^{2/3}} f(\zeta,z) f((\xi^3-\zeta^3)^{1/3},z) d\zeta \tag{5.15}$$
$$\mathcal{A}^-(\xi,z) = f(\xi,z) \int_{\xi_{min}}^{(\xi_{max}^3-\xi^3)^{1/3}} a(\xi,\zeta) f(\zeta,z) d\zeta \tag{5.16}$$

where ξ and ζ represent the bubble diameter.

and the cross-section averaged two-fluid model was derived in Section (3.5)

$$\begin{aligned}
\alpha_d\frac{dP}{dz} + K_d\hat{v}_d - K_d v_c =& -\rho_d\alpha_d\hat{v}_d\frac{d\hat{v}_d}{dz} + \mu_d\alpha_d\frac{du_d}{dz} \\
&+ \mu_d u_d\frac{d\alpha_d}{dz} - \alpha_d\rho_d g && (5.17)\\
(1-\alpha_d)\frac{dP}{dz} + K_d v_c - K_d\hat{v}_d =& -\rho_c(1-\alpha_d)v_c\frac{dv_c}{dz} + \mu_c(1-\alpha_d)\frac{du_c}{dz} \\
&- \mu_c u_c\frac{d\alpha_d}{dz} - (1-\alpha_d)\rho_c g && (5.18)\\
(1-\alpha_d)\frac{dv_c}{dz} - v_c\frac{d\alpha_d}{dz} =& 0 && (5.19)\\
\frac{d\hat{v}_d}{dz} - u_d =& 0 && (5.20)\\
\frac{dv_c}{dz} - u_c =& 0 && (5.21)
\end{aligned}$$

Note that the gas phase mass transfer equation has been excluded as the void fraction can be obtained from the PBE (5.12).

5.4.2 The least-squares formulation

We can write the system of linearized bubble column model equations for the PBE:

$$\mathscr{L}_{\text{PB}}\mathbf{f}_{\text{PB}} = \mathbf{g}_{\text{PB}}, \quad \text{in} \quad \Omega_{\text{PB}} \in \mathbb{R}^2 \tag{5.22}$$

$$\mathscr{B}_{\text{PB}}\mathbf{f}_{\text{PB}} = \mathbf{h}_{\text{PB}}, \quad \text{on} \quad \Gamma_{\text{PB}} \tag{5.23}$$

and the cross-sectional averaged two-fluid model equations:

$$\mathscr{L}_{\text{MF}}\mathbf{f}_{\text{MF}} = \mathbf{g}_{\text{MF}}, \quad \text{in} \quad \Omega_{\text{MF}} \in \mathbb{R}^1 \tag{5.24}$$

$$\mathscr{B}_{\text{MF}}\mathbf{f}_{\text{MF}} = \mathbf{h}_{\text{MF}}, \quad \text{on} \quad \Gamma_{\text{MF}} \tag{5.25}$$

in which $\mathscr{L}_{\text{PB}}$ and $\mathscr{L}_{\text{MF}}$ are first-order partial differential operators. $\Omega_{\text{PB}} \in \mathbb{R}^2$ and $\Omega_{\text{MF}} \in \mathbb{R}^1$ are bounded domains with piecewise smooth boundary Γ_{PB} and Γ_{MF}, respectively. The number of the space dimensions of the PBE problem is 2 as it includes both internal and external coordinates, while that of the two-fluid model is 1 as it only has external coordinate. $\mathbf{f}_{\text{PB}}$ is the unknown density function n of $\mathbf{x}_{\text{PB}} = (\xi, z)$, and $\mathbf{f}_{\text{MF}}^{\text{T}} = (\hat{v}_d, p, v_c, u_d, u_c)$ is a vector of 5 unknown functions of $\mathbf{x}_{\text{MF}} = z$. $\mathbf{g}_{\text{PB}}$ and $\mathbf{g}_{\text{MF}}$ are given vector-valued functions. $\mathscr{B}_{\text{PB}}$ and $\mathscr{B}_{\text{MF}}$ are algebraic boundary operators, and $\mathbf{h}_{\text{PB}}$, $\mathbf{h}_{\text{MF}}$ are given vector-valued functions on the boundary Γ_{PB} and Γ_{MF}, respectively. The definitions of the problem operators $\mathscr{L}_{\text{PB}}$, $\mathscr{L}_{\text{MF}}$, the boundary operators $\mathscr{B}_{\text{PB}}$, $\mathscr{B}_{\text{MF}}$, and the source terms $\mathbf{g}_{\text{PB}}$, $\mathbf{g}_{\text{MF}}$, $\mathbf{h}_{\text{PB}}$ and $\mathbf{h}_{\text{MF}}$ are outlined as follows. The linearized PBE

operator $\mathscr{L}_{\text{PB}}$ can be expressed as the summation of several sub-operators:

$$\begin{aligned}
\mathscr{L}_{\text{PB}}\{\mathbf{f}_{\text{PB}}\} &= \mathscr{L}_{\text{PB}}\{f(\xi,z)\} \\
&= \underbrace{\frac{\partial}{\partial z}(vf(\xi,z))}_{\text{convection}} \\
&+ \underbrace{b(\xi)f(\xi,z)}_{\text{breakage death}} - \underbrace{\int_{\xi}^{\xi_{max}} \nu P(\xi,\zeta)b(\zeta)f(\zeta,z)d\zeta}_{\text{breakage birth}} \\
&+ \underbrace{f(\xi,z)\int_{\xi_{min}}^{(\xi_{max}^3-\xi^3)^{1/3}} a(\xi,\zeta)f^*(\zeta,z)d\zeta}_{\text{aggregation death}} \\
&- \underbrace{\frac{\xi^2}{2}\int_{\xi_{min}}^{\xi} \frac{a((\xi^3-\zeta^3)^{1/3},\zeta)}{(\xi^3-\zeta^3)^{2/3}} f^*(\zeta,z)f((\xi^3-\zeta^3)^{1/3},z)d\zeta}_{\text{aggregation birth}}
\end{aligned} \tag{5.26}$$

with the source term $\mathbf{g}_{\text{PB}}$:

$$\mathbf{g}_{\text{PB}}(\xi,z) = 0 \tag{5.27}$$

After rearrangement of the Eq.(5.17), (5.18), (5.19), (5.20) and (5.21), the linearized cross-sectional averaged two-fluid model operator can be defined as:

$$\begin{aligned}
\mathscr{L}_{\text{MF}}\{\mathbf{f}_{\text{MF}}(z)\} = &\begin{bmatrix} 0 & \frac{\alpha_d^*}{K_d^*} & 0 & 0 & 0 \\ 0 & \frac{1-\alpha_d^*}{K_d^*} & 0 & 0 & 0 \\ 0 & 0 & (1-\alpha_d^*) & 0 & 0 \\ 1 & 0 & 0 & 0 & 0 \\ 0 & 0 & 1 & 0 & 0 \end{bmatrix} \frac{d\mathbf{f}_{\text{MF}}(z)}{dz} \\
&+ \begin{bmatrix} \frac{K_d^*}{K_d^*} & 0 & -\frac{K_d^*}{K_d^*} & 0 & 0 \\ -\frac{K_d^*}{K_d^*} & 0 & \frac{K_d^*}{K_d^*} & 0 & 0 \\ 0 & 0 & -\frac{d\alpha_d^*}{dz} & 0 & 0 \\ 0 & 0 & 0 & -1 & 0 \\ 0 & 0 & 0 & 0 & -1 \end{bmatrix} \mathbf{f}_{\text{MF}}(z)
\end{aligned} \tag{5.28}$$

with the source term:

$$\mathbf{g}_{\text{MF}}(z) = \begin{bmatrix} \frac{1}{K_d^*}\left[-\alpha_d^*\rho_d g - \rho_d\alpha_d^*\hat{v}_d^*\frac{d\hat{v}_d^*}{dz} + \mu_d^* u_d^*\frac{d\alpha}{dz} + \mu_d^*\alpha_d^*\frac{du_d^*}{dz} + M_d^{\text{wall}}\right] \\ \frac{1}{K_d^*}\begin{bmatrix} -(1-\alpha_d^*)\rho_c g - \mu_c^* u_c^*\frac{d\alpha_d^*}{dz} \\ +\rho_c(1-\alpha_d^*)v_c^*\frac{dv_c^*}{dz} + \mu_c^*(1-\alpha_d^*)\frac{du_c^*}{dz} + M_c^{\text{wall}} \end{bmatrix} \\ 0 \\ 0 \\ 0 \end{bmatrix} \tag{5.29}$$

in which, u_d and u_c are introduced as 1st-order derivatives of gas and liquid velocity in order to reduce the differential order of the two-fluid model to the standard first-order system. Note the terms with an asterisk (*) indicates it's known from the previous iteration step.

It is assumed that the system is well-posed. The least–squares formulation minimizes the residual of a norm-equivalent functional. The norm–equivalent functional for the system is given by

$$\mathcal{J}(\mathbf{f}_{\text{PB}}, \mathbf{f}_{\text{MF}}) = \mathcal{J}_{\text{PB}}(\mathbf{f}_{\text{PB}}) + \mathcal{J}_{\text{MF}}(\mathbf{f}_{\text{MF}}) \tag{5.30}$$

in which,

$$\begin{cases} \mathcal{J}_{\text{PB}}(\mathbf{f}_{\text{PB}}) & = \frac{1}{2}\|\mathscr{L}_{\text{PB}}\mathbf{f}_{\text{PB}} - \mathbf{g}_{\text{PB}}\|^2_{Y_{\text{PB}}(\Omega_{\text{PB}})} + \frac{1}{2}\|\mathscr{B}_{\text{PB}}\mathbf{f}_{\text{PB}} - \mathbf{h}_{\text{PB}}\|^2_{Y_{\text{PB}}(\Gamma_{\text{PB}})} \\ \mathcal{J}_{\text{MF}}(\mathbf{f}_{\text{MF}}) & = \frac{1}{2}\|\mathscr{L}_{\text{MF}}\mathbf{f}_{\text{MF}} - \mathbf{g}_{\text{MF}}\|^2_{Y_{\text{MF}}(\Omega_{\text{MF}})} + \frac{1}{2}\|\mathscr{B}_{\text{MF}}\mathbf{f}_{\text{MF}} - \mathbf{h}_{\text{MF}}\|^2_{Y_{\text{MF}}(\Gamma_{\text{MF}})} \end{cases} \tag{5.31}$$

with the norm defined like

$$\| \bullet \|^2_{Y(\Omega)} = < \bullet, \bullet >_{Y(\Omega)} = \int_{\Omega} \bullet \bullet \, d\Omega \tag{5.32}$$

$$\| \bullet \|^2_{Y(\Gamma)} = < \bullet, \bullet >_{Y(\Gamma)} = \int_{\Gamma} \bullet \bullet \, d\Gamma \tag{5.33}$$

A system of equations is obtained by substituting $\mathbf{f}_{\text{PB}} = \mathbf{f}_{\text{PB}} + \varepsilon_{\text{PB}}\mathbf{v}_{\text{PB}}$ and $\mathbf{f}_{\text{MF}} = \mathbf{f}_{\text{MF}} + \varepsilon_{\text{MF}}\mathbf{v}_{\text{MF}}$ and take the partial derivative of $\mathcal{J}$ with respect to ε_{PB} and ε_{MF}.

The minimization statement is equivalent to: find $\mathbf{f}_{\text{PB}} \in X_{\text{PB}}(\Omega_{\text{PB}})$ and $\mathbf{f}_{\text{MF}} \in X_{\text{MF}}(\Omega_{\text{MF}})$ such that

$$\begin{cases} \lim_{\epsilon_{1,2}\to 0} \frac{\partial}{\partial \epsilon_{\text{PB}}} \mathcal{J}(\mathbf{f}_{\text{PB}} + \epsilon_{\text{PB}}\mathbf{v}_{\text{PB}}, \mathbf{f}_{\text{MF}} + \varepsilon_{\text{MF}}\mathbf{v}_{\text{MF}}) = 0, & \forall \mathbf{v}_{\text{PB}} \in X_{\text{PB}}(\Omega_{\text{PB}}) \\ \lim_{\epsilon_{1,2}\to 0} \frac{\partial}{\partial \epsilon_{\text{MF}}} \mathcal{J}(\mathbf{f}_{\text{PB}} + \epsilon_{\text{PB}}\mathbf{v}_{\text{PB}}, \mathbf{f}_{\text{MF}} + \varepsilon_{\text{MF}}\mathbf{v}_{\text{MF}}) = 0, & \forall \mathbf{v}_{\text{MF}} \in X_{\text{MF}}(\Omega_{\text{MF}}) \end{cases} \tag{5.34}$$

where $X_{\text{PB}}(\Omega_{\text{PB}})$ and $X_{\text{MF}}(\Omega_{\text{MF}})$ are the space of the admissible functions. $\mathbf{v}_{\text{PB}}$ and $\mathbf{v}_{\text{MF}}$ are arbitrary trial functions and ε_{PB} and ε_{MF} are small perturbations. Consequently, the necessary condition can be written as:

Find $\mathbf{f}_{\text{PB}} \in X_{\text{PB}}(\Omega_{\text{PB}})$ and $\mathbf{f}_{\text{MF}} \in X_{\text{MF}}(\Omega_{\text{MF}})$ such that

$$\begin{cases} A_{\text{PB}}(\mathbf{f}_{\text{PB}}, \mathbf{v}_{\text{PB}}) = F_{\text{PB}}(\mathbf{v}_{\text{PB}}) & \forall \mathbf{v}_{\text{PB}} \in X_{\text{PB}}(\Omega_{\text{PB}}) \\ A_{\text{MF}}(\mathbf{f}_{\text{MF}}, \mathbf{v}_{\text{MF}}) = F_{\text{MF}}(\mathbf{v}_{\text{MF}}) & \forall \mathbf{v}_{\text{MF}} \in X_{\text{MF}}(\Omega_{\text{MF}}) \end{cases} \tag{5.35}$$

with

$$\begin{cases} A_{\text{PB}}(\mathbf{f}_{\text{PB}}, \mathbf{v}_{\text{PB}}) & = \langle \mathscr{L}_{\text{PB}}\mathbf{f}_{\text{PB}}, \mathscr{L}_{\text{PB}}\mathbf{v}_{\text{PB}} \rangle_{Y_{\text{PB}}(\Omega_{\text{PB}})} + \langle \mathscr{B}_{\text{PB}}\mathbf{f}_{\text{PB}}, \mathscr{B}_{\text{PB}}\mathbf{v}_{\text{PB}} \rangle_{Y_{\text{PB}}(\Gamma_{\text{PB}})} \\ F_{\text{PB}}(\mathbf{v}_{\text{PB}}) & = \langle \mathbf{g}_{\text{PB}}, \mathscr{L}_{\text{PB}}\mathbf{v}_{\text{PB}} \rangle_{Y_{\text{PB}}(\Omega_{\text{PB}})} + \langle \mathbf{h}_{\text{PB}}, \mathscr{B}_{\text{PB}}\mathbf{v}_{\text{PB}} \rangle_{Y_{\text{PB}}(\Gamma_{\text{PB}})} \\ A_{\text{MF}}(\mathbf{f}_{\text{MF}}, \mathbf{v}_{\text{MF}}) & = \langle \mathscr{L}_{\text{MF}}\mathbf{f}_{\text{MF}}, \mathscr{L}_{\text{MF}}\mathbf{v}_{\text{MF}} \rangle_{Y_{\text{MF}}(\Omega_{\text{MF}})} + \langle \mathscr{B}_{\text{MF}}\mathbf{f}_{\text{MF}}, \mathscr{B}_{\text{MF}}\mathbf{v}_{\text{MF}} \rangle_{Y_{\text{MF}}(\Gamma_{\text{MF}})} \\ F_{\text{MF}}(\mathbf{v}_{\text{MF}}) & = \langle \mathbf{g}_{\text{MF}}, \mathscr{L}_{\text{MF}}\mathbf{v}_{\text{MF}} \rangle_{Y_{\text{MF}}(\Omega_{\text{MF}})} + \langle \mathbf{h}_{\text{MF}}, \mathscr{B}_{\text{MF}}\mathbf{v}_{\text{MF}} \rangle_{Y_{\text{MF}}(\Gamma_{\text{MF}})} \end{cases} \tag{5.36}$$

where $A_{\text{PB}} : X_{\text{PB}} \times X_{\text{PB}} \rightarrow \mathbb{R}$ and $A_{\text{MF}} : X_{\text{MF}} \times X_{\text{MF}} \rightarrow \mathbb{R}$ are symmetric, continuous bilinear forms, and $F_{\text{PB}} : X_{\text{PB}} \rightarrow \mathbb{R}$ and $F_{\text{MF}} : X_{\text{MF}} \rightarrow \mathbb{R}$ are continuous linear forms. Using the these approximations in Eq.(5.36), the following matrix systems are obtained for the PBE problem and the flow problem, respectively.

$$\mathbf{A}_{\text{PB}}\mathbf{f}_{\text{PB}} = \mathbf{F}_{\text{PB}} \tag{5.37}$$

$$\mathbf{A}_{\text{MF}}\mathbf{f}_{\text{MF}} = \mathbf{F}_{\text{MF}} \tag{5.38}$$

We use the superscript ^{t} to denote the total number of degree of freedom over all subelements. The matrix $\mathbf{A}_{\text{PB}} \in \mathbb{R}^{(N_\xi^t \times N_z^t)\times(N_\xi^t \times N_z^t)}$, vectors $\mathbf{f}_{\text{PB}}$, $\mathbf{F}_{\text{PB}} \in \mathbb{R}^{(N_\xi^t \times N_z^t)}$ and matrix $\mathbf{A}_{\text{MF}} \in \mathbb{R}^{(N_z^t \times 5)\times(N_z^t \times 5)}$, vectors $\mathbf{f}_{\text{MF}}$, $\mathbf{F}_{\text{MF}} \in \mathbb{R}^{(N_z^t \times 5)}$ are defined like

$$\begin{aligned}
[\mathbf{A}_{\text{PB}}]_{ij} &= A_{\text{PB}}(\Phi_j, \Phi_i) \\
&= \langle \mathscr{L}_{\text{PB}}\Phi_j, \mathscr{L}_{\text{PB}}\Phi_i \rangle_{Y(\Omega_{\text{PB}})} + \langle \mathscr{B}_{\text{PB}}\Phi_j, \mathscr{B}_{\text{PB}}\Phi_i \rangle_{Y(\Omega_{\text{PB}})} && (5.39)\\
[\mathbf{F}_{\text{PB}}]_i &= F(\Phi_i) = \langle [\mathbf{g}_{\text{PB}}]_i, \mathscr{L}_{\text{PB}}\Phi_i \rangle_{Y(\Gamma_{\text{PB}})} + \langle [\mathbf{h}_{\text{PB}}]_i, \mathscr{B}_{\text{PB}}\Phi_i \rangle_{Y(\Gamma_{\text{PB}})} && (5.40)\\
[\mathbf{f}_{\text{PB}}]_i &= f([\mathbf{x}_{\text{PB}}]_i), \qquad \text{for } 1 \leq i, j \leq (N_\xi^t \times N_z^t) && (5.41)
\end{aligned}$$

and

$$\begin{aligned}
[\mathbf{A}_{\text{MF}}]_{ij} &= A_{\text{MF}}(\Phi_j, \Phi_i) \\
&= \langle \mathscr{L}_{\text{MF}}\Phi_j, \mathscr{L}_{\text{MF}}\Phi_i \rangle_{Y(\Omega_{\text{MF}})} + \langle \mathscr{B}_{\text{MF}}\Phi_j, \mathscr{B}_{\text{MF}}\Phi_i \rangle_{Y(\Omega_{\text{MF}})} && (5.42)\\
[\mathbf{F}_{\text{MF}}]_i &= F(\Phi_i) = \langle [\mathbf{g}_{\text{MF}}]_i, \mathscr{L}_{\text{MF}}\Phi_i \rangle_{Y(\Gamma_{\text{MF}})} + \langle [\mathbf{h}_{\text{MF}}]_i, \mathscr{B}_{\text{MF}}\Phi_i \rangle_{Y(\Gamma_{\text{MF}})} && (5.43)\\
[\mathbf{f}_{\text{MF}}]_i &= \mathbf{f}_{\text{MF}}([\mathbf{x}_{\text{MF}}]_i), \qquad \text{for } 1 \leq i, j \leq N_z^t. && (5.44)
\end{aligned}$$

5.4.3 Iteration algorithm

For the iteration algorithm, splitting strategies are usually necessary for the FVM coupled with the CFD. The PBE and flow calculations are conducted sequentially in two separate sections. Information exchange is required between these sections within each iteration.

The operator splitting of the PBE is normally applied such that its convective part is solved together with the continuity and momentum equations, while the breakage/coalescence parts are solved after the flow iteration loop is converged (see Figure 5.8). Such algorithm usually needs multiple iterative loops - one loop for calculation of flow equations combined with the convective term of the PBE (LOOP 2), which contains a nested loop for the convergence of the pressure correction equation (LOOP 1); another loop for calculation of the nonlinear PBE with the breakage and coalescence terms (LOOP 3).

Figure 5.9 illustrates the algorithm of solving the PBE with the multi-fluid model that is used in the bubble column problem of this work. It starts with two separated guessed values of unknowns $\mathbf{f}_{\text{PB}}^*(f^*)$ and $\mathbf{f}_{\text{MF}}^*(\mathbf{v}_c^*, \hat{\mathbf{v}}_d^*, P^*)$.

Since the information of the density function is known, moments of any order as well as the void fraction (α^*) and the Sauter diameter (ξ_{32}) can be calculated. Together with the

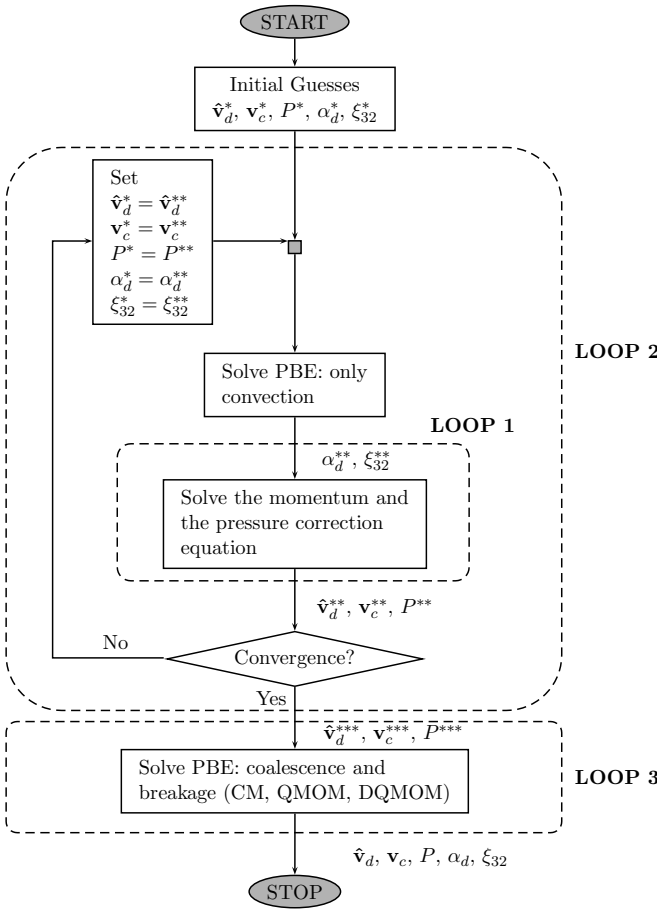

Figure 5.8: Conventional iteration algorithm for solving the PBE coupled with the two-fluid model.

guessed values being given, the PBE and multi-fluid linearized operators $\mathscr{L}_{\text{PB}}$, $\mathscr{L}_{\text{MF}}$ with their corresponding sources terms $\mathbf{g}_{\text{PB}}$ and $\mathbf{g}_{\text{MF}}$ are calculated.

The computation of the matrices $\mathbf{A}_{\text{PB}}^*$ and $\mathbf{F}_{\text{PB}}^*$, as well as $\mathbf{A}_{\text{MF}}^*$ and $\mathbf{F}_{\text{MF}}^*$ may be carried out by a least-squares method matrix constructor based on each individual problem operators. The next step is the assembly procedure. The overall stiffness matrix $\mathbf{A}^*$ and source vector $\mathbf{F}^*$ have the following structures:

$$\mathbf{A}^* = \begin{bmatrix} \mathbf{A}_{\text{PB}}^* & \mathbf{0} \\ \mathbf{0} & \mathbf{A}_{\text{MF}}^* \end{bmatrix} \quad \mathbf{F}^* = \begin{bmatrix} \mathbf{F}_{\text{PB}}^* \\ \mathbf{F}_{\text{MF}}^* \end{bmatrix} \tag{5.45}$$

in which $\mathbf{A}^*$ is the matrix constructed by diagonalizing the stiffness matrices of the PBE problem $\mathbf{A}_{\text{PB}}^*$ and the multi-fluid problem $\mathbf{A}_{\text{MF}}^*$.

Note that the prerequest of the above assembly is that both the unknowns $\mathbf{f}_{\text{PB}}^*$ and $\mathbf{f}_{\text{MF}}^*$, can be mapped to the $L_{\text{PB}}(\Omega_{\text{PB}})$ and $L_{\text{MF}}(\Omega_{\text{MF}})$ function spaces via the problem operators $\mathscr{L}_{\text{PB}}$ and $\mathscr{L}_{\text{MF}}$, respectively.

The new values of the unknowns, $\mathbf{f}^{**} = [\mathbf{f}_{\text{PB}}^{**} \quad \mathbf{f}_{\text{MF}}^{**}]^{\text{T}}$, can be obtained by inversion of the

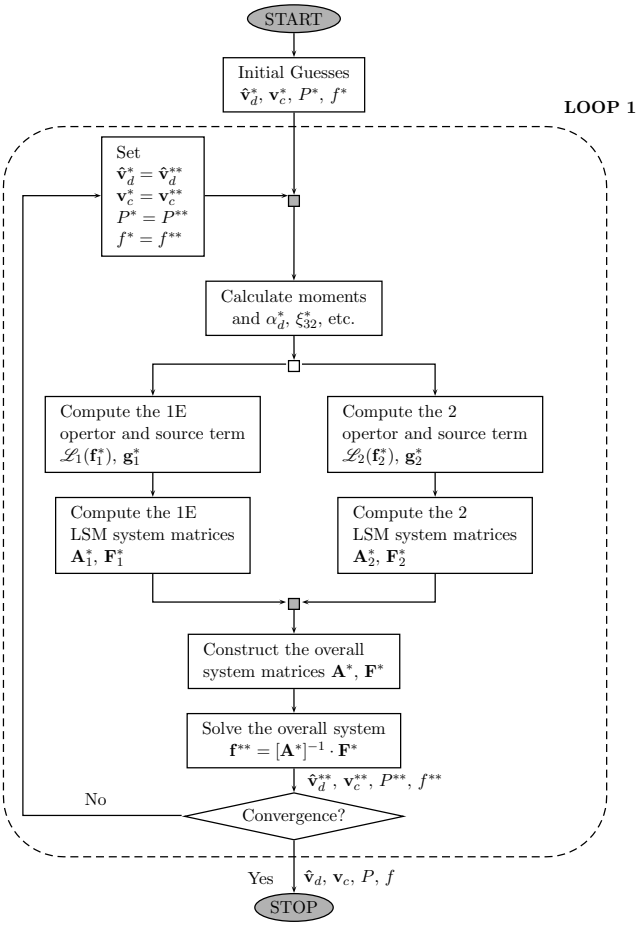

Figure 5.9: Iteration algorithm for solving the PBE coupled with two-fluid model by using the LSM.

matrix equation $\mathbf{A}^*\mathbf{f}^{**} = \mathbf{F}^*$. Then, the old values, $\mathbf{f}^*_{\text{PB}}$ and $\mathbf{f}^*_{\text{MF}}$, will be substituted by $\mathbf{f}^{**}_{\text{PB}}$ and $\mathbf{f}^{**}_{\text{MF}}$ for the next iteration until the L^2-normed residue

$$\begin{aligned} \| \mathbf{R} \|_{L^2} &= \|\mathbf{R}_{\text{PB}}\|_{L^2} + \|\mathbf{R}_{\text{MF}}\|_{L^2} \\ &\sim \max\left(\| \mathbf{R}_{\text{PB}} \|_{L^2}, \| \mathbf{R}_{\text{MF}} \|_{L^2}\right) \\ &= \max\left(\| \mathscr{L}_{\text{PB}}\mathbf{f}_{\text{PB}} - \mathbf{g}_{\text{PB}} \|_{L^2}, \| \mathscr{L}_{\text{MF}}\mathbf{f}_{\text{MF}} - \mathbf{g}_{\text{MF}} \|_{L^2}\right) \end{aligned} \tag{5.46}$$

is smaller than a specified value (10^{-6} for example) that ensures the convergence.

In comparison to the convectional approach of coupling the PBE and the flow equations, we found that solving the coupled multi-fluid model and the PBE by using the least-squares method is simpler and more systematic. Rather than conducting a decoupled iterative process, the least-squares method solves the flow equations and the population balance equation within the same framework. The least-squares approach does not split the PBE operator into convective part, and the breakage and coalescence parts are not solved in a second sequential step. Therefore, no multiple iterative loops are required. In addition, instead of solving the moments, the least-squares method solves the bubble size distribution function directly. Moments of any order can be retrieved in post-calculations by Eq.(4.29). The number of the moments does not influence the size of the system, as in QMOM. The way that the least-squares method is trying to minimize both sets of equations at the same time and searches for the optimal solution to the overall system corresponds to its intrinsic formulation Eq.(5.30).

We can see from Eq.(5.45) that the system is still not coupled in a mathematical sense, which implies that the LSM is also able to solve the PBE and the multiphase flow models separately like the case in the FVM. A fully coupled system will imply to create a common $\mathscr{L}$ operator for both parts, and then the final matrix $\mathbf{A}$ will result in a coupled system. This requires the dispersed velocity field $\mathbf{v}$ being solved in the multi-fluid model to be a function of both internal and external coordinates as in the PBE. The multi-fluid model thus has the same dimensionality as that of the PBE.

The cross-section averaged bubble column model has been implemented successfully using the LSM. The detailed simulated results and comparisons with experimental data obtained from the TOPFLOW at Forschungszentrum Dresden-Rossendorf (FZD), can be found in the self contained papers in the second part of this thesis.

Chapter 6

Conclusions and Future Work

The main contributions of this Ph.D work is the development, analysis and testing the applicability of using the least-squares method to solve the combined multifluid and PBE model that is based on the physical processes occurring in the bubble column. Different issues regarding the application of the least squares method were discussed in separate chapters in this thesis. In this chapter we shall present a brief overview of these analysis and the main conclusions. Besides, some possible lines of further research are suggested.

6.1 Conclusions

In this Ph.D work, a cross-sectional averaged two-fluid model combined with a population balance model is applied to simulate the flow field and the bubble size distributions in a two-phase bubble column. The Martinez-Bazan breakage kernel and a modified Prince and Blanch coalescence kernel have been chosen to describe bubble breakage and bubble coalescence, respectively. The solution of the combined multi-fluid model and the PBE has been found numerically by the LSM. In addition to the prediction of the gas void fraction, mean bubble diameter and moments of any order, the model has been shown to predict the evolution of the bubble size distributions, directly. With the support of the spectral elements, the LSM can find the solution in an more efficient way. The model has been validated against experimental data obtained for two-phase flow in a bubble column. The predicted bubble size distribution and other flow quantities are in good agreement with the experimental data.

The author discussed the advantages of the LSM as a solver of the stand-alone multi-fluid model, the stand-alone PBE and as a solver of multi-fluid model combined with the PBE. For the coupling of the multi-fluid model and the PBE, the LSM combines both high accuracy and efficiency. Similar to the (inhomogeneous) MUSIG, the LSM is capable of using both one-velocity and multi-velocity groups. The multi-velocity group in the LSM can be implemented by introducing subelements in the internal coordinate.

Furthermore, all interfacial mass transfer, i.e. the mass exchange of bubbles between different velocity groups, is completely handled by the PBE. The h/p-refinements within the Gauss quadrature integration in the internal coordinate provide far more effective approximation than the MUSIG. Opposite to the QMOM, moments of any order can be retrieved in post-calculations in the LSM, and the number of the desired moments does not influence the size of the system. In particular, the LSM is capable of solving the flow equations and the PBE within the same framework without introducing operator splitting and multiple iterative loops, hence an efficient and coupled scheme is obtained.

Significant loss of mass is observed when many breakage models are applied to compute the evolution of dispersed phase properties within the PBE. The mass loss problem of the dispersed phase is due to the fact that the breakup kernel does not precisely fulfill the mass conservation property. The problem is merely physical, not numerical, and does not disappear through increasing the numerical accuracy, leading to incorrect physical interpretations of the model simulations.

The author proposed a mass conservative PBE by using a LSSEM which allows for incorporating the disperse phase mass-conservation (in the form of a continuity equation for the disperse phase) by means of the Lagrange multipliers method. Then, the author solve the PBE under this additional constraint by finding the saddle point of the coupled system. Numerical experiments are carried out simulating the motion of a two-fluid model coupled with the PBE in a 2D domain. The Martinez-Bazan kernel is applied to describe the evolution of the dispersed phase. The results obtained by the constrained least-squares spectral element method show that the mass is conserved everywhere in the domain with high accuracy. The constrained LSM has significantly improved the performance of the nonconservative breakup kernels.

The results of the constrained LSM is highly desirable as the mass is conserved. Moreover, the shapes of the density functions clearly reveal that the flow is determined by the phenomena of bubble breakage. Although the enforcement of the mass conservation property is achieved at the expense of the emergence of a few large bubbles, the overall quality of the density function is quite satisfactory for the PBE. Considering that in many engineering problems the moments of the density function usually get more attention than the density function itself, the constrained LSM can be an attractive fix to these mass nonconservative breakage kernels.

However, by introducing the Lagrange multiplier one loses positive-definiteness - one of the appealing features of the LSM. A mixed problem for which one needs to establish an $\inf\text{-}\sup$ inequality is obtained. Equal order interpolation (another nice property of the LSM) is not possible anymore. Nevertheless, this mass conservative formulation of the PBE offers an attractive solution to a hitherto unsolved problem and may turn useful in engineering applications.

In this work a least-squares solver with an inherent direct minimization method (DM) is used for examining the convergence rate and the number of iterations required solving the population balance equation with different coalescence rates. The coalescence term

in the equation introduces a non-linearity that increases the complexity of the population balance equation.

It is shown that like the LSM, the DM generates the solution with high accuracy in both the breakage and coalescence dominant cases. The system with high non-linearity, large scale tends to be ill-conditioned. In comparison with the LSM, the DM has a condition number corresponding to the square root of the condition number of the system matrix of the LSM. This causes the fact that at a very high condition number, the LSM will become unstable or even fail to converge, while the DM can still get accurate results. Therefore, to solve a large scale non-linear PBE, the direct minimization method would be beneficial. Nevertheless, as mentioned in Section 2.4, the DM does not always lead to a symmetric, positive definite system. The LSM still has the advantages of handling the first-order differential equations and overdetermined systems. These are the issues need to be taken into account when deciding which method should be used in practical problems.

In addition to the major contributions mentioned above, a general purpose least-squares spectral element method toolbox lssem-suite has been designed and implemented by the author. The lssem-suite provides a highly flexible interface so that the user-defined problem operators can be easily implemented. It encapsulates the complexity of the least-squares method and makes the developing process of complex systems such as the large-scale multiphase models much faster and less error-prone.

Complex theory and implementation are the main disadvantages of the least-squares method that hinder its popularity in the CFD community. It is a relatively novel method and needs more time to be made available to engineers. At present it is regarded as a research tool. Compared to other conventional methods, for the LSM it is more difficult to define the stiffness matrix and sources. For equivalent number of the degrees of freedom, the stiffness matrix of the LSM usually has a higher condition number than other low order methods and the classic Galerkin method. For non-linear problems, computational cost is more expensive for each iterative step in the LSM, but the much fewer degrees of freedom required is a merit and reduces the overall computation. Another drawback of the LSM is stability as the linearization procedure has to be explored for every novel case (the same limitation is associated with the FVM approach, but 30-40 years experience has provided some rules of thumb).

6.2 Future work

This work presents the most complex multiphase flow model test of the LSSEM to date in our group. Nevertheless, the advantages observed so far are that the convergence rate is normally higher and better accuracy is obtained compared to the FVM solution. The present work was limited to steady, one-dimensional flow. A logical extension of the current research work could be the development of least-squares spectral element methods for the two- and three-dimensional unsteady multiphase flow equations. The efforts should be made to address more interfacial forces like lift force and virtual mass force. Emphasis

should also be laid on selecting a proper turbulence model based on the mechanisms of turbulence production and dissipation due to the interaction between the phases.

A more sophisticated case is when a non-isothermal species flow is considered, in order to gain insights of temperature profile, chemistry, conversion rate, reactive transport and so on, the heat balance equation and the chemical species balance equation are expected to be included in the model.

The assumption of incompressible gas flow fails to account for the vertical variation of bubble size due to the hydrostatic pressure change, leading to the underestimation of the void fraction in the upper part of the column. This assumption should be removed in future work by introducing an *equation of state* for the gas phase. Moreover, advanced thermodynamic models should be considered in certain processes to characterize the reaction equilibrium, phase equilibrium, non-polar/polar/ionic mixtures.

At present, the multi-fluid model incorporated with the PBE uses merely one velocity group. This assumption is necessary to reduce the gas phase momentum equations to a single equation with a velocity field, but this simplification makes the model unable to take into account the inhomogeneous properties of bubbly flow. Tomiyama et al. [89] also pointed out that the radial migrations of bubbles are different for bubbles of different sizes. Incorporation of this effect would significantly alter the gas void fraction predicted by the model. Therefore, future work should also be designed to use the multiple velocity group models, or even treat the velocity as a function of both internal and external coordinates, which is essential in real, physical multiphase flows. That is, making the gas velocity a function of particle size, space and time $\mathbf{v}(\xi, \mathbf{z}, t)$ provides a close to continuous solution of the momentum equation in all the 5 coordinates. This procedure will provide a more accurate representation than the present inhomogeneous multi-fluid model utilizing only a few velocity classes [51].

Many experimental observations show the bubble hydrodynamics (e.g., the bubble terminal velocity) are also affected by the shape of the bubbles. Hence an extra internal coordinate can be constructed so that the bubble shapes like sphere, ellipsoid and spherical-cap can be quantitatively characterized, which results in a bi-variant distribution function. Different extra internal coordinates can also be chosen for characterizing chains lengths, lumps of the polymers in polymer chemistry; different solid particle types such as catalyst, adsorbents, etc. in the fluidized bed reactor. With the model of this level of complexity, it would be extremely useful to evaluate the simulation of the dynamic 3D multifluid-PBE model of multiphase flows, and to see if the LSSEM is more efficient than the FVM for this purpose.

Further theoretical work is needed deriving consistent and more accurate population balance models, and this subject is in itself a source of large uncertainties. It is still in an initial stage of development and significant research is required developing models based on a physical understanding of the phenomena. An important and fundamental requirement of these models is that the mass conservation property should be strictly satisfied. Preliminary tests have shown that the state of the art breakage kernel needed for the PBE does

not fulfill this requirement. Experimental work and mathematical techniques like neural networks, inverse problem, parameter fitting, etc., can be utilized in order to determine the main characteristics of these functions and obtain models for practical applications.

Alternatively, the constrained LSM proposed by the author can be an attractive method to fix the nonconservative property of many existing population balance models. This method can be served as an effective remedy in applications where the composition of the system in terms of dispersed phase fraction is a key process variable. It is worthwhile to mention that the Lagrange multipliers method used to formulate the mass conservative PBE is an universal method. Further extensions might be oriented toward the implementations of the constrained PBE with different numerical methods such as CM, QMOM and DQMOM.

The multiphase reactive flow model encompass a very broad range of applications. Besides the bubble column discussed in this work, it also includes, stirred tanks with impellers, crystallization tanks, fluidized bed reactors, and perhaps even three-phase slurry bubble columns. Despite the obvious physical differences among these units, there is a similarity in the forms of the descriptive equations. Thus the consideration and procedures for constructing numerical models of these systems are also similar.

Another direction for future work could be the improvements of the present lssem-suite such as to include an iterative matrix solver and the development of mesh generation for complex geometries. Incorporation of adaptive mesh refinement based on the *posteriori* error indicator is also expected.

Bibliography

[1] S.P. Antal, R.T. Lahey, and J.E. Flaherty. Analysis of phase distribution in fully developed laminar bubbly two-phase flow. *International journal of multiphase flow*, 17(5):635–652, 1991.

[2] S.P. Antal, R.T. Lahey Jr, and M.H. Al-Dahhan. Simulating Churn-Turbulent Flows in a Bubble Column using a Three Field, Two-Fluid Model. In *5th International Conference on Multiphase Flow, ICMF'04*, 2004.

[3] M.R. Bhole, J.B. Joshi, and D. Ramkrishna. CFD simulation of bubble columns incorporating population balance modeling. *Chemical Engineering Science*, 2008.

[4] P. Bochev and MD Gunzburger. Least-squares finite-element methods for optimization and control problems for the stokes equations. *Computers and Mathematics with Applications*, 48(7-8):1035–1057, 2004.

[5] P. Bochev and M.D. Gunzburger. Least-Squares Finite Element Methods for Optimality Systems Arising in Optimization and Control Problems. *SIAM Journal on Numerical Analysis*, 43(6):2517, 2006.

[6] P.B. Bochev and M.D. Gunzburger. Finite Element Methods of Least-Squares Type. *SIAM REVIEW*, 40:789–837, 1998.

[7] P. Bolton and R.W. Thatcher. On mass conservation in least-squares methods. *Journal of Computational Physics*, 203(1):287–304, 2005.

[8] S. Bove, T. Solberg, and B.H. Hjertager. Numerical Aspects of Bubble Column Simulations. *International Journal of Chemical Reactor Engineering*, 2(A1), 2004.

[9] V.V. Buwa, D.S. Deo, and V.V. Ranade. Eulerian–Lagrangian simulations of unsteady gas–liquid flows in bubble columns. *International Journal of Multiphase Flow*, 32(7):864–885, 2006.

[10] C. Canuto. *Spectral Methods: Fundamentals in Single Domains*. Springer, 2006.

[11] P. M. Carrica, D. Drew, F. Bonetto, and R. T. Lahey Jr. A polydisperse model for bubbly two-phase flow around a surface ship. *International Journal of Multiphase Flow*, 25(2):257–305, 1999.

[12] C.L. Chang and J.J. Nelson. Least-Squares Finite Element Method for the Stokes

Problem with Zero Residual of Mass Conservation. *SIAM Journal on Numerical Analysis*, 34:480, 1997.

[13] A.J. Chorin and J.E. Marsden. *A mathematical introduction to fluid mechanics*. Springer, 1993.

[14] R. Clift, J.R. Grace, and M.E. Weber. *Bubbles, drops, and particles*. Academic press San Diego, Calif, 1978.

[15] C.A. Coulaloglou and L.L. Tavlarides. Description of interaction processes in agitated liquid-liquid dispersions. *Chem. Eng. Sci*, 32(11):1289–1297, 1977.

[16] Bart de Maerschalck. Space-time least-square spectral element method for unsteady flows - application and evaluation for linear and non-linear hyperbolic scalar eqautions. Master's thesis, Delft University of Technology, Dept. of Aerospace Engineering, 2003.

[17] W.D. Deckwer and R.W. Field. *Bubble column reactors*. Wiley New York, 1992.

[18] E. Delnoij, JAM Kuipers, and WPM van Swaaij. Computational fluid dynamics applied to gas-liquid contactors. *Chemical Engineering Science*, 52(21-22):3623–3638, 1997.

[19] E. Delnoij, FA Lammers, JAM Kuipers, and WPM van Swaaij. Dynamic simulation of dispersed gas-liquid two-phase flow using a discrete bubble model. *Chemical Engineering Science*, 52(9):1429–1458, 1997.

[20] R.B. Diemer and J.H. Olson. A moment methodology for coagulation and breakage problems: Part 3–generalized daughter distribution functions. *Chemical Engineering Science*, 57(19):4187–4198, 2002.

[21] C.A. Dorao and H.A. Jakobsen. A least squares method for the solution of population balance problems. *Computers & Chemical Engineering*, 30(3):535–547, 2006.

[22] C.A. Dorao and H.A. Jakobsen. Numerical calculation of the moments of the population balance equation. *Journal of Computational and Applied Mathematics*, 196(2):619–633, 2006.

[23] C.A. Dorao and H.A. Jakobsen. The quadrature method of moments and its relationship with the method of weighted residuals. *Chemical Engineering Science*, 61(23):7795–7804, 2006.

[24] C.A. Dorao and H.A. Jakobsen. Least-squares spectral method for solving advective population balance problems. *Journal of Computational and Applied Mathematics*, 201(1):247–257, 2007.

[25] C.A. Dorao and H.A. Jakobsen. Time–space-property least squares spectral method for population balance problems. *Chemical Engineering Science*, 62(5):1323–1333, 2007.

[26] D.A. Drew. Mathematical modeling of two-phase flow. *Annual Review of Fluid Mechanics*, 15:261–291, 1983.

[27] D.A. Drew and S.L. Passman. *Theory of multicomponent fluids*. Springer New York, 1999.

[28] R. Fan, D.L. Marchisio, and R.O. Fox. Application of the direct quadrature method of moments to polydisperse gas–solid fluidized beds. *Powder Technology*, 139(1):7–20, 2004.

[29] J.H. Ferziger and M. Perić. *Computational methods for fluid dynamics*. Springer New York, 2002.

[30] A. Clausse G. Guido-Lavalle and J. Converti. A contribution to a kinetic formulation of two-phase flows. *Chem. Eng. Commun.*, 120, 1994.

[31] Á. Galvão, M. Gerritsma, and B. De Maerschalck. hp-Adaptive least squares spectral element method for hyperbolic partial differential equations. *Journal of Computational and Applied Mathematics*, 215(2):409–418, 2008.

[32] W. Gautschi. Algorithm 726: Orthpol - a package of routines for generating orthogonal polynomials and gauss-type quadrature rules. *ACM Transactions on Mathematical Software*, 20:21–62, 1994.

[33] G.H. Golub and J.H. Welsch. Calculation of gauss quadrature rules. *Mathematics of Computation*, 23(106), 1969.

[34] R.G. Gordon. Error bounds in equilibrium statistical mechanics. *Journal of Mathematical Physics*, 9:655, 1968.

[35] T. Hibiki and M. Ishii. Two-group interfacial area transport equations at bubbly-to-slug flow transition. *Nuclear Engineering and Design*, 202(1):39–76, 2000.

[36] T. Hibiki, M. Ishii, and Z. Xiao. Axial interfacial area transport of vertical bubbly flows. *International Journal of Heat and Mass Transfer*, 44(10):1869–1888, 2001.

[37] W. Hoitinga, R. de Groot, M. Kwakkel, and M. Gerritsma. Direct Minimization of the least-squares spectral element functional–Part I: Direct solver. *Journal of Computational Physics*, 227(4):2411–2429, 2008.

[38] M.J. Hounslow. A discretized population balance for continuous systems at steady state. *AIChE Journal*, 36(1), 1990.

[39] M.J. Hounslow, R.L. Ryall, and V.R. Marshall. A discretized population balance for nucleation, growth, and aggregation. *AIChE journal*, 34(11):1821–1832, 1988.

[40] HM Hulburt and S. Katz. Some problems in particle technology. A statistical mechanical formulation. *Chem. Eng. Sci*, 19:555–574, 1964.

[41] M. Ishii and K. Mishima. Two-fluid model and hydrodynamic constitutive relations. *Nuclear engineering and design*, 82(2-3):107–126, 1984.

[42] M. Ishii, X. Sun, and S. Kim. Modeling strategy of the source and sink terms in the two-group interfacial area transport equation. *Annals of Nuclear Energy*, 30(13):1309–1331, 2003.

[43] H.A. Jakobsen. *Chemical Reactor Modeling: Multiphase Reactive Flows*. Springer Verlag, 2008.

[44] H.A. Jakobsen, H. Lindborg, and C.A. Dorao. Modeling of bubble column reactors: Progress and limitations. *Industrial & Engineering Chemistry Research*, 44:5107–5151, 2005.

[45] H.A. Jakobsen, B.H. Sannaes, S. Grevskott, and H.F. Svendsen. Modeling of vertical bubble-driven flows. *Ind. Eng. Chem. Res*, 36(10):4052–4074, 1997.

[46] B. Jiang. The Least-Squares Finite Element Method: Theory and Applications in Computational Fluid Dynamics and Electromagnetics. 1998.

[47] G. Karniadakis and S.J. Sherwin. *Spectral/hp element methods for CFD*. Oxford University Press New York, 1999.

[48] S. Kim, X. Sun, M. Ishii, S.G. Beus, and F. Lincoln. Interfacial area transport and evaluation of source and sink terms for confined air–water bubbly flow. *Nuclear Engineering and Design*, 219(1):61–75, 2003.

[49] G. Kocamustafaogullari and M. Ishii. Foundation of the interfacial area transport equation and its closure relations. *International Journal of Heat and Mass Transfer*, 38(3):481–494, 1995.

[50] M. Konno, M. Aoki, and S. Saito. Scale effect on breakup process in liquid-liquid agitated tanks. *Journal of chemical engineering of Japan*, 16(4):312–319, 1983.

[51] E. Krepper, D. Lucas, T. Frank, H.M. Prasser, and P.J. Zwart. The inhomogeneous MUSIG model for the simulation of polydispersed flows. *Nuclear Engineering and Design*, 2008.

[52] E. Krepper, D. Lucas, and H.M. Prasser. On the modelling of bubbly flow in vertical pipes. *Nuclear Engineering and Design*, 235(5):597–611, 2005.

[53] S. Kumar and D. Ramkrishna. On the solution of population balance equations by discretization-I. A fixed pivot technique. *Chemical Engineering Science*, 51(8):1311–1332, 1996.

[54] Marcel Kwakkel and Marc Gerritsma. Time dependent flow simulation using least squares spectral element method in combination with direct minimization. In *European Conference on Computational Fluid Dynamics, ECCOMAS CFD 2006*, 2006.

[55] D. L. Marchisio, R. Dennis Vigil, and R. O. Fox. Implementation of the quadrature method of moments in CFD codes for aggregation–breakage problems. *Chemical Engineering Science*, 58(15):3337–3351, 2003.

[56] A.Y. Lafi and J.N. Reyes Jr. General particle transport equation. Final report. *United States*, 1994.

[57] R.T. Lahey and D.A. Drew. The analysis of two-phase flow and heat transfer using a multidimensional, four field, two-fluid model. *Nuclear Engineering and Design*, 204(1-3):29–44, 2001.

[58] P. Lambin and J.P. Gaspard. Continued-fraction technique for tight-binding systems. A generalized-moments method. *Physical Review B*, 26(8):4356–4368, 1982.

[59] J.C. Lasheras, C. Eastwood, C. Martinez-Bazán, and J.L. Montañés. A review of statistical models for the break-up of an immiscible fluid immersed into a fully developed turbulent flow. *International Journal of Multiphase Flow*, 28(2):247–278, 2002.

[60] T.J. Lin, J. Reese, T. Hong, and L.S. Fan. Quantitative analysis and computation of two-dimensional bubble columns. *AIChE Journal*, 42(2), 1996.

[61] S. Lo. Application of population balance to CFD modelling of bubbly flow via the MUSIG model. *AEA Technology, AEAT-1096*, 1996.

[62] S. Lo. Application of population balance to CFD modelling of gas-liquid reactors. In *Proceeding of conference on Trends in Numerical and Physical Modelling for Industrial Multiphase Flows Conference, Corse, France*, 2000.

[63] B.D. Maerschalck and M.I. Gerritsma. Higher-order Gauss–Lobatto integration for non-linear hyperbolic equations. *Journal of Scientific Computing*, 27(1):201–214, 2006.

[64] E. Manger. *Modelling and simulation of gas/solids flow in curvilinear coordinates*. Høgskolen i Telemark, Avdeling for teknologiske fag, Institutt for prosessteknologi, 1996.

[65] D.L. Marchisio and R.O. Fox. Solution of population balance equations using the direct quadrature method of moments. *Journal of Aerosol Science*, 36(1):43–73, 2005.

[66] D.L. Marchisio, J.T. Pikturna, R.O. Fox, R.D. Vigil, and A.A. Barresi. Quadrature method of moments for population-balance equations. *AIChE Journal*, 49(5):1266–1276, 2003.

[67] D.L. Marchisio, R.D. Vigil, and R.O. Fox. Quadrature method of moments for aggregation–breakage processes. *Journal of colloid and interface science*, 258(2):322–334, 2003.

[68] R. McGraw. Description of aerosol dynamics by the quadrature method of moments. *Aerosol Science and Technology*, 27(2):255–265, 1997.

[69] Robert McGraw, Seth Nemesure, and Stephen E. Schwartz. Properties and evo-

lution of aerosols with size distributions having identical moments. *Journal of Aerosol Science*, 29(7):761–772, 1998.

[70] T.F. Miller and D.J. Miller. A Fourier analysis of the IPSA/PEA algorithms applied to multiphase flows with mass transfer. *Computers and Fluids*, 32(2):197–221, 2003.

[71] C. Morel, N. Goreaud, and J.M. Delhaye. The local volumetric interfacial area transport equation: derivation and physical significance. *International Journal of Multiphase Flow*, 25(6-7):1099–1128, 1999.

[72] Y. Pan and M.P. Dudukovic. Mean axial liquid velocity profile in bubble columns – numerical versus carpt. In *CREL Annual meeting*, 2000.

[73] S.V. Patankar and D.B. Spalding. A calculation procedure for heat, mass and momentum transfer in three-dimensional parabolic flows. *Int. J. Heat Mass Transfer*, 15(10):1787–1806, 1972.

[74] D. Pfleger and S. Becker. Modelling and simulation of the dynamic flow behaviour in a bubble column. *Chemical Engineering Science*, 56(4):1737–1747, 2001.

[75] J.P. Pontaza and J.N. Reddy. Spectral/hp least-squares finite element formulation for the Navier-Stokes equations. *Journal of Computational Physics*, 190(2):523–549, 2003.

[76] M.M.J. Proot and M.I. Gerritsma. Least-Squares Spectral Elements Applied to the Stokes Problem. *Journal of Computational Physics*, 181(2):454–477, 2002.

[77] M.M.J. Proot and M.I. Gerritsma. Mass-and Momentum Conservation of the Least-Squares Spectral Element Method for the Stokes Problem. *Journal of Scientific Computing*, 27(1):389–401, 2006.

[78] D. Ramkrishna. The status of population balances. *Rev. Chem. Eng.*, 3:49, 1985.

[79] D. Ramkrishna. *Population Balances, Theory and Applications to Particulate Systems in Engineering*. Academic Press, San Diego, 2000.

[80] A.D. Randolph. A population balance for countable entities. *Can. J. Chem. Eng.*, 42:280, 1964.

[81] J.N. Reyes. Statistically derived conservation equations for fluid particle flows. *Transactions of the American Nuclear Society*, 60, 1989.

[82] J. Sanyal, D.L. Marchisio, R.O. Fox, and K. Dhanasekharan. On the comparison between population balance models for CFD simulation of bubble columns. *Ind Eng Chem Res*, 44(4):5–063, 2005.

[83] Y.T. Shah, B.G. Kelkar, S.P. Godbole, and W.D. Deckwer. Design parameters estimations for bubble column reactors. volume 28, pages 353–379. American Institute of Chemical Engineers New York, 1982.

[84] J.C. Slattery. *Advanced Transport Phenomena*. Cambridge University Press, 1999.

[85] A. Sokolichin and G. Eigenberger. Gas-liquid flow in bubble columns and loop reactors: part i. detailed modelling and numerical simulation. *Chemical Engineering Sciences*, 49(24):5735–5746, 1994.

[86] D. Spalding. Numerical computation of multiphase flow and heat transfer, Recent advances in numerical methods in fluid mechanics. *Taylor and K. Morton eds., Pineridge, Swansea*, pages 139–168, 1980.

[87] X. Sun, S. Kim, M. Ishii, and S.G. Beus. Modeling of bubble coalescence and disintegration in confined upward two-phase flow. *Nuclear Engineering and Design*, 230(1-3):3–26, 2004.

[88] A. Tomiyama. Struggle with computational bubble dynamics. In *Third International Conference on Multiphase Flow*, volume 98, pages 8–12, Lyon, France, 1998.

[89] A. Tomiyama, H. Tamai, I. Zun, and S. Hosokawa. Transverse migration of single bubbles in simple shear flows. *Chemical Engineering Science*, 57(11):1849–1858, 2002.

[90] S.O. Unverdi and G. Tryggvason. A front-tracking method for viscous, incompressible, multi-fluid flows. *Journal of Computational Physics*, 100(1):25–37, 1992.

[91] K.J. Valentas and N.R. Amundson. Breakage and coalescence in dispersed phase systems. 2002.

[92] H.K. Versteeg and W. Malalasekera. *An introduction to computational fluid dynamics*. Prentice Hall, 1995.

[93] L. Wang, D.L. Marchisio, R.D. Vigil, and R.O. Fox. CFD simulation of aggregation and breakage processes in laminar Taylor–Couette flow. *Journal of colloid and interface science*, 282(2):380–396, 2005.

[94] L. Wang, R.D. Vigil, and R.O. Fox. CFD simulation of shear-induced aggregation and breakage in turbulent Taylor–Couette flow. *Journal of colloid and interface science*, 285(1):167–178, 2005.

[95] D.L. Wright, R. McGraw, and D.E. Rosner. Bivariate extension of the quadrature method of moments for modeling simultaneous coagulation and sintering of particle populations. *Journal of colloid and interface science*, 236(2):242–251, 2001.

[96] Q. Wu, S. Kim, M. Ishii, and S.G. Beus. One-group interfacial area transport in vertical bubbly flow. *International Journal of Heat and Mass Transfer*, 41:1103–1112, 1998.

[97] D.W. Yin, A.D. Burns, B.A. Splawski, S.M. Lo, and C. Guetari. Modeling of

complex multiphase flows: A coupled solver approach. In *Fourth International Conference on Multiphase Flow*, volume 119, 2001.

[98] C. Yoon and R. McGraw. Representation of generally mixed multivariate aerosols by the quadrature method of moments: I. Statistical foundation. *Journal of Aerosol Science*, 35(5):561–576, 2004.

[99] C. Yoon and R. McGraw. Representation of generally mixed multivariate aerosols by the quadrature method of moments: II. Aerosol dynamics. *Journal of Aerosol Science*, 35(5):577–598, 2004.

[100] A. Zaccone, A. Gäbler, S. Maaß, D. Marchisio, and M. Kraume. Drop breakage in liquid–liquid stirred dispersions: Modelling of single drop breakage. *Chemical Engineering Science*, 62(22):6297–6307, 2007.

[101] Z. Zhu, C.A. Dorao, and H.A. Jakobsen. A least-squares method with direct minimization for the solution of the breakage–coalescence population balance equation. *Mathematics and Computers in Simulation*, 79(3):716–727, 2008.

Appendix A

Spectral Element Approximation in $\mathbb{R}^n$

A.1 Spectral element in one-dimension

The problem domain Ω can be divided into N_e subdomains $(\Omega_1, \Omega_2, \ldots, \Omega_{N_e})$ in order to achieve better numerical efficiency. Therefore, we have

$$\Omega = \bigcup_{e=1}^{N_e} \Omega_e. \tag{A.1}$$

It is possible to express the global modes $\phi_J(x)$ in terms of the local expansion modes $\phi_j^e(x)$. Therefore, we can express local expansion of unknowns f_N in terms of $\phi_j^e(x)$, that is,

$$f_N(x) = \sum_{J=1}^{N} f_J \phi_J(x) = \sum_{e=1}^{N_e} \sum_{j=1}^{N_m^e+1} f_j^e \phi_j^e(x), \tag{A.2}$$

Suppose a one-dimensional domain Ω is divided into three linear elements, called Ω_1, Ω_2 and Ω_3, numbered from left to right as shown in Figure A.1. The nodes have the coordinates x_1, x_2, x_3 and x_4 and the constraint is that the global modes are continuous everywhere, which implies

$$f_2^1 = f_1^2 \tag{A.3}$$
$$f_2^2 = f_1^3 \tag{A.4}$$

The relationship between the local and global expansion coefficient is

$$\begin{aligned} f_1^1 &= f_1 \\ f_2^1 = f_1^2 &= f_2 \\ f_2^2 = f_1^3 &= f_3 \\ f_2^3 &= f_4 \end{aligned}$$

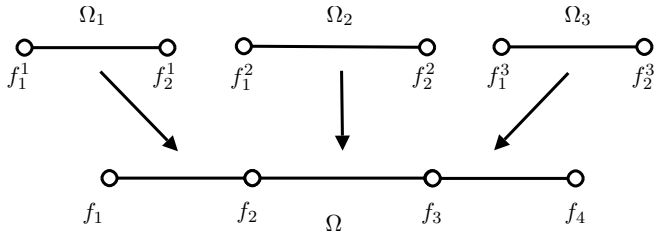

Figure A.1: One-dimensional domain divided into three subdomains with linear polynomial expansion.

For this example it can be seen that the local representation of the function has totally six elemental degrees of freedom ($N_{dof} = N_e(N_m^e + 1) = 6$) but only four global degrees of freedom ($N = 4$). The two constraints shown in (A.3) and (A.4) ensures that $f_N(x)$ is C^0 continuous. As a result, there are more local expansion coefficients f_j^e than global expansion coefficients f_J

A general procedure for global assembling is to construct a mapping array $\mathcal{GM}$ called the *local-global mapping* matrix. $\mathcal{GM}$ is a $N_e \times (N_x^e + 1)$ matrix where the e–th row contains in a fixed order the indices of the global expansion coefficients of the e–th subdomain. N_m^e is called the elemental degree of freedom.

$$\mathcal{GM} = \begin{bmatrix} 1 & 2 \\ 2 & 3 \\ 3 & 4 \end{bmatrix} \tag{A.5}$$

The scatter operation can then be evaluated as

$$\begin{aligned} &\textbf{for } e = 1 \rightarrow N_e \\ &\quad \textbf{for } j = 1 \rightarrow N_x^e \\ &\qquad \mathbf{f}_j^e = [\mathbf{f}_g]_{\mathcal{GM}_{ej}} \\ &\quad \textbf{end} \\ &\textbf{end} \end{aligned} \tag{A.6}$$

Alternatively, the global assembly may be written as

$$\begin{aligned} &\textbf{for } e = 1 \rightarrow N_e \\ &\quad \textbf{for } j = 1 \rightarrow N_x^e \\ &\qquad [\mathbf{f}_g]_{\mathcal{GM}_{ej}} = \mathbf{f}_j^e \\ &\quad \textbf{end} \\ &\textbf{end} \end{aligned} \tag{A.7}$$

Each spectral element is first mapped on the reference element and then the local systems

$$\mathbf{A}_e \mathbf{f}^e = \mathbf{g}_e, \quad \text{with } e = 1, \cdots, N_e \tag{A.8}$$

are calculated. The matrix $\mathbf{A}_e$ represents the least-squares spectral element discretization of the governing equations of spectral element e, and the vectors $\mathbf{f}^e$ and $\mathbf{g}_e$ represent the corresponding local variables and the right-hand function, respectively.

The local-global mapping matrices $\mathcal{GM}$ can also be expressed by the sparse *gathering matrix* $\mathcal{G}_e$ which has nonzero entries. The global assembly of the N_e local systems (A.8) can now readily be obtained with:

$$\mathbf{A}\mathbf{f}_g = \mathbf{g} \Longleftrightarrow \left[\sum_{e=1}^{N_e} \mathcal{G}_e^{\mathrm{T}} \mathbf{A}_e \mathcal{G}_e\right] \mathbf{f}_g = \sum_{e=1}^{N_e} \mathcal{G}_e^{\mathrm{T}} \mathbf{g} \tag{A.9}$$

in which,

$$\mathcal{G}_1 = \begin{bmatrix} 1 & 0 & 0 & 0 \\ 0 & 1 & 0 & 0 \end{bmatrix} \quad \mathcal{G}_2 = \begin{bmatrix} 0 & 1 & 0 & 0 \\ 0 & 0 & 1 & 0 \end{bmatrix} \quad \mathcal{G}_3 = \begin{bmatrix} 0 & 0 & 1 & 0 \\ 0 & 0 & 0 & 1 \end{bmatrix}. \tag{A.10}$$

The row number of the *gathering matrix* equals to the local degree of freedom in a subelement, and its column number equals to the global degree of freedom. The *gathering matrix* contains information of a single subdomain with each of its local node is marked by a unit value. The row number of this unit value is the *local index* and the column number is the *global index*.

The local systems:

$$\underbrace{\begin{bmatrix} a_{11}^1 & a_{12}^1 \\ a_{21}^1 & a_{22}^1 \end{bmatrix}}_{\mathbf{A}_1} \underbrace{\begin{bmatrix} f_1^1 \\ f_2^1 \end{bmatrix}}_{\mathbf{f}^1} = \underbrace{\begin{bmatrix} g_1^1 \\ g_2^1 \end{bmatrix}}_{\mathbf{g}_1}$$

$$\underbrace{\begin{bmatrix} a_{11}^2 & a_{12}^2 \\ a_{21}^2 & a_{22}^2 \end{bmatrix}}_{\mathbf{A}_2} \underbrace{\begin{bmatrix} f_1^2 \\ f_2^2 \end{bmatrix}}_{\mathbf{f}^2} = \underbrace{\begin{bmatrix} g_1^2 \\ g_2^2 \end{bmatrix}}_{\mathbf{g}_2}$$

$$\underbrace{\begin{bmatrix} a_{11}^3 & a_{12}^3 \\ a_{21}^3 & a_{22}^3 \end{bmatrix}}_{\mathbf{A}_3} \underbrace{\begin{bmatrix} f_1^3 \\ f_2^3 \end{bmatrix}}_{\mathbf{f}^3} = \underbrace{\begin{bmatrix} g_1^3 \\ g_2^3 \end{bmatrix}}_{\mathbf{g}_3}$$

The global system:

$$\underbrace{\begin{bmatrix} a_{11}^1 & a_{12}^1 & 0 & 0 \\ a_{21}^1 & a_{22}^1 + a_{11}^2 & a_{12}^2 & 0 \\ 0 & a_{21}^2 & a_{22}^2 + a_{11}^3 & a_{12}^3 \\ 0 & 0 & a_{21}^3 & a_{22}^3 \end{bmatrix}}_{\mathbf{A}} \underbrace{\begin{bmatrix} f_1 \\ f_2 \\ f_3 \\ f_4 \end{bmatrix}}_{\mathbf{f}_g} = \underbrace{\begin{bmatrix} g_1^1 \\ g_2^1 + g_1^2 \\ g_2^2 + g_1^3 \\ g_1^3 \end{bmatrix}}_{\mathbf{g}}$$

Figure A.2: The structures of local and global systems in the spectral element approaches of the LSM.

The structures of the local systems and assembled global system can be viewed in Figure A.2. It can be seen that the local expansion coefficients of overlapping boundary points exist within two adjacent local systems. Values at corresponding positions of the global

stiffness matrix $\mathbf{A}$ and load vector $\mathbf{g}$ are evaluated as the summations of values from the two adjacent local systems. It is worthwhile to mention that N_x^e can be greater than 1 and it is not necessary that N_x^e in each subdomain must be equal. In such case, the global $\mathcal{GM}$ is a more complex data type other than the matrix in (A.5).

A.2 Spectral element in multi-dimension

Suppose a two-dimensional domain Ω is divided into four spectral elements, called Ω_1, Ω_2, Ω_3 and Ω_4, numbered from left to right and bottom to top as shown in Figure A.3.

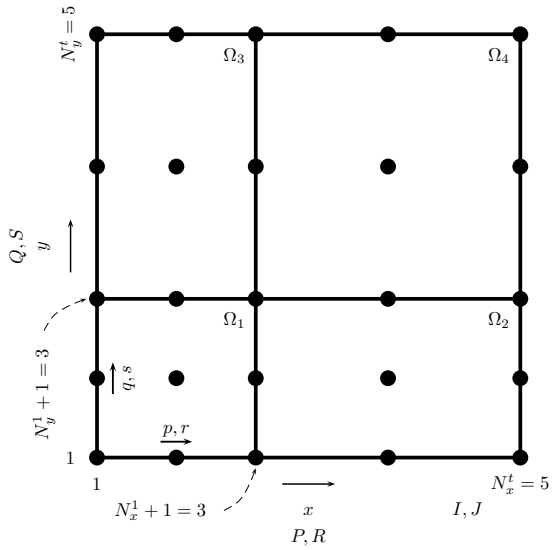

Figure A.3: The index system on a two-dimensional spectral element domain that is divided into four subdomains.

For the two-dimensional spectral element problem, we introduce two sets of numbering system, *local numbering* and *global numbering*.

The local numbering system is with respect to the individual subelement. Each node in the subelement can be identified by two integer numbers called *local subscripts*. These *local subscripts* are number from left to right in the x-direction and from bottom to top in the y-direction.

As being written in subelement Ω_1 in Figure A.3, the *local subscripts* p and q to denote the location of the GLL points for x and y, while another set of *local subscripts* r and s represent the degree of freedom for x and y in each subelement.

Alternatively, locations of local GLL point can also be identified by a single number called *local index*. The *local subscripts* (p, q, r and s) can be equivalently substituted by *local*

indices i and j through the following transformation.

$$i = (q-1) \times (N_y^e + 1) + p, \quad 1 \leq p \leq (N_x^e + 1) \text{ and } 1 \leq q \leq (N_y^e + 1) \tag{A.11}$$

$$j = (s-1) \times (N_y^e + 1) + r, \quad 1 \leq r \leq (N_x^e + 1) \text{ and } 1 \leq s \leq (N_y^e + 1) \tag{A.12}$$

in which N_x^e and N_y^e are the 1D polynomial degree of the basis functions in x and y-direction, respectively.

The inverse transformations that convert from *local indices* to *local subscripts* are

$$q = \mathsf{floor}\left(\frac{i}{N_y^e + 1}\right) + 1, \qquad p = i - (p-1) \times (N_y^e + 1); \tag{A.13}$$

$$s = \mathsf{floor}\left(\frac{j}{N_y^e + 1}\right) + 1, \qquad r = j - (r-1) \times (N_y^e + 1). \tag{A.14}$$

Here floor is a function that rounds towards negative infinity.

Similarly in the global domain, a *global numbering* system is used to uniquely denote the location of each GLL point. In our notion we use the capital letters to represent the *global numbering* in order to differentiate from the *local numbering*.

We can write transformation between the *global subscripts* (P, Q, R and S) and *global indices* (I and J) by resembling of the local transformations

$$I = (Q-1) \times N_y^t + P, \quad 1 \leq P \leq N_x^t \text{ and } 1 \leq Q \leq N_y^t \tag{A.15}$$

$$J = (S-1) \times N_y^t + R, \quad 1 \leq R \leq N_x^t \text{ and } 1 \leq S \leq N_y^t. \tag{A.16}$$

and the inverse transformations

$$Q = \mathsf{floor}\left(I/N_y^t\right) + 1, \qquad P = I - (P-1) \times N_y^t; \tag{A.17}$$

$$S = \mathsf{floor}\left(J/N_y^t\right) + 1, \qquad R = J - (R-1) \times N_y^t. \tag{A.18}$$

in which, N_y^t and N_x^t are the global degree of freedom in y and x, respectively.

The nodes in the 2D domain have their *local indices* shown in Figure A.4 (a) and the *global indices* shown in Figure A.4 (b), respectively. Indices (including the *local indices* and *global indices*) are necessary to construct the local and global stiffness matrices $\mathbf{A}_e$ and $\mathbf{A}$, respectively. The reason that we introduce the concept of *subscript* is that it stores the information of GLL positions in each dimension, which makes values of the Lagrangian polynomials readily to construct the least-squares problem operator $\mathscr{L}$.

Now we can use the *global indices* to approximate the $f_N(x, y)$ in terms of *local indices*, that is

$$f_N(x,y) = \sum_{J=1}^{N_y^t \times N_x^t} f_J \Phi_J(x,y) = \sum_{e=1}^{N_e} \sum_{j=1}^{(N_y^e+1)\times(N_x^e+1)} f_j^e \Phi_j^e(x,y) \tag{A.19}$$

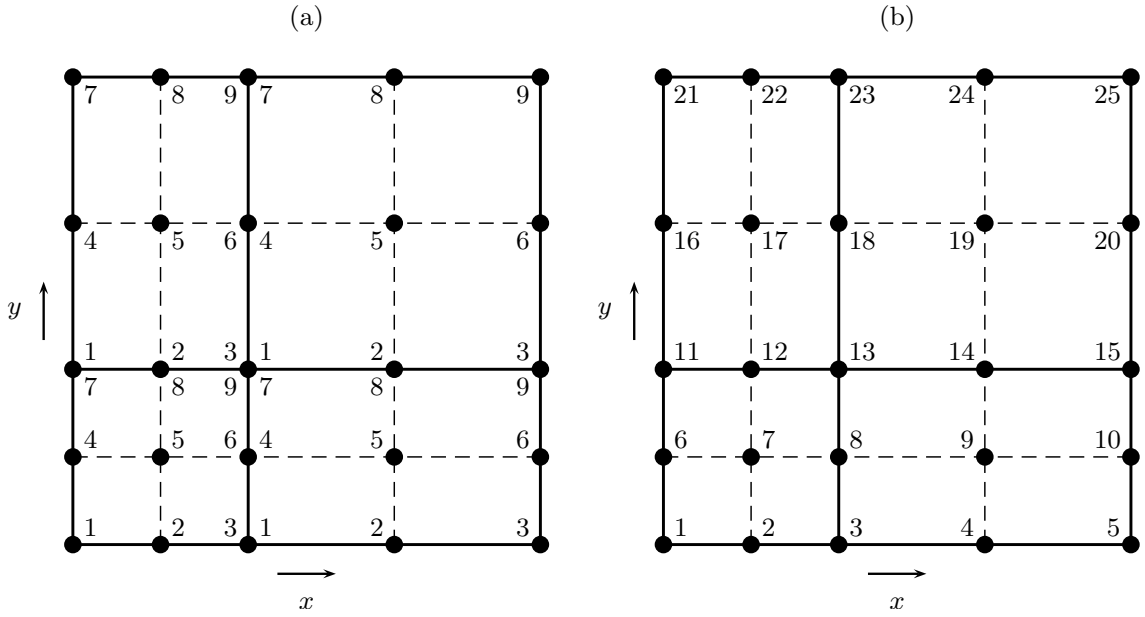

Figure A.4: The *local indices* (a) and *global indices* (b) of GLL points on a two-dimensional physical domain that is divided into four subdomains.

in which

$$\Phi_j^e(x,y) = \phi_r^e(x)\phi_s^e(y)$$

As it can be seen there are more local expansion coefficients f_j^e than global expansion coefficients f_J, some extra constraints are required. The constraint is that the approximation is continuous everywhere, which implies for example

$$f_3^1 = f_1^2 \tag{A.20}$$
$$f_7^1 = f_1^3 \tag{A.21}$$
$$f_9^1 = f_1^4 \tag{A.22}$$

The relationship between the local and global expansion coefficient on subdomain Ω_1 is

$$\begin{aligned} f_1^1 &= f_1 \\ f_3^1 = f_1^2 &= f_3 \\ f_7^1 = f_1^3 &= f_{11} \\ f_9^1 = f_7^2 = f_3^3 = f_1^4 &= f_{13} \end{aligned}$$

For this example it can be seen that the local representation of the function has totally 36 elemental degrees of freedom ($N_{dof} = N_e \sum_{e=1}^{N_e}[(N_x^e+1)\times(N_y^e+1)] = 36$, see Figure A.4(a)) but only 25 global degrees of freedom ($N_{dof}^t = N_x^t \times N_y^t = 25$, see Figure A.4(b)).

The constraints such as (A.20), (A.21) and (A.22) ensure that $f_N(x, y)$ is C^0 continuous [1] across the subelement boundaries.

As in the one-dimensional spectral element approach, a general procedure for global assembling is to construct two *local-global mapping* matrices $\mathcal{GM}_x$ and $\mathcal{GM}_y$.

$\mathcal{GM}_x$ is a $N_{e_x} \times (N_x^e + 1)$ matrix where the e_x–th row contains in a fixed order the *global subscripts* of the global expansion coefficients of the e_x-th subdomain in x-direction. N_{e_x} is number of subdomains in x-direction. $\mathcal{GM}_y$ is a $N_{e_y} \times (N_y^e + 1)$ matrix where the e_y–th row contains in a fixed order the *global subscripts* of the global expansion coefficients of the e_y-th subdomain in y-direction. N_{e_y} is number of subdomains in y-direction. The elemental index e can be represented by elemental subscripts e_y and e_x by following expression

$$e = (e_y - 1) \times N_{e_x} + e_x \tag{A.23}$$

For our example the $\mathcal{GM}_y$ and $\mathcal{GM}_x$ are

$$\mathcal{GM}_y = \begin{bmatrix} 1 & 2 & 3 \\ 3 & 4 & 5 \end{bmatrix} \qquad \mathcal{GM}_x = \begin{bmatrix} 1 & 2 & 3 \\ 3 & 4 & 5 \end{bmatrix} \tag{A.24}$$

Therefore, the *global subscripts* can be expressed by the *local subscripts*,

$$P = [\mathcal{GM}_x]_{e_x,p} \tag{A.25}$$
$$Q = [\mathcal{GM}_y]_{e_y,q} \tag{A.26}$$
$$R = [\mathcal{GM}_x]_{e_x,r} \tag{A.27}$$
$$S = [\mathcal{GM}_y]_{e_y,s}. \tag{A.28}$$

By using Eqs. (A.13), (A.14), (A.15), (A.16), (A.25), (A.26), (A.27) and (A.28), the scattering operation that convert the local expansion coefficients to the global expansion coefficients can thus be evaluated as

for $e = 1$ **to** N_e
  for $j = 1$ **to** $(N_y^e + 1) \times (N_x^e + 1)$
    $j \xrightarrow{\text{(A.14)}} r,\ s$
    $r,\ s \xrightarrow{\text{(A.27) and (A.28)}} R,\ S$
    $R,\ S \xrightarrow{\text{(A.16)}} J$
    $\mathbf{f}_j^e = [\mathbf{f}_g]_J$
  end
end

Alternatively, the global assembly may be written as

[1] C^0 continuity means the approximated curve points vary smoothly. That is, the curve is a set of connected points. C^1 continuity means the curve's first derivatives vary smoothly (plus C^0 continuity).

for $e = 1$ **to** N_e
  for $j = 1$ **to** $(N_y^e + 1) \times (N_x^e + 1)$
    $j \xrightarrow{\text{(A.14)}} r,\ s$
    $r,\ s \xrightarrow{\text{(A.27) and (A.28)}} R,\ S$
    $R,\ S \xrightarrow{\text{(A.16)}} J$
    $[\mathbf{f}_g]_J = [\mathbf{f}_g]_J + \mathbf{f}_j^e$
  end
end

in which, $\mathbf{f}_g$ and $\mathbf{f}^e$ are arrays of the global and local expansion coefficients, respectively.

Appendix B

A Generic LSSEM Toolbox - lssem-suite

B.1 Introduction

During the present work, the author has developed a generic least-squares spectral element method toolbox, lssem-suite. The lssem-suite is a computer program written in Matlab to solve PDEs using the least-squares spectral element method.

The lssem-suite takes the advantages of the high-level scripting language, and uses advanced data structures which allow an easy and efficient implementation of the problem dependent parts and mesh generation algorithms. A specific problem can be implemented and solved by providing just some problem dependent routines for evaluation of the (linearized) differential operator and source terms.

The lssem-suite consists of four general purpose solvers; linearlssemoneproblem.m, nonlinearlssemoneproblem.m, linearlssemmulti-problem.m and nonlinearlssemmulti-problem.m. There functions provide the capabilities of resolving both linear and nonlinear systems, as well as both single PDE problem and multiple PDE problem. The features of the lssem-suite are summarized as follows:

- Technique for solving the PDE: The least-squares method.
- Number of space dimensions: Indefinite (only limited by the capacity of computer memory). The data structures used in the codes, which dynamically allocate/deallocate the memory as the computation proceeds, allows easy extensions to higher dimensions. The space specifications can be formulated in such a way that the dimension is entered as a parameter (e.g. like size of local coordinate vectors)
- Number of variables: Indefinite (only limited by the capacity of computer memory). The lssem-suite is suitable for problems with infinite number of variables defined in the prescribed domain.

- Number of PDE problems: Indefinite (only limited by the capacity of computer memory). Based on the intrinsic property of the least-squares method, the lssem-suite allows problems defined in different spaces to be solved within the same framework.
- The h/p-refinements: The h/p spectral element method, in which both grid size h and local polynomial order p are altered, is a very effective discretization scheme for the numerical solution of large scale partial differential equations. The lssem-suite is equipped with the grid specification with both local h-refinement and p-enrichment, while different local function spaces can be used on all subgrid elements.
- Higher-order integration: In order for the least-squares spectral element method to make sense, the number of the Gaussian quadrature points must be equal to or greater than the number of the Lagrangian polynomials order. In particular, it is reported that higher order integration is used in the hyperbolic type differential equations [16]. The lssem-suite allows both equal order and higher-order integration.
- Iteration method: Picard iteration, by which the general nonlinear discrete systems be solved.
- The codes are written in MatLab (Version 7.2.0.294) and can be run under both Windows and Linux platforms.

B.2 Code design and organization

The writing of the lssem-suite codes is initiated by a complete design and organization. The starting point for the design is the concept of the least-squares formulation and the spectral element discretization. The features of the design include the following:

- The problem operator definition part is made flexible and isolated from the numerical modules. The design of the lssem-suite data structure allows a dimension independent implementation of the problem dependent parts.
- The problem operator is defined locally in a subelement. Element-stiffness matrices are computed and stored locally.
- Special modules have been developed to handle the subelement indices setting, as well as assembly/scattering between the local and global problem operators.
- The Dirichlet-node boundary information is implemented with a weak boundary approach such that the Dirichlet-node coordinate setting is numbered by global numbering on the global stiffness matrix.
- Dynamic data structure. The storage management within lssem-suite is fully dynamic so that modifications of routines are not necessary when changing the prob-

lem and dimension size.

To ensure the maximum reuse of the codes, the solver of the nonlinear and multi-problem systems which may require extra modules, are built upon the linear single problem solver. Figure B.1 (a) shows the structure of the lssem-suite comprising four different LSSEM

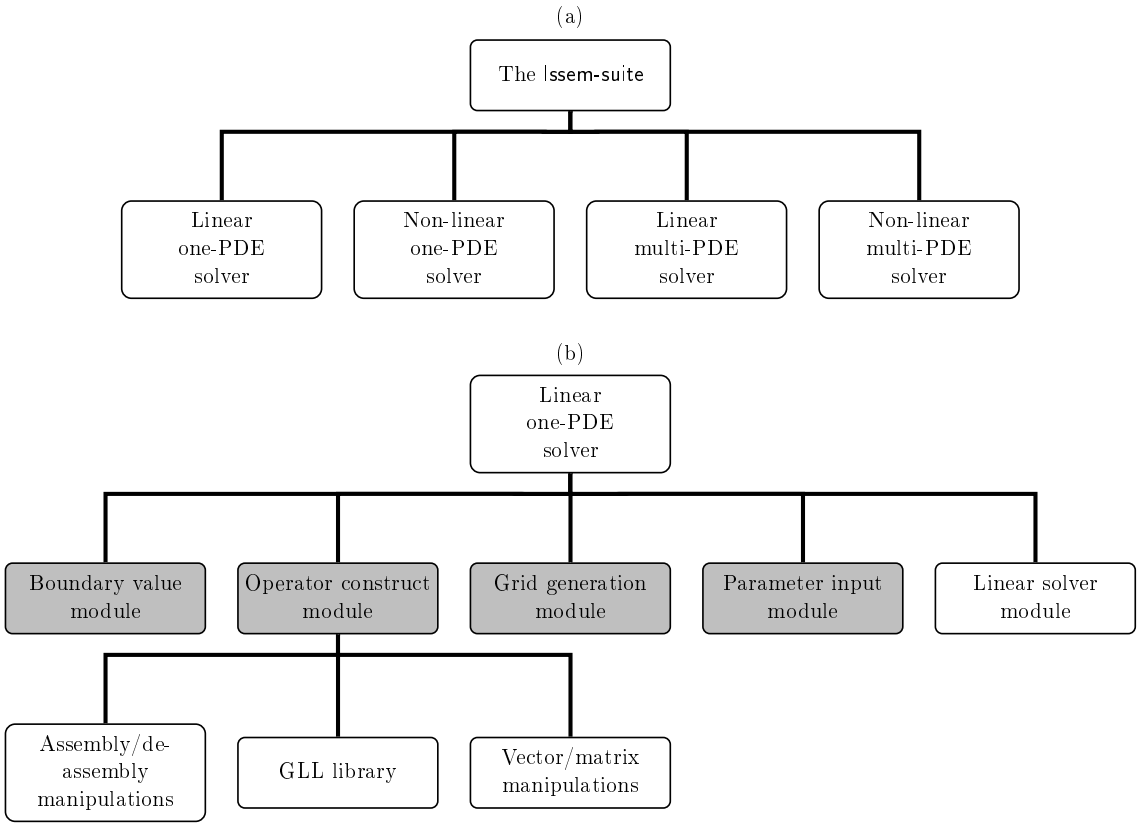

Figure B.1: The structure of the lssem-suite components.

solvers that are applied in four different circumstances. The fundamental one - the linear one-problem solver, with its structure being presented in Figure B.1 (b), provide solutions of the discrete linear problems on a fixed mesh. The structure of this solver has been made as an independent unit. It consists of five modules, in which the first four in gray boxes in Figure B.1(b) take the user-defined problem specification, boundary conditions, grid informations and parameters as input. These modules have direct interactions with the users.

At the bottom level is the assembly/scattering manipulation modules, providing the key operations constructing the global operators by looping over the local contributions defined in each subelement. The GLL module computes the values of the basis functions, the Gaussian quadrature weights and positions, and the derivative of the basis functions at the locations of the quadrature points with respect to each independent variable, etc. A vector/matrix manipulation module defining several elementary matrix operations is also included.

Based on the elementary linear one-PDE least-squares method solver, several variations which are suitable for different types of problems can be developed with the help of two additional modules, the Picard iterative module and the multiple PDE problem module. Figure B.2 shows the relationship of these modules from which new advanced solvers are evolved. The linear one-problem solver is wrapped into the codes of the existing solvers and serves as the inner core.

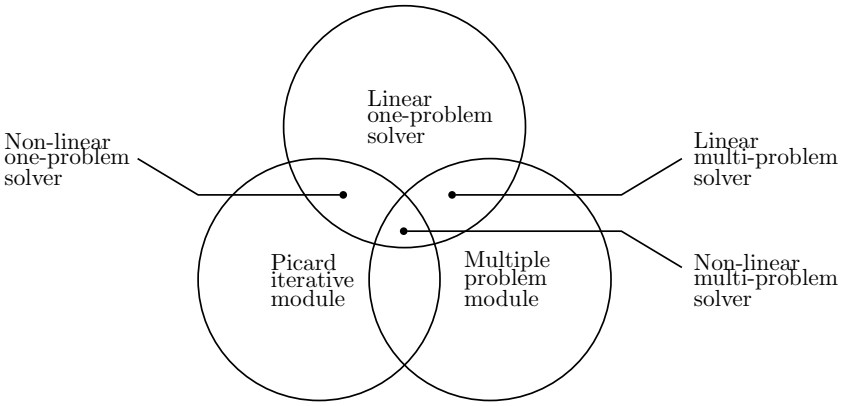

Figure B.2: The relationship of the solvers in lssem-suite.

Using these solvers, the toolbox lssem-suite provides the whole abstract framework of the least-squares spectral element method, easy and flexible problem posing and customizing, and meshes routines for grid generation, with the complete administration of the spectral element space and the corresponding degrees of freedom during the mesh modifications.

B.3 An example of usage of the lssem-suite

In this section, an example on how to solve a partial differential equation using the lssem-suite solvers is outlined. The test problem is a linear two-dimensional Poisson's equation with boundary conditions. This example shows the basic usage of the lssem-suite, which includes the following steps:

- Grid generation;
- Boundary condition specification;
- Problem operator and source term specification;
- Solving the linear system of equations.

B.3.1 Problem description

Consider a two-dimensional Poisson's equation:

$$\frac{\partial^2 \psi}{\partial x^2} + \frac{\partial^2 \psi}{\partial y^2} = 6xy(1-y) - 2x^3 \quad \text{in } \Omega = (0,\,1)^2 \in \mathbb{R}^2 \tag{B.1}$$

with its boundary conditions:

- in x-direction

$$\begin{cases} x = 0: & \psi(0, y) = 0 \\ x = 1: & \psi(1, y) = y(1-y) \end{cases} \tag{B.2}$$

- in y-direction

$$\psi(x, 0) = \psi(x, 1) = 0 \tag{B.3}$$

The problem has a analytical solution:

$$\psi(x, y) = y(1-y)x^3 \tag{B.4}$$

We solve the equation by introducing two new variables u and v

$$u = \frac{\partial \psi}{\partial x} \tag{B.5}$$

$$v = \frac{\partial \psi}{\partial y} \tag{B.6}$$

which represent the first derivatives of ψ with respect to x and y, respectively. Therefore the new set of equations can be written as

$$\frac{\partial u}{\partial x} + \frac{\partial v}{\partial y} = g(x, y) \tag{B.7}$$

$$\frac{\partial \psi}{\partial x} - u = 0 \tag{B.8}$$

$$\frac{\partial \psi}{\partial y} - v = 0 \tag{B.9}$$

or in matrix form

$$\mathscr{L}\mathbf{f} = \mathbf{L_x}\frac{\partial \mathbf{f}}{\partial x} + \mathbf{L_y}\frac{\partial \mathbf{f}}{\partial y} + \mathbf{L_0}\mathbf{f} = \mathbf{g} \tag{B.10}$$

in which, the unknown vector and source terms are defined as

$$\mathbf{f} = \begin{bmatrix} u \\ v \\ \psi \end{bmatrix}, \quad \mathbf{g} = \begin{bmatrix} 6xy(1-y) - 2x^3 \\ 0 \\ 0 \end{bmatrix} \tag{B.11}$$

and the parameter matrices are defined as

$$\mathbf{L_x} = \begin{bmatrix} 1 & 0 & 0 \\ 0 & 0 & 1 \\ 0 & 0 & 0 \end{bmatrix}, \quad \mathbf{L_y} = \begin{bmatrix} 0 & 1 & 0 \\ 0 & 0 & 0 \\ 0 & 0 & 1 \end{bmatrix} \quad \mathbf{L_0} = \begin{bmatrix} 0 & 0 & 0 \\ -1 & 0 & 0 \\ 0 & -1 & 0 \end{bmatrix}. \tag{B.12}$$

B.3.2 Specify grid information

A function file (poisson.m) aimed at resolving the Poisson's problem is created under the Matlab search path starting with the specification of the grid. It should have the form of Listing B.1.

```
1  % x-direction
2  xStartArray = [0.0,0.3,0.7];
3  xEndArray   = [0.3,0.7,1.0];
4  nxDofArray  = [3,4,3];
5  nxGllArray  = [3,4,3];
6  xPtsType    = 'GLL';
7  xDomainData = lssemdomain(xStartArray,xEndArray,nxDofArray, ...
8                nxGllArray,xPtsType);
9
10 % y-direction
11 yStartArray = [0.0,0.3,0.7];
12 yEndArray   = [0.3,0.7,1.0];
13 nyDofArray  = [4,5,4];
14 nyGllArray  = [4,5,4];
15 yPtsType    = 'GLL';
16 yDomainData = lssemdomain(yStartArray,yEndArray,nyDofArray, ...
17                 nyGllArray,yPtsType);
18
19 % domainDataVec is an array of structs.
20 domainDataVec = [xDomainData yDomainData];
21
22 [xt yt]   = deal(domainDataVec(:).DOFPtsArray);
23 [Nxt Nyt] = deal(domainDataVec(:).nDOF);
```

Listing B.1: Specification of problem domain and grid information

Here we divid both the x-direction and y-direction into three partitions so that the global domain comprises 3×3 subdomains.

Lines 2-3 in Listing (B.1) define the lower and upper boundaries of each subelement for dimension x. Then, lines 4-5 assign the number of degree of freedom and the order of the quadrature the integration by enumerating numbers in vectors. As mentioned in section B.1, the order of integration must always be equal or greater than number of the DOFs. The user is not precluded from choosing a subelement that has different integration order than degrees of freedom per element.

The options for the type of polynomials are either Gauss-Legendre-Lobatto (GLL) or Gauss-Legendre (GL). Lines 11-15 repeat the same procedure for the y-direction. The function `lssemdomain` takes the above information as arguments, and computes the grid-related variables and encapsulates them into the struct variables `xDomainData` and

yDomainData for each dimension. The xDomainData and yDomainData structs are later wrapped into an array of structs named domainDataVec, by which the information of the global discrete points and total number of these points can be retrieved from line 22 and line 23.

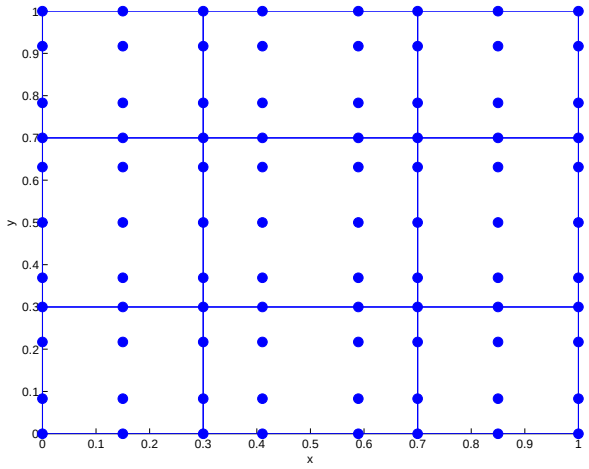

Figure B.3: A 2D Poisson's problem's domain that consists of 9 subdomains ($e_x = 3$, $e_y = 3$ and $e = e_x e_y = 9$).

The results of the grid structure is shown in Figure B.3, where the initial grid which is the square of $[-1, 1] \times [-1, 1]$ consists of only one cell, has been refined. The final grid has $3 \times 3 = 9$ cells, and a total of $8 \times 8 = 64$ degrees of freedom.

B.3.3 The boundary condition specification

The Dirichlet boundary condition of the Poisson problem requires specifications in the discrete domain. The solver needs to know at which points, what value has been assigned to which variables.

A matrix called *boundary matrix* can be constructed to hold these information. In this two-dimensional example, we define the *boundary matrix* psiBc (see Figure B.4). with its first two column corresponding to the *global subscripts* indicating the boundary nodes position in each dimension. The third column is the variable index (3 corresponds to ψ) and the last column stores a float condition for the boundary condition of the variable at the specified boundary points.

The number of rows of the psiBc equals to the number of DOFs on the whole or on parts of the boundary. In this test case, according to the given boundary conditions (B.2) and (B.3), all the exterior points of the domain have been specified and the number of rows of psiBc is 2×(Nxt+Nyt). The code for specifying the boundary condition is shown in Listing B.2.

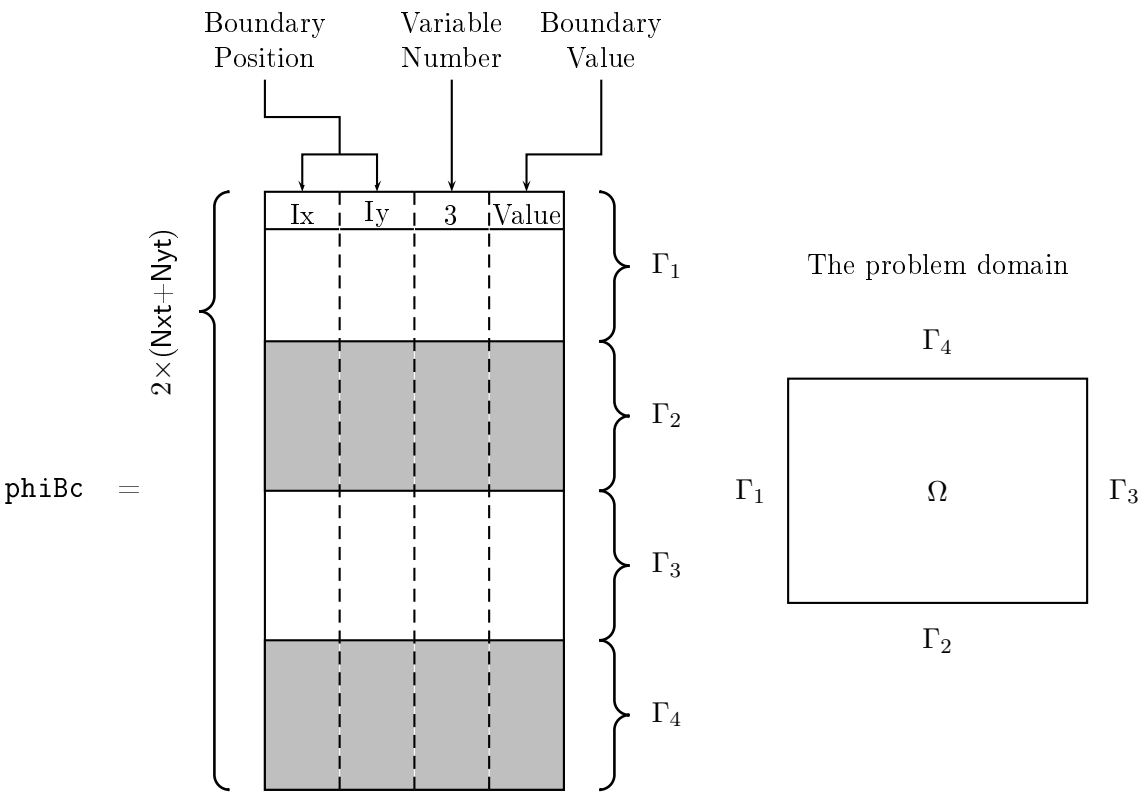

Figure B.4: The boundary value matrix, `psiBc`.

```
% Number of the dimensions
nDims = length(domainDataVec);

% Boundary matrix
psiBc = zeros(2*Nxt+2*Nyt,nDims+2);

% Boundary condition counter
iBc = 0;

% Gamma 1
Ix  = 1;
for Iy = 1:Nyt
    iBc = iBc+1;
    psiBc(iBc,:) = [Ix,Iy,3,0];
end

% Gamma 3
Ix  = length(xt);
for Iy = 1:Nyt
    iBc = iBc+1;
    psiBc(iBc,:) = [Ix,Iy,3,yt(Iy)*(1-yt(Iy))];
end

% Gamma 2
Iy  = 1;
for Ix = 1:Nxt
    iBc = iBc+1;
    psiBc(iBc,:) = [Ix,Iy,3,0];
end

% Gamma 4
Iy  = length(yt);
for Ix = 1:Nxt
    iBc = iBc+1;
    psiBc(iBc,:) = [Ix,Iy,3,0];
end

fBc = psiBc;
```

Listing B.2: Specification boundary conditions

B.3.4 The problem operator specification

In Listing B.3 the problem operator and the source term have been defined. The function `opt` provides the problem operator `lv` and source vector `gv` for each node of the subelement for the 2D Poisson problem.

The function name `opt` can be defined freely by the user, whereas the function pattern is built and fixed. It takes arguments of `subdomainDataVec` which encapsulates all grid information regarding to the present subelement, and `iVec`, `jVec` store the *local subscripts* comprising the integration order and the DOFs, respectively.

In general, we need the values of the basis functions at the quadrature points, their gradients and sometimes the weights in each subelement. Lines 3-5 in Listing B.3 are the assignments of these values extracted from the `subdomainDataVec`. The capital `B` is used to indicate the 1D local discrete mass matrix and capital `D` for the 1D local derivative matrix. The next 2 lines of codes acquire the *local subscripts* of the quadrature integration order (`ix` and `iy`) from `iVec` and the *local subscripts* of the Lagrangian polynomials (`jx` and `jy`) from `jVec`.

The matrices `lx`, `ly` and `l0` are the differential operator with respect to x, differential operator with respect to y and the zeroth order operator. They have exactly the same structures as have been defined in Eq.(B.12). We can get the partial derivatives of the 2D shape function with respect to x/y at the quadrature points by using the product of the 1D Lagrangian polynomials values and the values of the derivatives of the 1D Lagrangian polynomials with respect to x/y at these particular quadrature points. That is

$$\frac{\partial}{\partial x}\left(\phi_{j_x}(x)\phi_{j_y}(y)\right)\Big|_{x=x_{i_x},y=y_{i_y}} = \phi'_{j_x}(x_{i_x})\phi_{j_y}(y_{i_y}) = [\mathbf{d}_x]_{i_x,j_x}[\mathbf{b}_y]_{i_y,j_y} \tag{B.13}$$

$$\frac{\partial}{\partial y}\left(\phi_{j_x}(x)\phi_{j_y}(y)\right)\Big|_{x=x_{i_x},y=y_{i_y}} = \phi_{j_x}(x_{i_x})\phi'_{j_y}(y_{i_y}) = [\mathbf{b}_x]_{i_x,j_x}[\mathbf{d}_y]_{i_y,j_y} \tag{B.14}$$

in which, the 1D mass matrix $\mathbf{b}_x$, $\mathbf{b}_y$ and the 1D derivative matrix $\mathbf{d}_x$, $\mathbf{d}_y$ correspond to the array variables `Bx`, `By` and `Dx`, `Dy`.

Based on Eq.(B.10) the overall problem operator `lv` is obtained (line 20-22 in Listing B.3). We then do the same thing for the right hand side source term. The function `source` is an user-defined routine providing the source vector `gv`.

Note that the values of the local operator and source vector are evaluated each time the `subdomainDataVec`, index vectors `iVec` and `jVec` vary, whereas the `subdomainDataVec` that contains the quadrature information, derivative matrix, etc, regardless whether they are needed or not, are only recomputed and updated when switching to a new subelement.

```
1 function [lv gv]=opt(subdomainDataVec,iVec,jVec,pars)
2
3     [xh yh] = deal(subdomainDataVec(:).gllPts);
4     [Bx By] = deal(subdomainDataVec(:).B);
5     [Dx Dy] = deal(subdomainDataVec(:).D);
```

```
6
7       % local indices
8       [ix iy] = dealvector(iVec);
9       [jx jy] = dealvector(jVec);
10
11      % Differential operator with respect to x
12      lx = [1 0 0;0 0 1;0 0 0];
13
14      % Differential operator with respect to y
15      ly = [0 1 0;0 0 0;0 0 1];
16
17      % Zeroth order operator
18      l0 = [0 0 0;-1 0 0;0 -1 0];
19
20      lv = lx*Dx(ix,jx)*By(iy,jy)+...
21           ly*Bx(ix,jx)*Dy(iy,jy)+...
22           l0*Bx(ix,jx)*By(iy,jy);
23
24      gv = source(xh(ix),yh(iy));
25  end
26
27  function gv=source(x,y)
28      gv = zeros(3,1);
29      gv(1) = 6*x*y*(1-y)-2*x^3;
30      gv(2) = 0;
31      gv(3) = 0;
32  end
```

Listing B.3: Specification of the problem operator and source vector

All the matrices of `lv` and the vector `gv` computed on the subelement will be sent to the assembly module to build up a global operator and a global source vector, and to formulate a large-scale linear problem, from which all the unknowns will be computed. We could write the results directly into the global matrix, but this is not very efficient since access to the elements of a large matrix is slow. Rather, we first compute the contribution of each subelement in a small matrix with the degrees of freedom on the present subelement, and transfer them to the global matrix only when the computations are finished for this subelement. We do the same for the right hand side vector.

B.3.5 Call the lssem-suite solver

Now everything is set up for the solution of the discrete system. Since this two-dimensional Poisson problem is linear and no other problems defined in different function spaces are specified, we chose the linear one-problem LSSEM routine, `linearlssemoneproblem`

to solve the problem. As presented in Listing B.4, the routine *linearlssemoneproblem* takes the arguments of the grid information struct `domainDataVec`, the user-defined operator function `opt`, the boundary value matrix `fBc`, the options and parameters. The empty brackets assigned to the `options` and the `pars` indicate that we simply take the default setting for the solver and no parameter needs to be passed.

The outputs of the solver is the solution `f`, the global least-squares operator `A`, the global source vector `F` and the condition number of the global operator `condA`.

The last index of the multiple dimension the array `f` indicates the variable index. The order of the variables in array `f` corresponds to the operators (`lx`, `ly` and `l0`) defined in the Listing B.3. All the three unknowns u, v and ψ can be extracted from `f` by some post-processing as given in lines 8-10 in Listing B.4.

```
1 options = [];
2 pars    = [];
3
4 [f,A,F,condA] = linearlssemoneproblem(domainDataVec, ...
5 @opt,fBc,options,pars);
6
7 u   = f(:,:,1);
8 v   = f(:,:,2);
9 phi = f(:,:,3);
```

Listing B.4: Solve the Poisson problem by `linearlssemoneproblem` solver

Figure B.5 shows the numerical solution of potential variable ψ with comparison with the analytical solution.

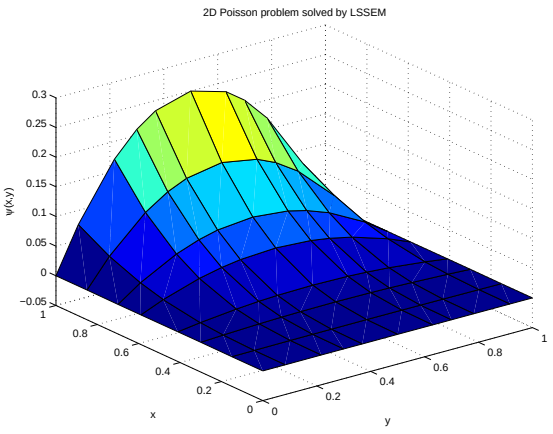

Figure B.5: The numerical result of a 2D Poisson's problem with $\|\psi - \psi^{\text{exact}}\|_{L_2(\Omega)} = 1.0326 \times 10^{-7}$ with the convergence criteria set as $|\psi^{new} - \psi^{old}| \leq 1 \times 10^{-6}$.

B.3.6 The plain script

The following is the full script of the Matlab code for solving the two-dimensional Poisson's problem, poisson.m.

```
%%%%%%%%%%%%%%%
%% Grid information
%%%%%%%%%%%%%%%

% x-direction
xStartArray = [0.0,0.3,0.7];
xEndArray   = [0.3,0.7,1.0];
nxDofArray  = [3,4,3];
nxGllArray  = [3,4,3];
xPtsType    = 'GLL';
xDomainData = lssemdomain(xStartArray,xEndArray,nxDofArray, ...
              nxGllArray,xPtsType);

% y-direction
yStartArray = [0.0,0.3,0.7];
yEndArray   = [0.3,0.7,1.0];
nyDofArray  = [4,5,4];
nyGllArray  = [4,5,4];
yPtsType    = 'GLL';
yDomainData = lssemdomain(yStartArray,yEndArray,nyDofArray, ...
               nyGllArray,yPtsType);

% domainDataVec is an array of structs.
domainDataVec = [xDomainData yDomainData];

[xt yt]   = deal(domainDataVec(:).DOFPtsArray);
[Nxt Nyt] = deal(domainDataVec(:).nDOF);


%%%%%%%%%%%%%%%
%% Boundary conditions
%%%%%%%%%%%%%%%

% Number of the dimensions
nDims = length(domainDataVec);

% Boundary matrix
psiBc = zeros(2*Nxt+2*Nyt,nDims+2);

```

```
% Boundary condition counter
iBc = 0;

% Gamma 1
Ix  = 1;
for Iy = 1:Nyt
    iBc = iBc+1;
    psiBc(iBc,:) = [Ix,Iy,3,0];
end

% Gamma 3
Ix  = length(xt);
for Iy = 1:Nyt
    iBc = iBc+1;
    psiBc(iBc,:) = [Ix,Iy,3,yt(Iy)*(1-yt(Iy))];
end

% Gamma 2
Iy  = 1;
for Ix = 1:Nxt
    iBc = iBc+1;
    psiBc(iBc,:) = [Ix,Iy,3,0];
end

% Gamma 4
Iy  = length(yt);
for Ix = 1:Nxt
    iBc = iBc+1;
    psiBc(iBc,:) = [Ix,Iy,3,0];
end

fBc = psiBc;

%%%%%%%%%%%%%%
%% Problem operator, source vector
%%%%%%%%%%%%%%

function [lv gv]=opt(subdomainDataVec,iVec,jVec,pars)

    [xh yh] = deal(subdomainDataVec(:).gllPts);
    [Bx By] = deal(subdomainDataVec(:).B);
    [Dx Dy] = deal(subdomainDataVec(:).D);

    % local indices
```

```
84      [ix iy] = dealvector(iVec);
85      [jx jy] = dealvector(jVec);
86
87      % Differential operator with respect to x
88      lx = [1 0 0;0 0 1;0 0 0];
89
90      % Differential operator with respect to y
91      ly = [0 1 0;0 0 0;0 0 1];
92
93      % Zeroth order operator
94      l0 = [0 0 0;-1 0 0;0 -1 0];
95
96      lv = lx*Dx(ix,jx)*By(iy,jy)+...
97           ly*Bx(ix,jx)*Dy(iy,jy)+...
98           l0*Bx(ix,jx)*By(iy,jy);
99
100     gv = source(xh(ix),yh(iy));
101 end
102
103 function gv=source(x,y)
104     gv = zeros(3,1);
105     gv(1) = 6*x*y*(1-y)-2*x^3;
106     gv(2) = 0;
107     gv(3) = 0;
108 end
109
110 %%%%%%%%%%%%%%
111 %% Least-squares solution
112 %%%%%%%%%%%%%%
113
114 options = [];
115 pars    = [];
116
117 [f,A,F,condA] = linearlssemoneproblem(domainDataVec, ...
118 @opt,fBc,options,pars);
119
120 u   = f(:,:,1);
121 v   = f(:,:,2);
122 phi = f(:,:,3);
```

Listing B.5: poisson.m

Appendix C

Formulation of the Length-Based PBE

The derivation of the length-based PBE from the volume-based PBE is based on work of Marchisio et al.[67].

The volume-based PBE is

$$\frac{\partial \tilde{f}(V,\mathbf{r},t)}{\partial t} + \nabla_{\mathbf{r}} \cdot (\mathbf{v}_d \tilde{f}(V,\mathbf{r},t)) = \tilde{\mathcal{B}}^{+}(V,\mathbf{r},t) - \tilde{\mathcal{B}}^{-}(V,\mathbf{r},t) + \tilde{\mathcal{A}}^{+}(V,\mathbf{r},t) - \tilde{\mathcal{A}}^{-}(V,\mathbf{r},t) \tag{C.1}$$

in which,

$$\tilde{\mathcal{B}}^{+}(V,\mathbf{r},t) = \int_{V}^{V_{max}} \nu \tilde{P}(V,V')\tilde{b}(V')\tilde{f}(V',\mathbf{r},t)dV' \tag{C.2}$$

$$\tilde{\mathcal{B}}^{-}(V,\mathbf{r},t) = \tilde{b}(V)\tilde{f}(V,\mathbf{r},t) \tag{C.3}$$

$$\tilde{\mathcal{A}}^{+}(V,\mathbf{r},t) = \frac{1}{2}\int_{V_{min}}^{V} \tilde{a}(V-V',V')\tilde{f}(V',\mathbf{r},t)\tilde{f}(V-V',\mathbf{r},t)dV' \tag{C.4}$$

$$\tilde{\mathcal{A}}^{-}(V,\mathbf{r},t) = \tilde{f}(V,\mathbf{r},t)\int_{V_{min}}^{V_{max}-V} \tilde{a}(V,V')\tilde{f}(V',\mathbf{r},t)dV' \tag{C.5}$$

We can define the following relations between the volume-based quantities (denoted by symbols with a tilde "~") and the length-based quantities (denoted by symbols without a tilde "~").

$$\tilde{f}(V,\mathbf{r},t) = \frac{1}{3\xi^2} f(\xi,\mathbf{r},t) \tag{C.6}$$

$$\tilde{b}(V) = \tilde{b}(\xi^3) = b(\xi) \tag{C.7}$$

$$\tilde{P}(V,V') = \tilde{P}(\xi^3,\zeta^3) = \frac{1}{3\xi^2} P(\xi,\zeta) \tag{C.8}$$

$$\tilde{a}(V,V') = \tilde{a}(\xi^3,\zeta^3) = a(\xi,\zeta) \tag{C.9}$$

Thus, we multiply $3\xi^2$ on both sides of the Eq.(C.1). By applying the relations (C.6)-(C.9), the birth and death terms of the length-based PBE can be derived.

$$\begin{aligned}\mathcal{B}^+(\xi,\mathbf{r},t) &= 3\xi^2\tilde{\mathcal{B}}^+(V,\mathbf{r},t)\\ &= 3\xi^2\left[\int_V^{V_{max}}\nu\tilde{P}(V,V')\tilde{b}(V')\tilde{f}(V',\mathbf{r},t)dV'\right]\\ &= 3\xi^2\left[\int_\xi^{\xi_{max}}\nu\left(\frac{1}{3\xi^2}\right)P(\xi,\zeta)b(\zeta)\left(\frac{1}{3\zeta^2}\right)f(\zeta,\mathbf{r},t)(3\zeta^2)\,d\zeta\right]\\ &= \int_\xi^{\xi_{max}}\nu P(\xi,\zeta)b(\zeta)f(\zeta,\mathbf{r},t)d\zeta\end{aligned} \tag{C.10}$$

$$\begin{aligned}\mathcal{B}^-(\xi,\mathbf{r},t) = 3\xi^2\tilde{\mathcal{B}}^-(V,\mathbf{r},t) &= 3\xi^2\left[\tilde{b}(V)\tilde{f}(V,\mathbf{r},t)\right]\\ &= 3\xi^2\left[b(\xi)\left(\frac{1}{3\zeta^2}\right)f(\xi,\mathbf{r},t)\right] = b(\xi)f(\xi,\mathbf{r},t)\end{aligned} \tag{C.11}$$

$$\begin{aligned}\mathcal{A}^+(\xi,\mathbf{r},t) &= 3\xi^2\tilde{\mathcal{A}}^+(V,\mathbf{r},t)\\ &= 3\xi^2\left[\frac{1}{2}\int_{V_{min}}^{V}\tilde{a}(V-V',V')\tilde{f}(V',\mathbf{r},t)\tilde{f}(V-V',\mathbf{r},t)dV'\right]\\ &= 3\xi^2\left[\frac{1}{2}\int_{\xi_{min}}^{\xi}a((\xi^3-\zeta^3)^{1/3},\zeta)\frac{f(\zeta,\mathbf{r},t)}{3\zeta^2}\frac{f((\xi^3-\zeta^3)^{1/3},\mathbf{r},t)}{3(\xi^3-\zeta^3)^{2/3}}(3\zeta^2)\,d\zeta\right]\\ &= \frac{\xi^2}{2}\int_{\xi_{min}}^{\xi}\frac{a((\xi^3-\zeta^3)^{1/3},\zeta)}{(\xi^3-\zeta^3)^{2/3}}f(\zeta,\mathbf{r},t)f((\xi^3-\zeta^3)^{1/3},\mathbf{r},t)d\zeta\end{aligned} \tag{C.12}$$

$$\begin{aligned}\mathcal{A}^-(\xi,\mathbf{r},t) &= 3\xi^2\left[\tilde{f}(V,\mathbf{r},t)\int_{V_{min}}^{V_{max}-V}\tilde{a}(V,V')\tilde{f}(V',\mathbf{r},t)dV'\right]\\ &= 3\xi^2\left[\frac{f(\xi,\mathbf{r},t)}{(3\xi^2)}\int_{\xi_{min}}^{(\xi_{max}^3-\xi^3)^{1/3}}a(\xi,\zeta)\frac{f(\zeta,\mathbf{r},t)}{3\zeta^2}(3\zeta^2)\,d\zeta\right]\\ &= f(\xi,\mathbf{r},t)\int_{\xi_{min}}^{(\xi_{max}^3-\xi^3)^{1/3}}a(\xi,\zeta)f(\zeta,\mathbf{r},t)d\zeta\end{aligned} \tag{C.13}$$

Summarizing (C.10)-(C.13), yields the length-based PBE:

$$\frac{\partial f(\xi,\mathbf{r},t)}{\partial t}+\nabla_{\mathbf{r}}\cdot(\mathbf{v}_d f(\xi,\mathbf{r},t)) = \mathcal{B}^+(\xi,\mathbf{r},t)-\mathcal{B}^-(\xi,\mathbf{r},t)+\mathcal{A}^+(\xi,\mathbf{r},t)-\mathcal{A}^-(\xi,\mathbf{r},t) \tag{C.14}$$

in which,

$$\mathcal{B}^{+}(\xi,\mathbf{r},t) = \int_{\xi}^{\xi_{max}} \nu P(\xi,\zeta) b(\zeta) f(\zeta,\mathbf{r},t) d\zeta \tag{C.15}$$

$$\mathcal{B}^{-}(\xi,\mathbf{r},t) = b(\xi) f(\xi,\mathbf{r},t) \tag{C.16}$$

$$\mathcal{A}^{+}(\xi,\mathbf{r},t) = \frac{\xi^2}{2} \int_{\xi_{min}}^{\xi} \frac{a((\xi^3-\zeta^3)^{1/3},\zeta)}{(\xi^3-\zeta^3)^{2/3}} f(\zeta,\mathbf{r},t) f((\xi^3-\zeta^3)^{1/3},\mathbf{r},t) d\zeta \tag{C.17}$$

$$\mathcal{A}^{-}(\xi,\mathbf{r},t) = f(\xi,\mathbf{r},t) \int_{\xi_{min}}^{(\xi_{max}^3-\xi^3)^{1/3}} a(\xi,\zeta) f(\zeta,\mathbf{r},t) d\zeta \tag{C.18}$$

where ξ and ζ represent the particle diameter.

Appendix D

Proof of the Saddle Point Problem

Consider the following linear algebraic matrix system is obtained for the mass conservative PBE problem (see section 4.3.5).

$$\begin{bmatrix} \mathbf{A}_e & \mathbf{B}^T \\ \mathbf{B} & \mathbf{0} \end{bmatrix} \begin{bmatrix} \mathbf{f}_e \\ \boldsymbol{\lambda} \end{bmatrix} = \begin{bmatrix} \mathbf{F}_e \\ \mathbf{G} \end{bmatrix} \tag{D.1}$$

or

$$\mathbf{A}_c \mathbf{f}_c = \mathbf{F}_c \tag{D.2}$$

where,

$$\mathbf{A}_c = \begin{bmatrix} \mathbf{A}_e & \mathbf{B}^T \\ \mathbf{B} & \mathbf{0} \end{bmatrix}, \quad \mathbf{f}_c = \begin{bmatrix} \mathbf{f}_e \\ \boldsymbol{\lambda} \end{bmatrix} \quad \text{and } \mathbf{F}_c = \begin{bmatrix} \mathbf{F}_e \\ \mathbf{G} \end{bmatrix}$$

in which $\mathbf{A}_e$, $\mathbf{F}_e$ are defined in (4.45) and (4.46), respectively. The matrix $\mathbf{B} \in \mathbb{R}^{(M^t \times N^t)}$,

$$[\mathbf{B}]_{ij} = B(\Phi_j, \Psi_i) = \langle \Psi_i, \left[\left(\int_{\Omega_r} \Phi_j \text{vol}(\xi)\, d\xi \right) \mathbf{v}_d \right] \rangle_{Y(\Omega_e)} \tag{D.3}$$

for $1 \leq i \leq N^t$ and $1 \leq j \leq M^t$.

The vectors $\boldsymbol{\lambda}$, $\mathbf{G} \in \mathbb{R}^{(M^t \times 1)}$, the matrix $\mathbf{A}_c \in \mathbb{R}^{(N^t+M^t)\times(N^t+M^t)}$, and the vectors $\mathbf{f}_c$, $\mathbf{F}_c \in \mathbb{R}^{(N^t+M^t)\times 1}$.

The constrained LSSEM then has M^t more unknowns than the standard LSSEM for the same discretization. The extended matrix $\mathbf{A}_c$ resulting from the modified system is symmetric and pseudopositive definite, which we explain in the following.

Since $\mathbf{A}_e$ is a standard LSM operator, we have

$$\mathbf{A}_c = \mathbf{A}_c^T \tag{D.4}$$

therefore $\mathbf{A}_c$ is symmetric and $\mathbf{A}_c$ has real eigenvalues.

Then consider an arbitrary nontrivial vector

$$\mathbf{f}_c = \begin{bmatrix} \mathbf{p} \\ \mathbf{0} \end{bmatrix} \neq 0$$

yields,

$$\mathbf{f}_c^T \mathbf{A}_c \mathbf{f}_c = \mathbf{p}^T \mathbf{A}_e \mathbf{p} > 0 \tag{D.5}$$

Next consider

$$\mathbf{f}_c = \begin{bmatrix} \mathbf{A}_e^{-1} \mathbf{B}^T \mathbf{q} \\ -\mathbf{q} \end{bmatrix} \neq 0$$

and

$$\mathbf{f}_c^T \mathbf{A}_c \mathbf{f}_c = -\mathbf{q}^T \mathbf{B} \mathbf{A}_e^{-1} \mathbf{B}^T \mathbf{q} = -\mathbf{p}^T \mathbf{A}_e^{-1} \mathbf{p} < 0 \tag{D.6}$$

In conclusion, $\mathbf{A}_c$ is semi-positive definite and therefore must have both positive and negative eigenvalue. The algebraic problem does not correspond to either a minimization problem or a maximization problem, but a saddle point problem.

The discrete form of the *Lagrangian*, $\mathcal{I}(\mathbf{w}, \boldsymbol{\eta})$ is defined by

$$\begin{gathered} \mathcal{I} : \mathbb{R}^{N^t} \times \mathbb{R}^{M^t} \to \mathbb{R} \\ \mathcal{I}(\mathbf{w}, \boldsymbol{\eta}) = \mathcal{J}(\mathbf{w}) + \boldsymbol{\lambda}^T (\mathbf{B}\mathbf{w} - \mathbf{G}) \end{gathered} \tag{D.7}$$

The non-constraint quadratic functional for the $\mathcal{J}(\mathbf{w})$,

$$\mathcal{J}(\mathbf{w}) = \frac{1}{2} \mathbf{w}^T \mathbf{A}_e \mathbf{w} - \mathbf{w}^T \mathbf{F}_e \tag{D.8}$$

which can be written as a constrained functional

$$\mathcal{I}(\mathbf{w}, \boldsymbol{\eta}) = \frac{1}{2} \mathbf{w}^T \mathbf{A}_e \mathbf{w} - \mathbf{w}^T \mathbf{F}_e + \boldsymbol{\lambda}^T (\mathbf{B}\mathbf{w} - \mathbf{G}) \tag{D.9}$$

The stationary point, $(\mathbf{w}, \boldsymbol{\eta})$, of the Lagrangian, $\mathcal{I}(\mathbf{w}, \boldsymbol{\eta})$, corresponds to a saddle point of $\mathcal{I}$, hence

$$\mathcal{I}(\mathbf{f}, \boldsymbol{\lambda}) = \min_{\mathbf{w} \in \mathbb{R}^{N^t}} \max_{\boldsymbol{\lambda} \in \mathbb{R}^{M^t}} \mathcal{I}(\mathbf{w}, \boldsymbol{\lambda}) = \max_{\boldsymbol{\lambda} \in \mathbb{R}^{M^t}} \min_{\mathbf{w} \in \mathbb{R}^{N^t}} \mathcal{I}(\mathbf{w}, \boldsymbol{\lambda}) \tag{D.10}$$

In this saddle point problem, the Ladyzhenskaja-Babuška-Brezzi (LBB) condition commonly referred to as the (discrete) *inf-sup* condition owing to the equivalent form yields

$$\inf_{\lambda_N \in M_N, \lambda_N \neq 0} \sup_{f_N \in X_N, f_N \neq 0} \frac{B(f_N, \lambda_N)}{\|f_N\|_X \|\lambda_N\|_M} \geq K_b \tag{D.11}$$

in which K_b is a positive constant, must be satisfied.

Appendix E

Selected Papers

E.1 Paper I

Paper I: Zhengjie Zhu, C.A.Dorao and H.A.Jakobsen. A least–squares method with direct minimization for the solution of the breakage-coalescence population balance equation. *Mathematics and Computers in Simulation, Volume 79, Issue 3, 1 December 2008, Pages 716-727*.

A least–squares method with a direct minimization algorithm is introduced to solve the nonlinear population balance equation that consists of both breakage and coalescence terms. The least–squares solver, the direct minimization solver together with a finite difference solver are implemented for comparisons. It is shown that the coalescence term introduces a strong non–linear behavior which can affect the robustness of the numerical solvers. In the comparison with the least–squares method, the direct minimization method is proved to be capable of producing equally accurate results, while its formulation is better conditioned. In the case of a nonlinear population balance equation system, the direct minimization method converges faster than the standard least–squares method.

Is not included due to copyright

E.2 Paper II

Paper II: Zhengjie Zhu, C.A.Dorao and H.A.Jakobsen. Solution of bubble number density with breakage and coalescence in a bubble column by least-squares method. *Progress in Computational Fluid Dynamics (PCFD), Volume 9, Nos 6/7, Pages 436-446* .

A steady-state model has been built for an air-water bubble column. The bubble number density constitutive equation has been formulated through integrating the bubble transport equation. Proper kernels for the bubble breakage and coalescence rates have been taken from the literature. The momentum balance of the gas phase is included in the model which leads to a set of non-linear differential equations. The model has been successfully solved by using the least-squares method with high accuracy and fast convergence. The successive iteration has been applied to the linearized equation set. The model shows excellent agreements with experimental data.

Is not included due to copyright

E.3 Paper III

Paper III: Zhengjie Zhu, C.A.Dorao and H.A.Jakobsen. On the fully coupled solution of a two-fluid model combined population balance equation using the least-squares spectral element method. *Industrial & Engineering Chemistry Research, Volume 48(17), July 2, 2009, Pages 7994-8006*.

In this work, a cross-sectional averaged two-fluid model combined with a population balance model is applied to simulate the flow field and the bubble size distributions in a two-phase bubble column. The Martinez-Bazan breakage kernel and a modified Prince and Blanch coalescence kernel have been chosen to describe bubble breakage and bubble coalescence, respectively.

In the present study, we discuss the use of a higher order spectral element method - the least-squares method, to compute the system of equations in a coupled manner. The least-squares method is highly accurate and has a number of advantages over the conventional numerical methods like the finite difference- and finite volume methods. In contrast to the finite volume method, when designing an overall solution algorithm this least squares method ensures that all the continuity equations are satisfied individually and it deals with both the convective and diffusive terms stably and accurately. The novel iterative algorithm solves the flow and the population balance equation in a coupled manner.

The model has been validated against experimental data obtained for two-phase flow in a bubble column. The predicted bubble size distribution and other flow quantities are in good agreement with the experimental data.

Is not included due to copyright

E.4 Paper IV

Paper IV: Zhengjie Zhu, C.A.Dorao and H.A.Jakobsen. Mass conservative formulation of population balance equation using the least-squares spectral element method, Submitted to *Industrial & Engineering Chemistry Research* (Accepted).

In the standard least-squares formulation of the population balance equation significant loss of mass is observed for the dispersed phase. This mass loss is actually caused by the inexact conservation property reflected by many breakage kernels, hence incorrect physical interpretations of the model simulations may be drawn.

In this work a constrained least-squares spectral element method is developed enforcing mass conservation. This numerical property is accomplished by adding an extra restriction to the method in terms of the dispersed phase continuity equation through the Lagrange multipliers strategy. The discretized system resulting from applying the method to a two-phase population balance equation problem is symmetric and pseudopositive definite. Numerical experiments are carried out simulating the motion of a two-phase mixture passing through a 2D domain. The results obtained by the modified least-squares spectral element method show that the mass is conserved everywhere in the domain with high accuracy.

Is not included due to copyright

Appendix F

Secondary Papers

F.1 Paper V

Paper V: Zhengjie Zhu, C.A.Dorao and H.A.Jakobsen. Modelling a bubble column with a bubble number density equation using the least-squares method. *6th International Conference on CFD in Oil and Gas, Metallurgical and Process Industries, SINTEF/NTNU, Trondheim, Norway, 10-12 June 2008* **(Selected as lead paper by reviewers)**.

A steady-state model has been built for an air-water bubble column. The bubble number density constitutive equation has been formulated through integrating the bubble transport equation. Proper kernels for bubble breakage and coalescence rate have been taken from the literature. The momentum balance of the gas phase is included in the model which leads to a set of non-linear differential equations. The model has been successfully solved by using the least-squares method with high accuracy and fast convergence. The successive iteration has been applied to the linearized equation set. The model shows excellent agreements with experimental data.

F.2 Paper VI

Paper VI: Zhengjie Zhu, L.E.Patruno, C.A.Dorao and H.A.Jakobsen. Simulation of the bubble coalescence in bubble column using the least-squares method. *11th International Conference on Multiphase Flow in Industrial Plant, Palermo, Italy, 7-10 September 2008 (MFIP'08).*

The population balance equation (PBE) has been combined with a steady-state gas phase momentum equation to model the operation of an air-water bubble column. Instead of solving a bubble number density constitutive equation, a population balance equation

with coalescence term has been solved. The system of equations has been linearized by successive iteration and solved by the least-squares method with high accuracy and fast convergence. The bubble size distribution along the column axis has been investigated and compared to the corresponding experimental data, showing good agreement.